Physik

Viorel Dumitru

Physics and Technology of Nitride Lasers

Physics and Technology of Nitride Lasers

Vor der Fakultät Mathematik und Physik der Universität Stuttgart
zur Erlangung der Würde eines Doktors der Naturwissenschaften
(Dr. rer. nat.) genehmigte Abhandlung

vorgelegt von

Viorel Dumitru

aus Ploiesti

Hauptberichter:	Prof. Dr. H. Schweizer
Mitberichter:	Prof. Dr. M. Berroth
Tag der Einreichung	21 Juni 2004
Tag der mündlichen Prüfung	23 July 2004

Physikalisches Institut der Universität Stuttgart
2004

Contents

Publications and conferences:

H. Schweizer, H. Gräbeldinger, **V. Dumitru**, M.Jetter, S. Bader, G. Brüderl, A. Weimar, A. Lell, and V. Härle, *"Laterally coupled InGaN/GaN DFB laser diodes"*, phys. stat. sol 192 (a), 301-307, (2002)

F. Scholz, G. Moutchnik, **V. Dumitru**, R. Härle, H. Schweizer *"Investigations about series resistance of MOVPE grown GaN laser structures"* Journal of Crystal Growth 248, p. 507-512 (2003)

V. Dumitru, H. Schweizer, H. Gräbeldinger, R. Härle, S. Bader, G. Brüderl, A. Weimar, A. Lell, and V. Härle, *"InGaN/GaN multi-quantum well distributed Bragg reflector laser diode with second-order gratings"* Electron. Lett.39 (4) p.372, (2003)

F. Scholz, J. Off, Y. Kobayashi, V. Peres-Solorzano B., **V.Dumitru**, H. Schweizer *"Studies of MOVPE groth of GaInN for optoelectronic applications"*4th Japanese-Spanish-German Workshop on Recent Progress in Advanced Materials, Devices, Processing and Characterisation, Cordoba, Spain, March 10-11,2002

R. Härle, H. Schweizer, H. Gräbeldinger, **V. Dumitru**, M.Jetter, S. Bader, G. Brüderl, A. Weimar, A. Lell, and V. Härle *„GaN-DFB-Laserdioden: Prozessierung und Untersuchung"* DPG-Tagung , Regensburg, March (2002)

V. Dumitru, R.Härle, H. Schweizer, F. Scholz, A. Ivanov, G. Moutchnik *„A fast and easy tool for optimisation of GaN based laser diodes growth"* DPG-Tagung, Dresden (2003)

A. Ivanov, **V. Dumitru**, G. Moutchnik, H. Schweizer, F. Scholz, *"Strain studies on GaN-based structures on SiC"* 10th European Workshop on Metalorganic Phase Epitaxy, Lecce (2003)

Zusammenfassung

In den letzten Jahren haben die nitridischen Halbleiter auf GaN Basis durch ihre Verwendung in elektro-optischen Bauteilen, die in den spektralen Gebieten grün, blau, violett und ultraviolett arbeiten, viel Aufmerksamkeit erregt.

Die auf diesem Materialsystem basierende Laserdiode, die bei ca. 400 nm emittiert, ist die vielversprechendste Lichtquelle für optische Datenspeicherung hoher Dichte sowie für der nächsten Generation Laserdruckern, um nur einige Anwendungen zu nennen. Trotz des in den letzten Jahren erreichten erheblichen Fortschritts müssen viele Aspekte, die Technologie dieser Bauteile betreffend, noch verbessert werden und die zugrunde liegenden physikalischen Zusammenhänge geklärt werden.

Diese Arbeit beschreibt die Realisierung von Gruppe-III-Nitrid-Laserdioden mit SiC als Substrat aus der Sicht der Bauteilprozessierung und -charakterisierung. Bedeutende Vorteile des leitfähigen SiC als Substrat im Gegensatz zu isolierendem Saphir, das normaler Weise benutzt wird, entstehen durch die Möglichkeit mit einer echten vertikalen Chip-Struktur mit Rückseiten n-Kontakt zu arbeiten und durch die Möglichkeit auf einfache Weise gespaltene Spiegel für die Laserdiode zu realisieren. Weitere Vorteile entstehen durch die höhere thermische Leitfähigkeit von SiC, die eine effektivere Wärmeverteilung erlaubt.

Die Arbeit ist in 5 Teile gegliedert. Nach einer kurzen Einführung in Kapitel 1, werden in Kapitel 2 einige grundlegende Eigenschaften der Gruppe-III-Nitrid-Laserdioden präsentiert. Der erste Teil (2.1) dieses Kapitels gibt einen Überblick über einige der wichtigsten Charakteristiken des III-Nitrid Materialsystems. Es werden spezifische Eigenschaften dieses Materials hervorgehoben, wie z.B. die Anwesenheit starker innerer elektrischer Felder in den epitaktischen Strukturen. Der zweite Teil (Kapitel 2.2) befaßt sich mit grundlegenden Aspekten von Nitrid Laserdioden, wie der Realisierung des vertikalen und

horizontalen Confinement, dem Funktionsprinzip und den physikalischen Eigenschaften von Laserdioden der Typen Fabry-Perot, DFB und DBR.

Kapitel 3 präsentiert Untersuchungen, die für die Etablierung einer Prozeßtechnologie zur Herstellung von Nitrid-Laserdioden auf SiC gemacht wurden. Gemeinsam mit einigen grundlegenden Kontakttheorie- und Literaturbetrachtungen werden die Experimente präsentiert, die zur Realisierung der elektrischen Kontakte (n-Kontakt auf SiC und p-Kontakt auf GaN) gemacht wurden, sowie der Vorgang der Mg-Aktivierung (p-Dotierung in GaN) betrachtet. Nachdem ein verläßliches Vorgehen zur Herstellung der elektrischen Kontakte eingeführt wurde, war es möglich, komplette Bauteile weiter zu prozessieren und zu charakterisieren. Als erstes wurde ein einfacher Prozeß realisiert, um eine schnelle Rückkopplungsmöglichkeit für die Epitaxie zu erhalten (präsentiert in Kapitel 4). Durch Benützen einer Schattenmaske erhielt man Elektroluminiszenzdioden, die zur Untersuchung und Optimierung von verschiedenen Wachstumsparametern hinsichtlich ihres Einflusses auf die elektrischen und optischen Bauteilkennlinien benutzt wurden. In elektrischer Hinsicht wurden verschiedene Ansätze des p-Kontakts und des Wachstums der n-Seiten Bufferschichten untersucht und verglichen, sowie eine InGaN Deckschicht bezüglich der Gasflüsse, Wachstumstemperatur und Schichtdicke optimiert. Die auf diese Weise angepaßten epitaktischen Wachstumsparameter führten schließlich zusammen mit den Verbesserungen, die bei der Prozeßentwicklung der elektrischen Kontakte erhalten wurden, zu einer bedeutenden Erniedrigung des Spannungsabfalls an den hergestellten Laserdioden und zu einem sehr niedrigen differentiellen Widerstand.
Zur optischen Charakterisierung der epitaktischen Schichtstrukturen wurden ebenfalls die durch Schattenmaskentechnologie hergestellten Bauteile herangezogen. Mit Multisegmentbauteilen wurden sowohl Elektrolumineszenzspektren als auch optische Verlustmessungen durchgeführt, um ihre Abhängigkeit vom Magnesium

Dotierprofil im Bereich dicht an der aktiven Zone zu untersuchen.

Kapitel 5 stellt die Ergebnisse vor, die aus der Prozessierung und Charakterisierung von Nitrid Laserdioden mit Multiquantenwellstruktur gewonnen wurden. Im ersten und zugleich größten Abschnitt dieses Kapitels werden Fabry-Perot-Laser betrachtet. Zuerst werden Herstellung und Messungen, die zur Charakterisierung der Bauteile durchgeführt wurden, beschrieben. Danach erfolgt die Präsentation und Diskussion der Ergebnisse, die sowohl aus dem Schwellstromwert und seiner charakteristischen Temperatur, als auch aus der charakteristischen Temperatur der Laserwellenlänge ermittelt wurden. Es werden die Auswirkungen der in diesen Strukturen vorhandenen unvollständig abgeschirmten internen elektrischen Felder, die zu einer Wellenlängenstabilisierung gegenüber Temperaturvariationen führen, diskutiert. An den hergestellten Laserdioden wurden außerdem Untersuchungen zur Verteilung des Stromes durchgeführt. Hierfür wurden Dioden mit verschiedenen Kontaktgeometrien und unterschiedlichen Höhen der Rippenwellenleiter miteinander verglichen. Es konnte gefolgert werden, dass in der n-seitigen Region der epitaktischen Schichtstrukturen eine signifikante Aufteilung des Stromes erfolgt, während in der p-seitigen Region bis zur aktiven Zone ein solcher Effekt vernachlässigbar ist und deshalb die Schwellspannung der hergestellten Dioden nicht beeinflusst. Da sich bei Untersuchungen zu den Eigenschaften bezüglich des Wärmewiderstandes relativ hohe Werte ergaben, wurden einige Verbesserungen mit vielversprechenden Ergebnissen ausprobiert, wie z.B. eine Verdickung der Kontaktmetallisierung oder den Austausch der SiO_2-Isolatorschicht durch eine mit einer besseren Wärmeleitfähigkeit (Al_2O_3).

Abschnitt 5.2 enthält die Realisierung und Charakterisierung einer lateral gekoppelten DFB Nitrid Laserdiode mit einem Gitter zweiter Ordnung. Diese Methode, weltweit erstmals in diesem Materialsystem realisiert, ermöglicht einen einfachen Herstellungsprozeß, der die Notwendigkeit eines epitaktischen

Überwachsschrittes vermeidet, der normalerweise für diese Art von Lasern herangezogen wird. Die erhaltenen DFB Dioden erlaubten die Messung des Brechungsindexes der Struktur und durch die Wahl verschiedener Gitterperioden auch die Messung der Dispersionsrelation der Wellenleiter-Struktur. Desweiteren wurden Anzeichen des unvollständig abgeschirmten internen elektrischen Feldes im Falle von elektrisch angeregten Nitrid Lasern bestätigt. Das Vorhandensein dieses Restfeldes führt zu einer extrem kleinen Wellenlängenverschiebung in Abhängigkeit von der Temperatur.

Zum Schluß wird in Abschnitt 5.3 ein erfolgreicher Test für die Realisierung einer oberflächenemittierenden Nitrid Laserdiode präsentiert. Durch ein Gitter zweiter Ordnung in einer DBR Laserstruktur konnte eine vertikal emittierende Laserdiode hergestellt werden, bei der gänzlich auf Spiegel verzichtet werden konnte. Auch dieses Bauelement wurde für dieses Materialsystem weltweit erstmals realisiert.

1. Introduction

Due to their use in optoelectronic devices operating in green, blue, violet and ultraviolet spectral region III-nitride materials (AlInGaN) have recently become one of the most interesting and hot topics of research for many physicist and engineers.
The blue-violet laser diodes based on this material system stand to satisfy a number of application needs including high-density data storage, high capacity DVD, high-resolution color printing, laser displays, chemical and biological agent detection.
Despite the tremendous progress achieved since the first nitride based laser diode was realized by Nakamura et al. [Nakamura96], many aspects regarding the technology of these devices remain to be improved and the underlying physics issues must be clarified.
This work approaches, from the device processing and characterization point of view, the realization of the multiple quantum well nitride laser diodes epitaxially grown on SiC substrate. Because large size, cheap bulk GaN with sufficient quality is not yet available, the epitaxially grown laser structures currently involves the use of heterosubtrates as sapphire and, to a lesser extent, SiC. While the laser structures growth process on SiC substrate is not so well developed as on the most commonly employed sapphire one, SiC however offers few potential major advantages. By contrast with the isolating sapphire, SiC is a electrical conductive substrate, therefore allows the realization of a true vertical laser diode structure, in which p-type and n-type electrodes are respectively formed on the surface and the bottom of the wafer. This greatly simplifies the fabrication process which is suitable for mass production. Also, SiC substrate allows the fabrication of the laser cavity mirrors by cleavage – in case of sapphire this usually employs a deep etching step – and, having a higher thermal conductivity assures a more effective heat dissipation.
The work is structured in 5 parts. After a short introduction in chapter 1, in chapter 2 there are presented some basic properties of the III-nitride laser diodes. First part (2.1) of this chapter surveys some of the most important characteristics of the III-nitride material. The second part (chapter 2.2) approaches some

basic aspects of nitride laser diodes as the realization of the vertical and horizontal confinement, operation principle and physical properties of the Fabry-Perot, DFB and DBR types of laser diodes.
Chapter 3 presents the investigations done for establishing a process technology for fabrication of nitride laser diodes on SiC. Together with some basic contact theory and literature considerations, experiments done for realization of n-and p-electrical contacts as well as the Mg (p-type dopant in GaN) activation procedure are regarded.
In chapter 4 the realization of an electroluminiscent diode and its utilization as a fast feedback tool for epitaxy is presented. Based on the previously developed contact technology but using a simple, fast shadow-mask approach, the investigation and optimisation of different growth parameters with respect to their influences on the electrical and optical device characteristics was enabled. Different approaches related to the p-contact and n-side buffer layers growth were investigated and compared. Furthermore the InGaN cap layer was optimised with respect to the gas flows, growth temperature and layer thickness.
The epitaxial growth parameters adjusted in this manner, together with the improvements obtained by the electrical contacts process development were finally leading to a significant voltage drop reduction on the fabricated laser diodes and a very low differential resistivity was obtained. The shadow-mask devices were also used for optical characterizations of the epitaxially grown structures. Using a multi-segment device approach both electroluminiscence spectra and optical loss measurements were done. Their dependence of Mg doping profile in the region close to the active zone was also investigated.
Chapter 5 presents the results obtained from the nitride laser diodes processing and charaterization. The first part of this chapter deals with the Fabry-Perot lasers. After describing the fabrication procedure and measurements done for the devices characterization, there are then presented and discussed the obtained results with respect to the threshold current value (5.1.2) and its characteristic temperature (5.1.3), as well as the characteristic temperature of lasing wavelength (5.1.4). The

effect of the incompletely screened internal electric fields present in these structures are evidenced and discussed. They lead to improved wavelength stability under temperature variations. On the realized laser diodes current spreading investigations were also done (5.1.5). By comparing diodes with different contact geometry as well as different ridge waveguide height, it was concluded that while a significant current spreading effect is present in the n-side of the epitaxial structure, such an effect is negligible in the p-side –from the surface down to the active zone – therefore not affecting the threshold current of the fabricated diodes. The processed laser diodes were also investigated with regard to their thermal resistance properties (5.1.6). Because the found values of this parameter were relatively high ones, there were tested, with promising results, some possible improvements, like increasing the contact metalization thickness or exchanging the SiO_2 isolator layer with a better thermal conductive one (Al_2O_3).

The chapter 5.2 presents the realization and characterization of a laterally coupled DFB nitride laser diode with second order grating. This approach, a new one for this material system, allows a simple fabrication procedure, avoiding the need of the epitaxial overgrowth step, typically employed in case of such lasers. The obtained DFB diodes enabled the measurement of the structure's refractive index and, using different grating periods, also of its dispersion relation. Furthermore, it was confirmed the previously evidenced presence of the incompletely screened internal electric fields in the electrically injected nitride lasers, which lead in the case of these devices to an extremely small wavelength shift with temperature.

Finally, in chapter 5.3 a successfully test for realization of a nitride surface emitting laser diode is presented. Employing a second order grating incorporated in a DBR laser structure a vertical emitting laser diode was obtained, avoiding altogether the mirror realization step.

2. Basic properties of nitride laser diodes.

2.1 III- nitrides material system

2.1.1 General properties

The group III-nitrides, aluminum nitride (AlN), gallium nitride (GaN), indium nitride (InN) and their alloys are materials of considerable interest for applications in optoeletronic devices. This is due to their direct bandgap ranging from 1.9 eV for InN - recent reports indicate even a lower one, of ~0.7 eV [Davydov02] - to 3.4 eV for GaN and to 6.2 eV for AlN. Therefore, these materials, together with their ternary alloys could in principle cover almost all the visible and near-ultraviolet regions of the spectrum, as schematically is depicted in figure 2.1.1. The bandgap of ternary alloys $Al_xGa_{1-x}N$ and $In_xGa_{1-x}N$ is given [Hofmann00] by:

$$E_g\left(Al_xGa_{1-x}N\right) = xE_g\left(alN\right) + \left(1-x\right)E_g\left(GaN\right) - b_1x\left(1-x\right) \qquad (2.1.1)$$

$$E_g\left(In_xGa_{1-x}N\right) = xE_g\left(InN\right) + \left(1-x\right)E_g\left(GaN\right) - b_2x\left(1-x\right) \qquad (2.1.2)$$

where E_g is the bandgap energy and b_1, b_2 are the so-called bowing parameters. Moreover, these materials are characterized also by properties like high thermal and chemical stability, low compressibility, high thermal conductivity and high melting temperature. Such properties, from one side, make III-nitrides one of the most promising candidates as materials for applications to light emitters such as light-emitting diodes (LEDs) and laser diodes (LDs) from the UV to the visible region of the spectrum. But, on the other side, their properties also make the growth of high-quality single crystals, the epitaxy of perfect layers and the device processing complicated.
Therefore, in the following, the most important properties of these materials and the related consequences for the devices realization will be briefly surveyed.

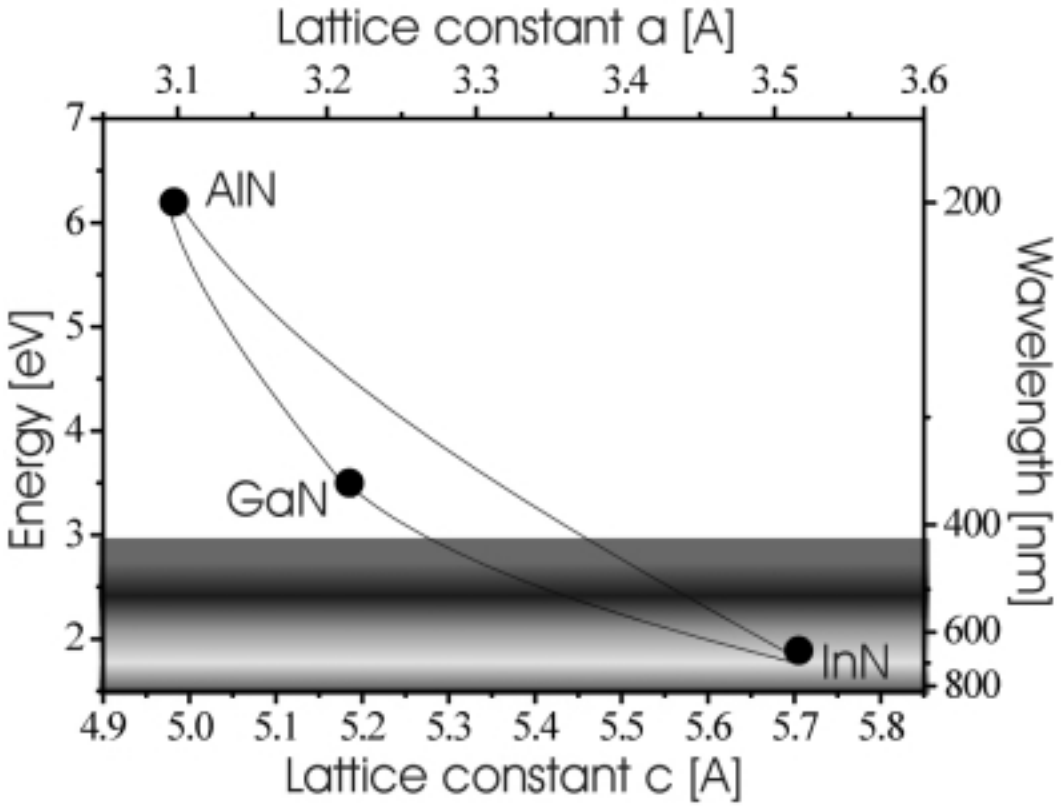

Fig. 2.1.1 Bandgap energies and lattice constants of III-nitrides material system (hexagonal phase)

2.1.2 Crystal structure

There are three common crystal structures shared by the group III-nitrides: the wurtzite (α-phase), zinc-blende (β-phase) and NaCl structure. However, the only thermodynamically stable structure at ambient conditions for AlN, GaN and InN is the wurtzite (hexagonal) one [Edgar94]. The wurtzite structure has a hexagonal unit cell and thus two lattice constants, *c* and *a*, as could be seen from figure 2.1.2 where, as an example, is schematically shown the GaN crystal structure. It contains 6 atoms of each type. The space grouping for the wurtzite structure is $P6_3mc$ (C^4_{6v}). The wurtzite structure consists of two interpenetrating hexagonal closely packed (HCP) sublattices, each with one type of atom, offset along the c-axis by 5/8 of the cell height *c*. Each group III atom is coordinated by four nitrogen atoms and conversely, each nitrogen atom is coordinated by four group III atoms. However, in the real structure of the nitrides the

four tetrahedral bonds around one atom are not equivalent ones, that parallel with the c-axis being different by the others three. This is evidenced by the deviation of the *c*/*a* ratio, and of the cell-internal parameter *u* from those of an ideal structure, as could be seen from the Table 2.1.1 For an ideal closely packed hexagonal structure $c/a=(8/3)^{0.5}=1.633$, and the parameter *u*, which is defined as the length of the bond parallel to the c-axis in units of c_0, has the value of 3/8=0.375 [Ambacher98, 03]. This non-ideality given by the differences in bond lengths lead to the existence of strong polarization fields in these materials, as will be discussed later on.

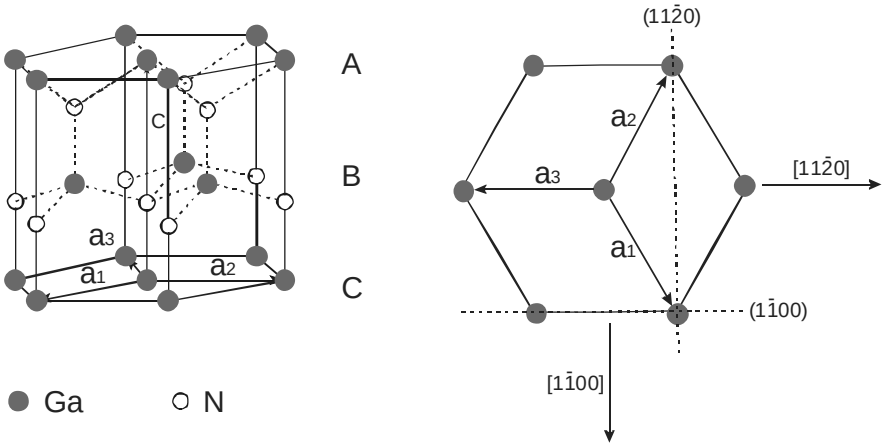

Fig. 2.1.2 Schematic drawing of a wurtzite GaN structure (left). View along the c-axis of the (0001) plane, indicating the crystallographic directions, respectively planes, with high symmetry (right). The Miller indices for a hexagonal lattice are used with the common conventions.

Wurtzite, 300 K	AlN	GaN	InN
a_0 (A)	3.11	3.189	3.54
c_0 (A)	4.98	5.185	5.705
c_0/a_0	1.601	1.6259	1.611
u_0	0.380	0.376	0.377

Table.2.1.1 Lattice constants of AlN, GaN and InN at 300 K [Ambacher98] For an ideal closed packed hexagonal structure *c*/*a*=1.633 and *u*=0.375.

2.1.3 Growth, substrates and doping issues

The above described structural properties have important consequences on the nitrides growth. Because, due to the high temperature melting point and extremely high equilibrium vapor pressure of nitrogen at the growth temperature it is fairly difficult to grow large size bulk crystals, the primary methods of obtaining crystal material rely on growth of epitaxial layers on different substrates at high temperature, the commonly used method for the optoelectronic applications being MOVPE. However, due to their structural properties, it is quite difficult to grow high-quality epitaxial nitride films with a flat surface free of cracks. This is caused by the lack of substrate materials with lattice constants close to that of the nitrides. More than this, a major problem of the heteroepitaxial growth is given by the large thermal mismatch between nitrides and the substrate. The different coefficients of thermal expansion between substrate and nitride introduce residual stress during cooling. These induced stresses can cause additional structural defects and – how will be discussed later on, piezoelectric fields, influencing the optical and electrical properties of films and devices.
Therefore, many different substrates materials have been tried out for nitrides epitaxy, including metals, oxides, nitrides, and semiconductors. A few example could be cited: Al_2O_3, SiC, ZnO, MgO, Mg Al_2O_3, $LiGaO_2$, GaAs, GaP, Si, Hf, Zr, ZrN, TiN, etc…[Miskys03]. However, those which are successfully used for device realization are sapphire (α-Al_2O_3) and SiC (6H-SiC). A comparison of the lattice and thermal properties of these materials respective to those of GaN or AlN –that are commonly used as first layers in an epitaxial nitride structure – could be seen in table 2.1.2.
Despite the fact that, as can be seen, from lattice and thermal properties point of view, SiC is superior to sapphire, the last one is currently more widely used in device fabrication. This is mainly due to the fact that while the epitaxy process is relatively well established on sapphire, on SiC it's still to some extent in the developing course. However, for optoelectronic applications, and especially for laser diodes fabrication, the SiC has also other

potential advantages, which makes it very promising. One of them is its large thermal conductivity (see table 2.1.2), which assures a better heat dissipation from the device by comparison with sapphire, this being a very important issue in the case of a laser diode [Härle00]. Another advantage of SiC as substrate over sapphire is brought by the crystal structure and the nitride epitaxial growth mode. In the case of sapphire, which has a rhombohedral structure, GaN (as representative nitride) is growing with c-axis parallel to the substrate ones. But for minimizing the lattice mismatch, the in-plane GaN lattice is rotated with 30° around the c-axis compared to the sapphire substrate. In consequence, obtaining cavity mirrors by cleavage is extremely difficult. Therefore, the standard approach to realize this laser mirrors is by deep etching. In the case of SiC, which has a wurtzitic structure similar to nitrides, GaN is growing with the same orientation as the substrate. Therefore the laser facets could be obtained by cleavage and this simplifies considerably the device realization process.

Material	GaN	AlN	6H-SiC	sapphire
a(A)	3.189	3.11	3.080	4.758
c(A)	5.185	4.98	15.12	12.991
Thermal conductivity (W/cmK)	1.3	2.85	3.0-3.8	0.5
Thermal expansion coefficient. in-plane (10^{-6}/K)	5.59	4.2	4.2	7.5
Lattice mismatch GaN/substrate (%)	-	2.4	3.5	16
Thermal mismatch GaN/substrate (%)	-	25	25	-34

Table 2.1.2 Material properties of GaN, AlN, sapphire and SiC. Reference [Dadgar03]

Furthermore, in the same direction of processing simplification, SiC is bringing another important advantage. The fact that SiC possesses electrical conductivity allows the realization of a vertical laser diode structure, with the n-contact on the backside. In the case of sapphire, which is an isolator, both p- and n-contacts have to be realized on the top of the epitaxial structure, as can be seen from the figure 2.1.3, where the vertical structure of laser diodes realized using SiC, respectively sapphire as substrates are schematically shown. This complicates the device processing by an additional deep etching step till n-GaN layer on which the n-contact will be realized using a lithographic process. In the case of SiC substrate these problems are completely avoided because the n-contact can be realized just by a backside metalization.
Due to all these potential advantages, the diodes processed during this work have epitaxial structures grown on SiC.

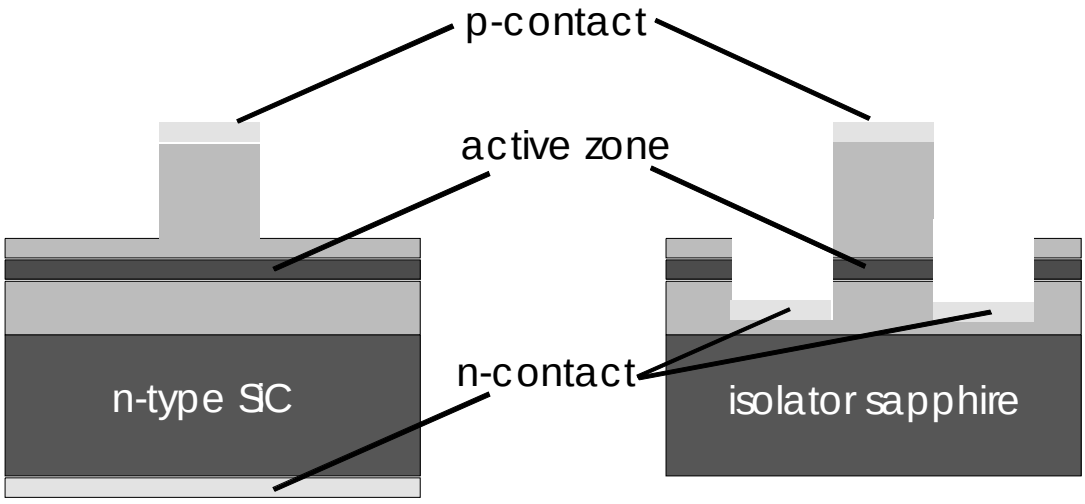

Fig. 2.1.3 Schematic vertical structure of laser diodes realized on SiC, respectively sapphire.

Finally, before leaving this section, it's worth to briefly mention also few aspects related to another very important issue from a laser diode device realization point of view: the doping characteristics of the nitrides. Because in the laser diode structure, as will be later shown, the p-n junction is basically

formed by GaN and AlGaN layers, the discussion will be concentrated on these materials. Firstly, it should be said that the realization of sufficiently n- and p-doped material was one of the factors that were hindering for a long time the use of the nitrides as a suitable material system for device applications. The main difficulty was the realization of p-doped GaN layers. This was due, from one side, due to its large bandgap (>3 eV), but also due to the fact that for a long time the as grown, nominally undoped GaN, was showing n-type conductivity. Responsible for this were the relatively poor quality of the grown material, contamination with oxygen from the growing atmosphere, and the presence of nitrogen vacancies which acted as donors. On the other hand this background n-type doping level was making it easy to obtain a further proper, controllable, n-type material using the dopant Si, which has a donor activation energy of around 12-17 meV in GaN [Ambacher98].

Regarding the p-doped GaN, it was first time successfully obtained in 1989 by Amano and his team [Amano89]. Besides growing high quality material, they have used Mg as dopant and applied a post-growth LEEBI (low energy electron beam irradiation) treatment. This was necessary because, as will be discussed later on in more detail, in the as-grown samples Mg is passivated by hydrogen forming an Mg-H complex which is electrically neutral. However, even since then a huge amount of work was done in this area, the Mg doping, which remains the only successfully method for obtaining device applicable p-GaN material, still possesses a lot of challenges. Besides its passivation by hydrogen – for its removal also other methods like thermal annealing, minority carrier injection, etc… were developed in the mean time - a major obstacle is its large activation energy, around 170 meV. Therefore, up to present the maximum available p-doping of GaN is about $1*10^{18}cm^{-}3$.

Regarding the AlGaN, it is, of course, even more difficult than for GaN to obtain both n- and p-type doping, especially for higher aluminum compositions (>20%).

2.1.4 Internal electrical fields

An important characteristic of the nitrides that influences the device properties is the presence of strong internal electrical fields inside the epitaxial structures. Responsible for these is, on one hand, the structure non-ideality given by the differences in bond lengths, already mentioned in section 2.1.2. This leads to the existence of a non-zero electrical dipole moment oriented parallel to the c-axis, and consequently to a spontaneous polarization directed along the c-axis as illustrated in figure 2.1.4(a).

The strength of the spontaneous polarization in the nitrides is very large and increasing from GaN to InN and AlN due to the increasing non-ideality of the crystal structure. The sign of the spontaneous polarization for the nitrides is found to be negative. Some reported values are -0.081 C/m^2 for AlN, -0.029 C/m^2 for GaN and -0.032 C/m^2 for InN [Bernardini97]. The orientation of the polarization is defined assuming that the positive direction goes from the metal (cation) to the nearest neighbor nitrogen atom (anion) along the c-axis. Therefore in the case of the nitrides the direction of the negative spontaneous polarization points from the nitrogen atom to the metal atom along the c-axis bond.

However, regarding the epitaxial nitrides samples, the direction of the spontaneous polarization is also determined by the polarity, which could be [0001] or [000-1]. By convention the [0001] direction is given by a vector pointing from a Ga (metal) atom toward the nearest-neighbour N atom. Therefore a sample grown in the [0001] direction – [0001] polarity - will have Ga (metal) atoms on the top position of the {0001} bilayer, for this reason this polarity is called “Ga-face”. It should be pointed out that Ga-face does not mean Ga-terminated surface, since a Ga-face surface might be N-terminated if it is covered with nitrogen atoms, but without flipping the crystal it will never be N-faced. In case of the epitaxial nitride films grown by MOVPE, typically the samples are growing in the [0001] direction with Ga-faced surfaces [Ambacher98]. Therefore in this case the spontaneous polarization pointing from the nitrogen toward the Ga (metal)

along the c-axis atom is directed toward substrate as indicated in figure 2.1.4 (b).
Of course, in case of the bulk material, the rearrangement of surface charges nullifies a spatially uniform spontaneous polarization. Consequently, any sample under equilibrium conditions will not exhibit a macroscopic potential difference between their polar surfaces, regardless of any internal fields. Therefore, the effect of the spontaneous polarization fields can only be observed in layered structures such as heterostructures consisting of different compounds. The discontinuity in polarization from one material to the other creates bound charges at the interfaces and consequently an electric field.

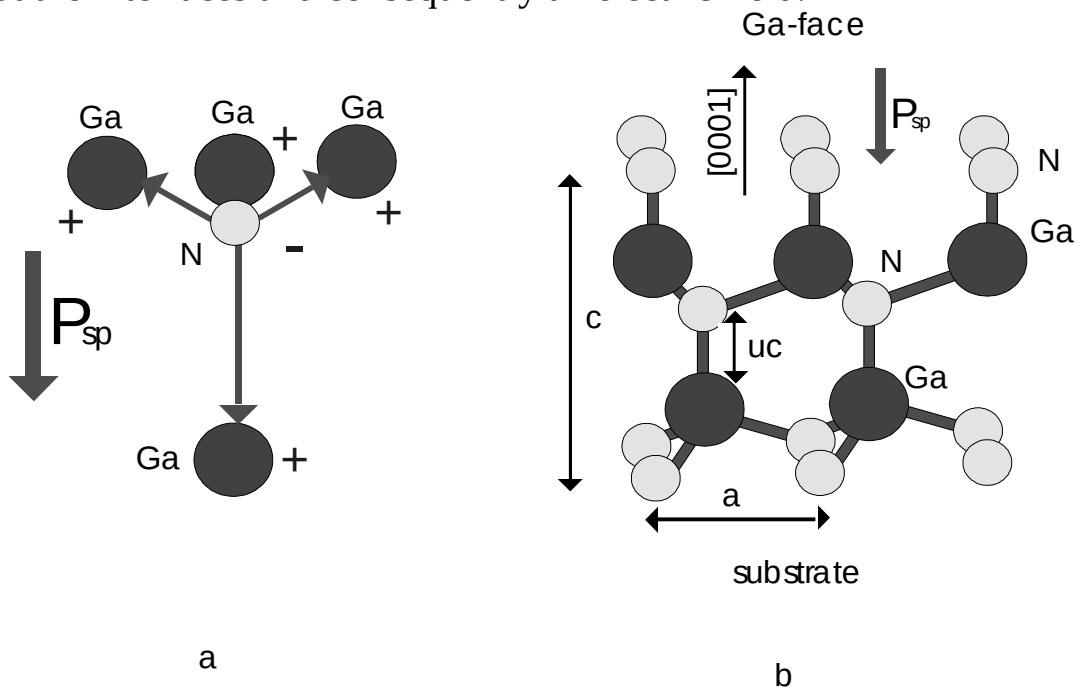

Fig. 2.1.4 (a) Spontaneous polarization induced by the non-ideality of the tetrahedral structure of the nitrides figured schematically for GaN; (b) Crystal structure of GaN with Ga-face polarity and spontaneous polarization

Additionally to the spontaneous polarization, the nitrides, being non-centrosymetric polar crystals, when subject to external stress may generate also piezoelectric fields due to the strain-induced polarization. Due to the significant mismatch in lattice constants and thermal expansion coefficient between nitrides and substrate

but also between nitrides layers with different compositions, the epitaxially grown heterostructures usually presents biaxial strain in the (0001) plane – which is perpendicular to the c-axis. According to growth condition, substrate and layers succession in the vertical structure, the (0001) in-plane strain could vary from compressive to tensile one. A compressive strain means that the lattice constants *a* – the edge length of the basal hexagon – and *c* – the height of the hexagonal prism – are decreased, respectively increased by comparison with their equilibrium values a_0 and c_0. In case of a tensile strain the situation is, of course, inversed. The induced piezoelectric polarization in the direction of the c-axis is then given [Ambacher98] by:

$$P_{PE} = e_{33}\varepsilon_z + e_{31}\left(\varepsilon_x + \varepsilon_y\right) \qquad (2.1.3)$$

where e_{33} and e_{31} are the piezoelectric coefficients, $\varepsilon_z = (c\text{-}c_0)/c_0$ is the strain along the c-axis, and the in-plane strain $\varepsilon_x = \varepsilon_y = (a\text{-}a_0)/a_0$ is assumed to be isotropic. Using the relation between the lattice constants in the hexagonal nitride system

$$\frac{c - c_0}{c_0} = -2\frac{C_{13}}{C_{33}}\frac{a - a_0}{a_0} \qquad (2.1.4)$$

where C_{13} and C_{33} are the elastic constants, the relation (2.3) can be rewritten as:

$$P_{PE} = 2\frac{a - a_0}{a_0}\left(e_{31} - e_{33}\frac{C_{13}}{C_{33}}\right) \qquad (2.1.5)$$

From a microscopic point of view, a strain parallel or perpendicular to the c-axis produces an internal displacement of the metal sublattice with respect to the nitrogen ones, and thus a variation of the parameter *u* of the wurtzite structure. The obtained piezoelectric polarization is due to the effect of the change of the macroscopic lattice constants and to the associated change in *u*.

The piezoelectric coefficients of the nitrides are very large (Table 2.1.3) – up to ten times larger than in GaAs based crystals, their sign being also opposite to other III-V compounds - therefore if nitride layers are under biaxial strain, large piezoelectric polarizations can be generated. The value of the piezoelectric polarization is increasing with strain and for crystals or epitaxial layers under the same strain from GaN to InN and AlN.
The sign of the piezoelectric polarization is, of course, depending on whether the strain is compressive or tensile. Accordingly to relation 2.5, in case of a tensile strain the piezoelectric polarization is negative and in case of a compressive strain is positive. It's evident that this piezoelectric polarization is superimposed to the spontaneous one, and that their orientations could be parallel or antiparallel ones. For a Ga-face polarity crystal and with the above mentioned definition of the polarization sign, in case of a tensile strain the piezoelectric and spontaneous polarizations are parallel ones, being both negative, and in case of the compressive strain their orientations are antiparallel ones.

Piezoelectric constants	AlN	GaN	InN
e_{33} (C/m^2)	1.46	0.73	0.97
e_{31} (C/m^2)	-0.60	-0.49	-0.57

Table 2.1.3 Piezoelectric constants of AlN, GaN and InN. Reference [Ambacher98].

Therefore, generally, in the absence of external electric fields, the total macrocopic polarization P_{total} of the solid is the sum of the spontaneous polarization P_{SP} in the equilibrium lattice and the strain-induced or piezoelectric polarization P_{PE}.

$$P_{total} = P_{SP} + P_{PE} \qquad (2.1.6)$$

As mentioned already, at the interfaces present in a heterostructure the polarization discontinuity leads to the

existence of fixed polarization charges and hence of the locally built-in electrostatic fields. In case of a MQW structure, the electric field in the active layer can be written [Fiorentini99, Strassburg03] generally as:

$$E_w = \frac{L_w\left(P^B_{total} - P^W_{total}\right)}{\varepsilon_0\left(L_B\varepsilon_W + L_W\varepsilon_B\right)} \qquad (2.1.7)$$

where $L_{W,B}$ are the well and barrier thicknesses, $\varepsilon_{W,B}$, and ε_0 are the dielectric constants of well, barrier and vacuum, and $P^W_{total} = P^W_{SP} + P^W_{PE}$, respective $P^B_{total} = P^B_{SP} + P^B_{PE}$ are the total polarization in the well, respective barrier.
As can be seen, in general the polarization field depends on a combination of polarization differences, dielectric constants and geometrical factors. To obtain at least a rough, qualitative, illustration of such an electric field, it's worth to consider a simple case of a GaN/InGaN/GaN quantum well, assuming for simplicity that $L_W << L_B$, and that the GaN (barrier) layers are unstrained. Therefore their piezoelectric polarization $P^{GaN}_{PE} = 0$. In such a case the relation (2.1.7) is becoming

$$E_w = \frac{P^{GaN}_{SP} - P^{InGaN}_{SP} - P^{InGaN}_{PE}}{\varepsilon_0\varepsilon_w} = -\frac{P^{InGaN}_{PE} - P^{diff}_{SP}}{\varepsilon_0\varepsilon_w} \qquad (2.1.8)$$

where $P^{diff}_{SP} = P^{InGaN}_{SP} - P^{GaN}_{SP}$ is expressing the spontaneous polarization difference between InGaN well and GaN barrier materials. Because the spontaneous polarization of GaN and InN is varying (increasing in absolute value from GaN to InN) by only 10%, P^{diff}_{SP} should have a very small value. On the other hand, because the natural lattice constant of the InGaN quantum well material is larger than that of the barrier material, the quantum well is under biaxially compressive strain and should exhibit a large piezoelectric polarization having an opposite orientation to the spontaneous one. Therefore it could be expected that the differential InGaN/GaN spontaneous

polarization $P_{SP}^{diff} << P_{PE}^{InGaN}$ could be neglected by comparison with the piezoelectric polarization. In this case the electric field will be given mainly by the piezoelectric polarization:

$$E_w \approx \frac{-P_{PE}^{InGaN}}{\varepsilon_0 \varepsilon_w} \qquad (2.1.9)$$

Such a situation is schematically illustrated in figure 2.1.5 (for a Ga-face structure). With these assumptions, a strong electric field

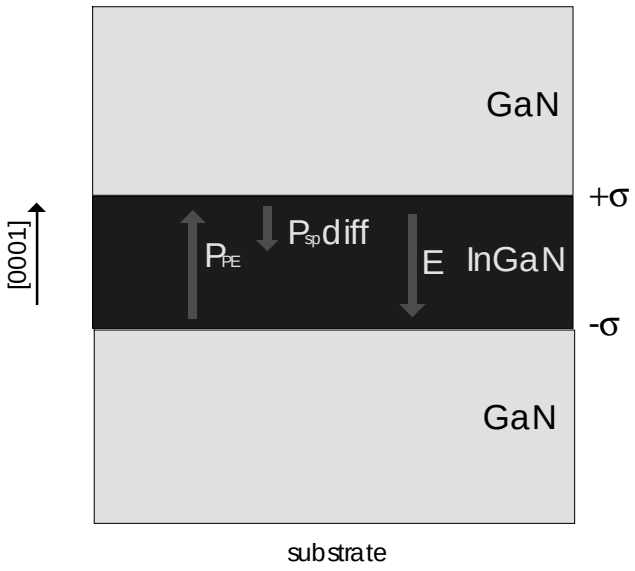

Fig. 2.1.5 Piezoelectric and differential InGaN/GaN spontaneous polarizations in a GaN/InGaN/GaN heterostructure. InGaN layer is under compressive stress and GaN ones are supposed unstrained. The resulting internal electric field in case that the piezo-component is dominant.

directing toward the substrate should be present in the active layer. Indeed, the existence of such a strong electric field oriented toward the substrate in the GaN/InGaN/GaN heterostructures, whose strength reaches even the MV/cm range, was reported by many authors [Wetzel98, Cartwright99, Hangleiter98, etc…].

The presence of such internal piezoelectric field in the nitrides heterostructure give rise to a strong quantum confined Stark

effect (QCSE), leading to a red-shift of the quantum well emission with respect to an ideal square potential well. The effect of the electric field within the quantum well is depicted schematically in figure 2.1.6, which shows also that the electron and the hole wavefunction are localized in opposite corners of the quantum well. Due to the spatial separation of electrons and holes the recombination probability of electron hole pairs will be strongly reduced.
However, under high excitation conditions, the piezoelectric fields will be screened by injected carriers. This should then lead to a blue-shift of the emission and to a recovering of the oscillator strength. In fact, it was considered that only due to this screening effect optical gain and lasing of the nitride laser structures becomes possible [Hangleiter03].

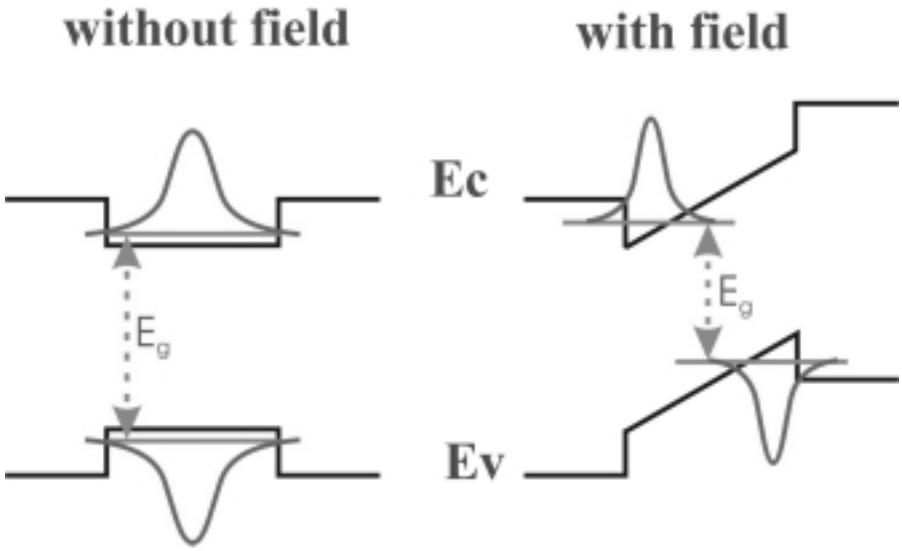

Fig. 2.1.6 Schematic view of a quantum well with built-in field. Electrons and holes are localized in opposite corners, leading to a red-shift of the lowest transition and to a reduction of the oscillator strength compared to the flat band case.

2.2 Nitride laser diodes

2.2.1 Epitaxial structure of InGaN/GaN QW laser diodes. Vertical confinement.

The state of the art nitride laser diodes are realized as separate confinement heterostructure multi quantum well (SCH-MQW) lasers. A vertical structure of such a laser diode could be seen in figure 2.2.1. It shows the typical epitaxial structure employed in this work. Using n-type 6H-SiC as substrate, these structures were grown by low pressure metalorganic vapor-phase epitaxy (MOVPE) at the Stuttgart University (4. Phys. Inst., Crystalographic Lab.) as well as at the company Osram Opto Semiconductors in Regensburg. Without insisting on the epitaxial growth (detailes could be found in [Scholz03, Bader00]), the working principle of such structures will be presented in this chapter. As can be seen from fig.2.2.1, the active zone of such device, consisting of several InGaN/GaN quantum wells placed in the junction region of a p-n heterostructure is sandwiched on both sides by layers having higher bandgap (and lower refractive index). This is the double-heterostructure laser diode concept. The band discontinuities in the conduction and valence bands confine the electrons and holes within the active layer, resulting in more concentrated carriers as compared with the usual homogenous situation where carriers could diffuse over distances of the orders of microns. In this way the so-called “carrier confinement” is realized.
Simultaneously, using the convenient feature of semiconductor physics that increasing the bandgap of the semiconductor by changing its composition also normally decreases its refractive index, such a heterostructure realizes also the “optical confinement” – that means the confinement of the photons closely around the active layer. The larger refractive index of the inner layer in the heterostructure guides the optical wave between the outer layers, resulting in a compression of the optical wave compared with its natural extension in an unbounded medium.
However, for realizing the confinement in an optimal way the optical waveguide should have a relatively large thickness. For

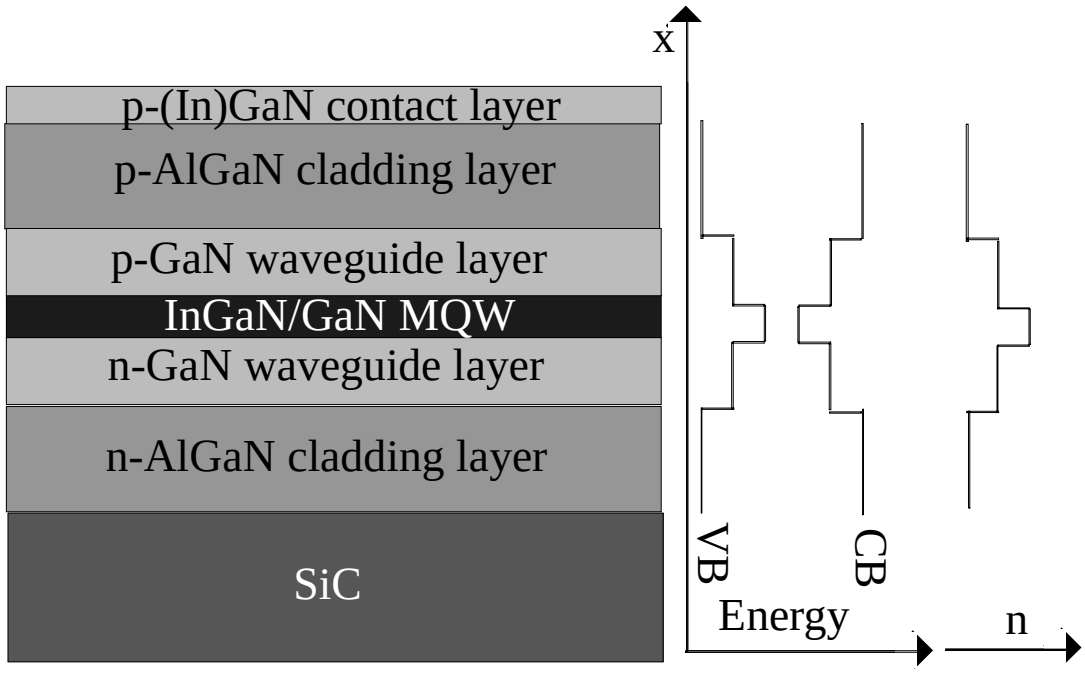

Fig. 2.2.1 Vertical structure of the InGaN/GaN QW laser diodes on SiC. Schematics of the energy and refractive index profiles associated with the separate confinement heterostructure design of these laser diodes. The additional substrate, p-contact layer, and –not depicted - electrons blocking layer and contacts metallizations are not considered in these diagrams.

very thin layers – as the active ones in case of the quantum well lasers – the optical wave is less confined in the heterostructure. It leaks into the confining layers or even into substrate and contact metalizations where it could be strongly absorbed. To overcome this effect while retaining quantum wells as active layers, it is used the separate confinement heterostructure (SCH) scheme where optical confinement is provided by a set of optical confinement layers, while carrier confinement in the quantum well occurs in another imbedded layer. In case of the presented structure, the optical confinement is realized by the AlGaN/GaN system. These layers act as a slab waveguide confining the photons through total internal reflection. This is schematically illustrated in figure 2.2.2, where the two GaN waveguide layers and the thin active zone (from figure 2.2.1) are compactly represented by a single GaN waveguide layer. Total internal

reflection requires that the refractive index of the outer material n_2 is smaller than the refractive index of inner ones n_1. A guided ray has to propagate at a sufficiently shallow angle to the active region, and from Snell's law, the angle of incidence $\theta > \theta_{critical}$. Therefore one may write:

$$\sin\Theta > \sin\Theta_{critical} = n_2 / n_1 = 1 - \Delta n / n_1 \tag{2.2.1}$$

where $\Delta n = n_1 - n_2$. The angle Φ from figure 2.8 then has to be glancing such that:

$$\Phi = (\pi / 2 - \Theta) < \cos^{-1}(1 - \Delta n / n_1) \tag{2.2.2}$$

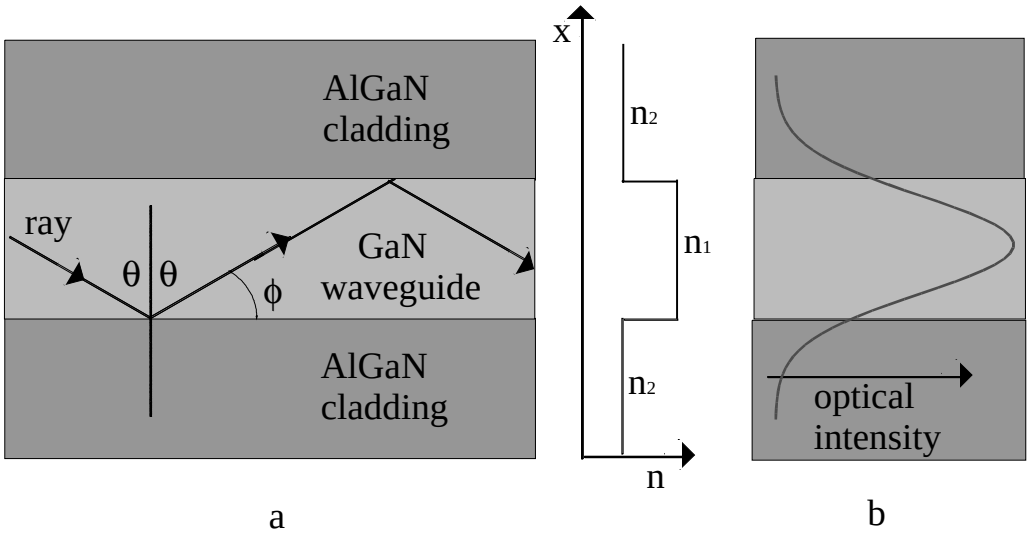

Fig.2.2.2 Rays and intensity for vertical confinement of optical fields. (a) optical-ray picture illustrating the total internal reflection; (b) field or modal picture.

However, only a small part of the light field oscillating along the thin QW is confined in the active layer. The confined part of the field in the active region is given by the optical confinement factor Γ which is defined for T.E. modes as:

$$\Gamma = \frac{\int_{active} E^2(x)dx}{\int_{-\infty}^{+\infty} E^2(x)dx} \qquad (2.2.3)$$

It depicts the overlap of the optically guided wave with the quantum wells, therefore it will describe which fraction of the photons of the guided optical wave interacts with the active or passive layer material: when g is the volume gain per unit length of the active material, the amplification of the optical wave is Γg per unit length. If α_g is the loss per unit length in the active material $\Gamma\alpha_g$ is the loss per unit length of a guided wave. Conversely, 1-Γ is the fraction of the optical wave outside the active material and $(1-\Gamma)\alpha_o$ will be the loss of the optical wave per unit length if the α_o is the absorption coefficient of the confining material at the lasing wavelength.

2.2.2 Structures for lateral confinement

Besides the vertical carrier and optical confinement mentioned above which have operated perpendicular to the junction plane, in the laser diodes could be realized also a so-called horizontal or lateral confinement operating in the junction plane. Figure 2.2.3(a) illustrates one simple way of providing this lateral optical and electron confinement in a laser [Carrol98]. The p-contact is made at the top of the laser through a stripe, etched through an insulating oxide - typically SiO_2 – and although the current spreads out sideways under this contact, peak carrier densities are achieved under the middle of the contact. The optical guiding in the junction plane in such structures is determined mainly by the gain guiding. In this case the optical waveguide structure is formed by surrounding a region of optical gain with a region of optical loss. The optical behavior in such a guide can be analyzed by an extension of the treatment used for a dielectric waveguide, in which is used the complex refractive index $n=n_r + jn_i$, with $g=n_i\omega/c$. However, even if relatively simple to manufacture, this type of lasers called “oxide-stripe” could be affected by problems like current spreading and weak guiding

which lead to high threshold currents, unstable modes and non-linear light-current characteristics.

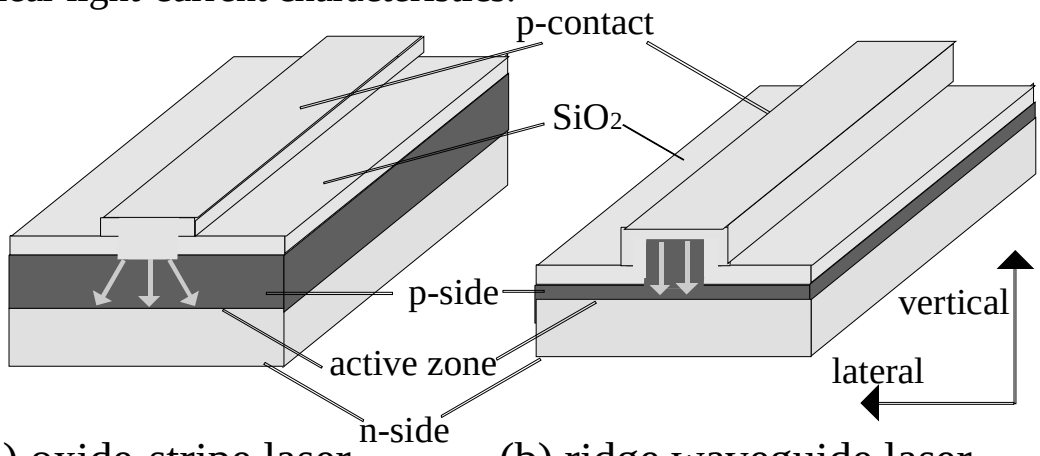

Fig. 2.2.3 Schematic illustration of (a) gain-guided and (b) index-guided structures for providing lateral confinement.

Another way for obtaining the lateral confinement is to realize a ridge waveguide laser as illustrated in figure 2.2.3(b). The ridge is fabricated on the p-side of the structure by etching. In this way one obtains an index-guided structure in which in the lateral direction the ridge is sandwiched between layers with lower refractive index. At the same time the carrier flow is laterally restricted only to the ridge, except the region placed just above the active zone which was not etched. Generally, the ridge is not passing through the active zone in order to avoid the formation of etching induced defects which could act as non-radiative recombination centers. Even if, practically, the ridge lasers are not so easily fabricated as the oxide-stripe ones, they have superior performances due to the better confinement of carriers and photons.

2.2.3 Fabry-Perot lasers. Oscillation condition.

A basic requirement for obtaining laser activity is to provide the laser diode with an optical feedback. In the simplest laser diodes, the Fabry-Perot ones, this is realized by a pair of reflector mirrors facing each other (figure 2.2.4), which build together with the active material a resonator. For obtaining the oscillation

Fig. 2.2.4 Schematic representation of a Fabry-Perot resonator

conditions, let's consider the plane optical waves traveling back and forth along the length of the laser. These waves have optical frequencies $\omega=2\pi f$ with an associated propagation constant $\beta=2\pi/\lambda_m$ where λ_m is the wavelength in the material. Such a wave starting from the left-hand reflector and traveling to the right is referred to as a forward wave and has its phase and amplitude written in complex form:

$$E_f(z) = E_0 e^{(g-\alpha_i)z} e^{-j\beta z} e^{j\omega t} \qquad (2.2.4)$$

The amplitude decays or grows with distance because, as mentioned above, the wave suffers scattering and other fixed losses α_i per unit length, but also experiences a material optical gain g per unit length caused by the electrons and holes being stimulated to recombine. Considering that the laser is of length L and that there is zero phase change on reflection from the partially reflective facets at either end, the forward wave has at the right facet (z=L) a fraction R_{right} reflected and this fraction now travels back, from right to left. Accordingly to eqn. 2.2.4, these reverse fields are described by:

$$E_r(z) = \left\{E_0 e^{(g-\alpha_i)L} e^{-j\beta L}\right\} e^{(g-\alpha_i)(L-z)} e^{-j\beta(L-z)} \tag{2.2.5}$$

where the time variation $e^{j\omega t}$ occurring in all terms was implicitly included.
The reverse wave now travels back to the left facet (z=0) and a fraction R_{left} is reflected to form the forward wave. For stable resonance, the amplitude and phase after this single whole round trip must be identical to the phase and amplitude for the wave when it started:

$$E_0 = E_0 R_{left} R_{right} e^{(g-\alpha_i)2L} e^{-j2\beta L} \tag{2.2.6}$$

This is giving the amplitude condition for stable oscillation:

$$R_{left} R_{right} e^{2(g-\alpha_i)L} = 1 \tag{2.2.7}$$

which could be also written as:

$$g = \alpha_i + \frac{1}{2L} \ln\left(\frac{1}{R_{left} R_{right}}\right) \tag{2.2.8}$$

where the logarithmic term can be considered as a distributed reflector loss α_m. Taking also into account that only a fraction of the photons of the guided optical wave interacts with the active region, therefore considering the optical confinement factor Γ, the eqn. (2.2.8) should be written as:

$$\Gamma g = \alpha_i + \frac{1}{2L} \ln \frac{1}{R_{left} R_{right}} = \alpha_i + \alpha_m \tag{2.2.9}$$

with, as already mentioned

$$\alpha_i = \alpha_0(1-\Gamma)+\alpha_g\Gamma \qquad (2.2.10)$$

$$\alpha_m = \frac{1}{2L}\ln\frac{1}{R_{left}R_{right}} \qquad (2.2.11)$$

where α_i is the loss due to absorptions inside the guide α_g, and outside α_0.

Simultaneously with eqn (2.2.7) must be met also the "phase" condition:

$$e^{-j2\beta L} = 1 \Rightarrow 2\beta L = 2m\pi \qquad (2.2.12)$$

where m is an integer (m=1,2,3…) which determines the longitudinal - or Fabry-Perot - mode number. Therefore, the Fabry-Perot mode becomes a discrete mode depending on the cavity length and waveguide parameters, with the mode spacing – the wavelength difference between adjacent modes – given by:

$$\Delta\lambda = -\frac{\lambda^2}{2n_{eff}L\left[1-\left(\lambda/n_{eff}\right)\left(dn_{eff}/d\lambda\right)\right]} \qquad (2.2.13)$$

with n_{eff} being the effective refractive index of the laser structure.

2.2.4 Threshold current. Output power and differential quantum efficiency.

Assuming that on the laser diode is applied a voltage V, the correspondent injection current being I, the current density will be

$$j = \frac{I}{wL} \qquad (2.2.14)$$

where w is the width of the active region in the lateral direction and L is the cavity length of the laser diode. The carrier concentration in the active region is determined by the rate equation, which neglecting the carrier diffusion is:

$$\frac{\partial n}{\partial t} = \frac{j}{qd} - R(n) \qquad (2.2.15)$$

where the first term on the right-hand side accounts for the carrier injection into the active region with a thickness d, and the second term $R(n)$ accounts for the carrier recombinations due to both radiative and nonradiative processes. Therefore, at steady state:

$$\frac{j}{qd} = R(n) \qquad (2.2.16)$$

The recombination rate is given by:

$$R(n) = A_{nr}n + Bn^2 + Cn^3 + R_{st}N_{ph} \qquad (2.2.17)$$

where the first term is due to nonradiative processes, Bn^2 is due to the spontaneous radiative recombination rate, Cn^3 accounts for nonradiative Auger recombinations, and the last term accounts for stimulated recombination that leads to emission of light and it is proportional to the photon density N_{ph}.
The coefficient for stimulated emission rate is

$$R_{st} = v_g g(n) \qquad (2.2.18)$$

where v_g is the group velocity and $g(n)$ is the gain coefficient.
Below the threshold, the term $R_{st}N_{ph}$ could be ignored since the photon density is small, and then:

$$R(n) = \frac{n}{\tau_e(n)} \qquad (2.2.19)$$

where the carrier lifetime $\tau_e(n)$ is given by

$$\tau_e(n) = \frac{1}{A_{nr} + Bn + Cn^2} \qquad (2.2.20)$$

Therefore, below the threshold, the current density could be written as

$$j = \frac{qdn}{\tau_e(n)} = qd(A_{nr} + Bn^2 + Cn^3) \qquad (2.2.21)$$

With an increase in the injection current density *j*, the gain will increase due to the increase of the carrier concentration *n*. When the threshold condition is reached, the carrier concentration *n* will be pinned at the threshold value n_{th} since the gain is pinned accordingly to eqn.(2.2.9) at the threshold gain $g_{th}=(\alpha_i + \alpha_m)/\Gamma$. Therefore at the threshold

$$j = \frac{qdn_{th}}{\tau_e(n_{th})} = qd(A_{nr} + Bn_{th}^2 + Cn_{th}^3) \qquad (2.2.22)$$

Below the threshold, the output light consists mainly of spontaneous emission and its magnitude is governed by Bn^2. A further increase in the injection current density above threshold leads to the light emission through the stimulated emission process:

$$\begin{aligned} j &= qd(A_{nr} + Bn_{th}^2 + Cn_{th}^3) + qdR_{st}N_{ph} \\ j &= j_{th} + qdv_g g_{th} N_{ph} \end{aligned} \qquad (2.2.23)$$

where $R_{st} = v_g g(n) = v_g g_{th}$ since n is pinned at n_{th}. Therefore,

$$N_{ph} = \frac{1}{qdv_g g_{th}}(j - j_{th}) \qquad (2.2.24)$$

The photon lifetime τ_p is defined as:

$$\frac{1}{\tau_p} = v_g(\alpha_i + \alpha_m) = v_g \Gamma g_{th} \qquad (2.2.25)$$

which accounts for the loss rate of the photons in the laser cavity due to absorption and transmission. With this it's obtained that

$$\frac{N_{ph}}{\tau_p} = \frac{\Gamma}{qd}(j - j_{th}) \qquad (2.2.26)$$

The optical output power P_{out} versus the injection current is determined by:

$$P_{out} = \hbar\omega N_{ph} \frac{Lwd}{\Gamma}(v_g \alpha_m) \qquad (2.2.27)$$

where $v_g \alpha_m$ is the escape rate of the photons and the ratio term is the effective volume of the optical mode. Therefore:

$$P_{out} = \hbar\omega v_g \alpha_m \frac{\tau_p}{q}(j - j_{th})Lw = \frac{\hbar\omega}{q}\frac{\alpha_m}{\alpha_m + \alpha_i}(I - I_{th}) \qquad (2.2.28)$$

However, in this expression of the output power is not taken into account the internal quantum efficiency (it was assumed to be one). The internal quantum efficiency η_i is defined as the percentage of the injected carriers that contribute to the radiative recombinations:

$$\eta_i = \frac{Bn^2 + R_{st}N_{ph}}{An + Bn^2 + Cn^3 + R_{st}N_{ph}} \qquad (2.2.29)$$

and generally $\eta_i < 1$, so eqn. (2.2.28) should be modified as:

$$P_{out} = \frac{\hbar\omega}{q}\frac{\alpha_m}{\alpha_m + \alpha_i}\eta_i(I - I_{th}) \qquad (2.2.30)$$

The external differential quantum efficiency η_e is defined as:

$$\eta_e = \frac{dP_{out}/dI}{\hbar\omega/q} = \eta_i\frac{\alpha_m}{\alpha_m + \alpha_i} \qquad (2.2.31)$$

2.2.5 DFB and DBR laser diodes.

One of the problems encountered in GaN based laser diodes is related to the optical feedback. As already described, in a Fabry-Perot laser this is provided by the laser cavity mirrors. In the case of GaN based lasers, due to the low effective refractive index (~2.5) the cavity mirror has a low reflectivity (~19%). Therefore, typically, in case of a Fabry-Perot laser diode it is necessary to apply subsequent high-reflective mirror coatings. Furthermore, the mirrors realization itself is a difficult processing step. In the case of sapphire substrate this has to be realized by etching. In the case of SiC substrate, even if the mirrors are obtained by cleavage, this procedure is not very easy due to hardness, bad cleavability and hexagonal structure of SiC.
An attractive solution to overcome the problems related to the optical feedback realization is to use an optical grating that is incorporated into the heterostructure waveguide. In this case the grating-induced refractive index perturbations lead to a coupling between the forward and backward propagating waves of the particular laser mode. Therefore the optical feedback is not localized at the cavity end facets but instead is distributed throughout the entire laser cavity (Distributed Feedback – DFB

lasers) or only part of it (Distributed Bragg Reflector – DBR lasers). Another advantage of this optical feedback approach is brought by its wavelength selectivity. This improve the single longitudinal mode operation of these types of lasers by comparison with the Fabry-Perot ones in which the only longitudinal mode discrimination is that provided by the gain spectrum itself which, being much wider than the spacing between resonances, is not very selective.
Without entering in the detailed theory of the DFB and DBR lasers (excellent references could be found for example in [Suematsu94, Carrol98]) will be only surveyed the working principle of these devices. For this, let's consider a diffraction grating embedded into a semiconductor waveguide, as schematically is illustrated in figure 2.2.5.

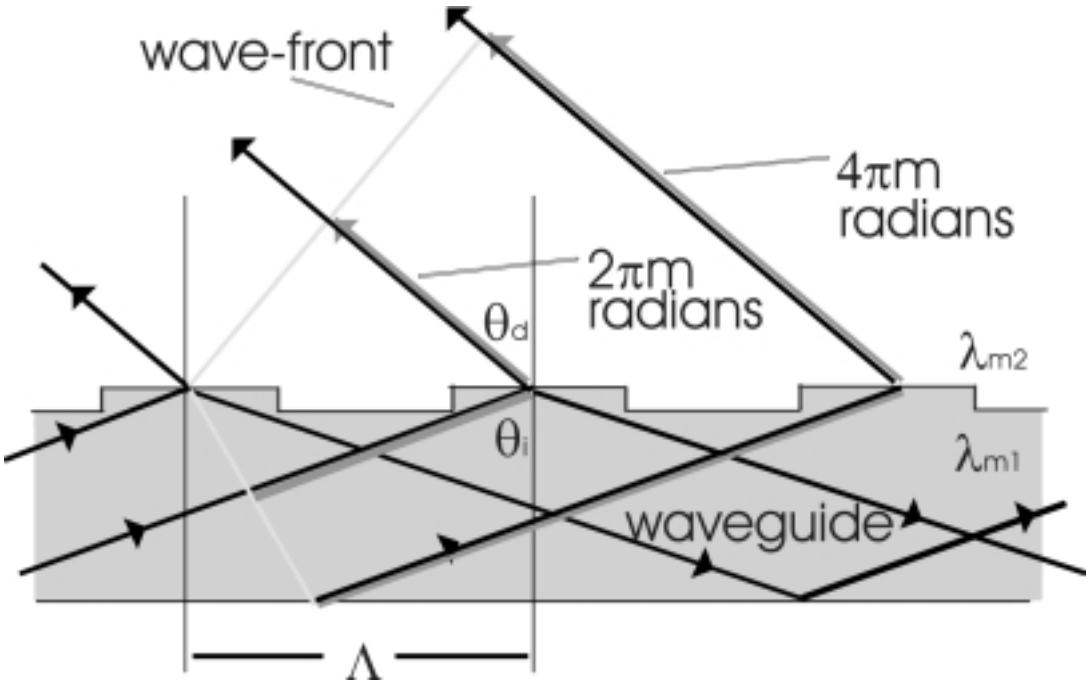

Fig. 2.2.5 Diffraction form grating embedded in a laser waveguide. In such a situation, the incidence angle $\theta_i \sim \pi/2$ and for feedback the diffracted wave emerges at $\theta_d \sim \pi/2$. However, one can also have $\theta_d \sim 0$ when the diffracted wave gives radiation out from the guide. Reference: [Carrol98].

A plane incoming wave is incident at an angle θ_i and the *m*-th order diffracted plane wave emerges at the angle θ_d. Using the Huygen's construction for constructive interference from 'identical' points but at different periods of the grating, one requires the sum or difference of the total optical path in radians to be integer multiples of 2π. With the notations used in figure 2.2.5 one gets:

$$\frac{\Lambda \sin \Theta_i}{\lambda_{m1}} + \frac{\Lambda \sin \Theta_d}{\lambda_{m2}} = m \qquad (2.2.32)$$

The integer *m* defines the diffraction order. At the same time, it should be taken into account that for applying this result to a propagating optical mode in a laser waveguide, the angle of incidence θ_i cannot be less than the critical angle for total internal reflection $\theta_{critical}$ so that:

$$\sin \Theta_i \geq \sin \Theta_{critical} = \frac{n_2}{n_1} = \frac{\lambda_{m1}}{\lambda_{m2}} \qquad (2.2.33)$$

where n_1 and n_2 are the refractive indices in the central and outer regions of the waveguide, respectively. Inserting eqn. (2.2.33) into eqn. (2.2.32) it's obtained:

$$\sin \Theta_d \geq \left(\frac{\lambda_{m2} m}{\Lambda} - 1 \right) \approx \left(\frac{2m}{q} - 1 \right) \qquad (2.2.34)$$

where an integer $q = \Lambda/(\lambda_m/2)$ defines the grating order. Because of the small differences in the refractive index, could be considered that $\lambda_{m1} \sim \lambda_{m2} \sim \lambda_m$, the effective wavelength in the guide. Generally, for a laser with feedback along the waveguide it's necessary that $\theta_d \sim \theta_i \sim \pi/2$. From eqn. (2.3.34), using the equality sign and $\sin \theta_d = 1$, this requires that the order *q* of the grating equals the order *m* of the diffraction. Given the physical

periodicity Λ of the grating, the optimum free-space wavelength λ_b which is most strongly reflected is called the Bragg wavelength and satisfies the Bragg condition:

$$m\frac{\lambda_b}{n_{eff}} = 2\Lambda \qquad (2.2.35)$$

where n_{eff} is the mean value of the refractive index in the guide and relates the free-space Bragg wavelength λ_b with the corresponding guide wavelength $\lambda_m = (\lambda_b/n_{eff})$.
Anyway, it is also possible to find gratings where $\sin\theta_d \sim 0$ – when $q = 2m$ – or $\sin\theta_d$ is significantly less than 1 so that the diffracted wave is radiated away from the guide. Of particular interest is the second-order grating where $q = 2$ because this can be used to couple light from a laser out into the direction perpendicular to the junction to form a surface-emitting laser. While a first-order grating with a period of one-half a guide wavelength gives optical feedback in the first diffraction order, a second-order grating radiates normal to the grating in the first diffraction order but gives feedback in the second diffraction order. Generally, feedback is obtained from a grating of order N in diffraction order N, but diffraction orders intermediate between 0 and N result in radiation loss for such a grating. Because second-order gratings have larger dimensions than first-order ones, they are easier to fabricate. In the case of the GaN based laser diode structures, with an effective refractive index value of around 2.5 and an emission wavelength at around 410 nm, accordingly to the Bragg condition - eqn. (2.2.35) – the grating period Λ should be about 80 nm for the first-order grating and 160 nm for second-order ones. Therefore, even in the latter case, the fabrication of such a grating is not a trivial process.
By inserting such a grating inside a laser diode, as already mentioned, the lumped reflections from the end facets of the Fabry-Perot laser are replaced by the grating's multiple tiny reflections adding in-phase at the operating wavelength. The reflections could be distributed throughout the entire laser cavity,

this being the distributed feedback laser (DFB) concept schematically shown in figure 2.2.6a, or only at the ends of the laser cavity, as in the distributed Bragg reflector (DBR) approach illustrated in figure 2.2.6b. As can be seen, in the latter case, of

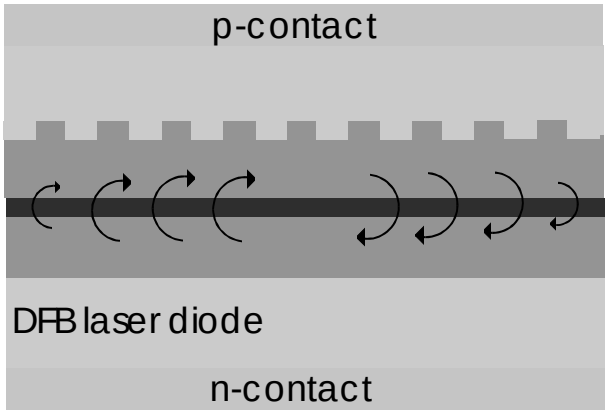

Fig. 2.2.6a Schematic diagram of a distributed feedback (DFB) laser diode.

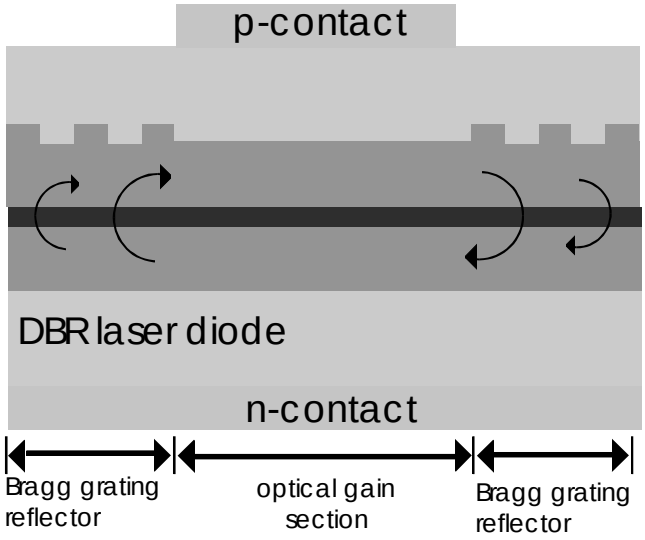

Fig.2.2.6b Schematic diagram of a distributed Bragg reflector (DBR) laser diode.

the DBR structures, the gain (active) and reflection regions are spatially separated. Therefore, such a laser is essentially identical to a Fabry-Perot ones, whose mirrors are replaced by the distributed Bragg reflectors, so that the mirror reflectivities

become wavelength dependent. This is because the grating's multiple reflections give significant feedback only around the Bragg frequency determined by the grating period. Thus, the lasing mode is determined only by parameters of the distributed reflector.

In case of DFB lasers the active and reflection regions are not spatially separated anymore (see fig 2.2.6a), the continuous feedback being combined with gain. Therefore, an optical wave traveling in one direction is continuously scattered into the optical wave in the reverse direction. Both waves grow as they travel towards their respective facets because of the feedback and gain.

The in-depth analysis of these devices requires the investigation of the wave propagation in periodic structures. This is described by the wave equation [Thompson80]:

$$\frac{d^2E}{dz^2} + \beta^2(z)E = 0 \qquad (2.2.36)$$

where z is the propagation direction and where the propagation constant $\beta(z)$ is a periodic function of z. Because the refractive index could have generally a complex form $n=n_{eff} + jn_i$, with the $g=n_i\omega/c$, the propagation constant could be written as:

$$\beta = \pm\left(\frac{\omega}{c}n_{eff}(z) + jg(z)\right) \qquad (2.2.37)$$

As can be seen, in the general case, besides a periodic variation of the real part of the refractive index, should be taken into account also a possible periodic gain. Physically, such a periodic gain can be obtained, for example, if the grating is etched down into the gain region [Schreiner02]. Therefore, one can distinguish different types of Bragg grating based lasers:

(a) passive periodic waveguide structures. In this case the real part of the refractive index is modulated and the imaginary one,

the gain is zero. Such a structure could be already seen in the case of DBR lasers.
(b) lasers with 'pure index grating', where the real refractive index is modulated at constant gain. In case of the DFB lasers with such grating, it's used also the notion of 'index-coupling'.
(c) lasers with 'pure gain grating', where the gain is modulated at constant real refractive index. The DFB lasers of this kind are called 'gain-coupled'.
(d) 'complex-coupled' lasers. In this case both the real and imaginary parts of the complex refractive index are modulated.

For solving the wave equation (2.2.36) one possible approach is given by the coupled wave theory of Kogelnik and Shank [Kogelnik72]. Even if useful for determining some important characteristics of the Bragg grating based devices like for example the coupling coefficient, its applicability is somewhat limited due to the assumption of sinusoidal, not to strong perturbation of the refractive index. Another possible approach is given by the transfer-matrix theory [Björk87] in which the resonator is divided in domains where refractive index and gain are constant, the domain's boundary conditions are expressed in a matrix form and then the entire resonator is modeled as a matrices product. By using this method it's possible, for example, to find out the lasers spectral characteristics. Without entering in more details, will be pointed out only some important laser properties and parameters obtained by these methods.
One fundamental parameters of the Bragg grating lasers is the coupling coefficient k between the counterunning waves in such resonators. Introduced in the coupled wave theory, it could be considered a measure of the interaction between the grating and the light waves. Generally, it has a real component k_i describing the index coupling due to the real refractive index modulation and an imaginary one k_g describing the gain coupling through the modulation of the gain:

$$k = k_i + jk_g \qquad (2.2.38)$$

It is depending on the grating's modulation depth, teeth shape and line to space ratio. For a rectangular grating of order *m* having a line to space ratio w/Λ one finds from Fourier analysis [Hofmann00]:

$$k = \left(\frac{2\Delta n}{\lambda_b} + j\frac{\Delta g}{\pi} \right) * \frac{1}{m} \left| \sin\left(m\pi \frac{w}{\Lambda} \right) \right| \qquad (2.2.39)$$

where Δn and Δg are the real refractive index, respectively gain periodic perturbations. The presence of the line to space ratio in the coupling coefficient expression could be easily understood if it is considered for example an index grating of second order taking into account also the phase shift at the partial reflection of the light waves at the interface between low/high refractive index media. Such a situation is schematically shown in figure 2.2.7. In order to obtain constructive interference, the phase difference between the reflected waves arriving at the reference point z should be integer multiples of 2π. It is evident that in this case, for a second order grating, this is possible only for a line to space ratio w/Λ of 0.25 or 0.75. For w/Λ = 0.5 the interference is a destructive one (see eqn.2.2.39).

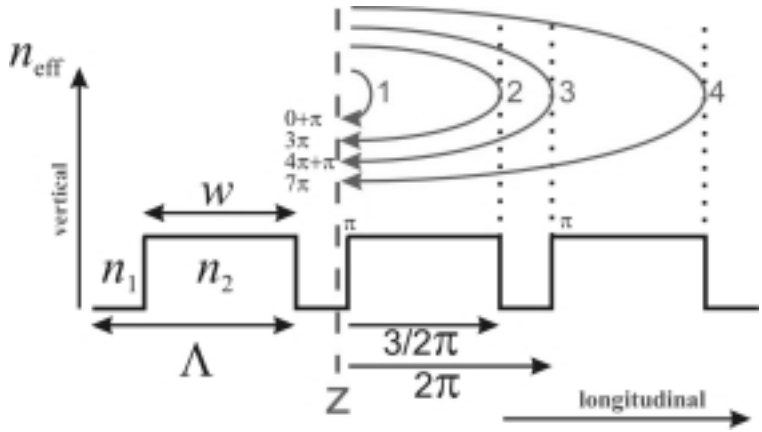

Fig. 2.2.7 Schematic representation of the optical feedback in a second order grating.

This requirement imposes however difficulties from practical realization point of view, because it is not always easy to obtain the exactly desired line to space ratio, altering thus the coupling

coefficient of the fabricated device. However, the real etched gratings show always Fourier components which result in a non-zero *k* even in the case of the w/Λ = 0.5.
Other important characteristic of the Bragg grating lasers which should be mentioned, even only briefly, regards their expected emission spectra. In case of DBR lasers, which, as already explained, are basically identical with the Fabry-Perot ones but having wavelength dependent mirror reflectivities, the lasing wavelength is given by the Bragg one (provided that inside the mirrors loss stopband is not more than one Fabry-Perot mode). In the case of the DFB lasers, the situation is a little different, depending on the coupling characteristics. While in the case of a pure gain coupling, the lasing wavelength is again expected at the Bragg wavelength, for a pure index coupling the feedback is in antiphase at the Bragg wavelength, therefore giving rise to a stopband having the width:

$$\Delta\lambda_s = \frac{\lambda_0}{\pi n_{eff}} k \qquad (2.2.40)$$

where k is the coupling coefficient. The presence of a stopband could be intuitively understood if there are considered the forward and backward propagating waves in a DFB resonator with pure index coupling.

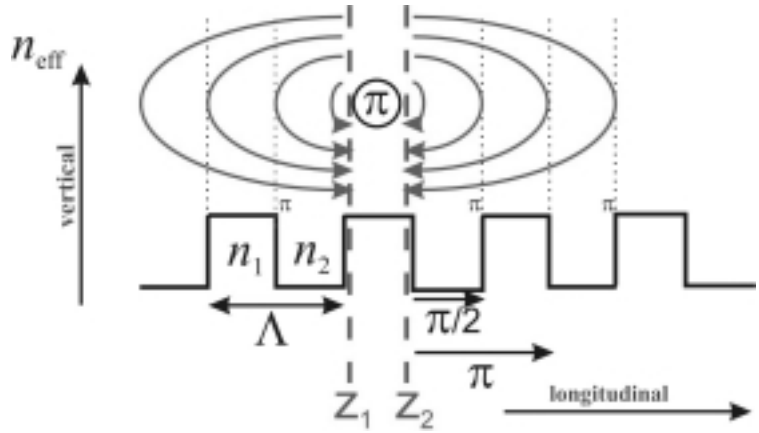

Fig. 2.2.8 Schematic representation of the forward and backward propagating waves in a DFB resonator with pure index coupling.

Taking for simplicity a first order grating and considering a $\lambda_m/4$ long section of it, as illustrated in figure 2.2.8, it is clear that, even if the waves arriving from the left-side at the point z1 add in phase, and similar that coming from the right-side at point z2, for a total round trip –starting and ending at, let's say, point z1 - the waves has to pass also two times the $\lambda_m/4$ long section. This gives an additional phase shift of π and so prevents lasing at the Bragg wavelength. Therefore, such a DFB with a pure index coupling has two longitudinal modes with equal threshold gain on both sides of the Bragg wavelength.

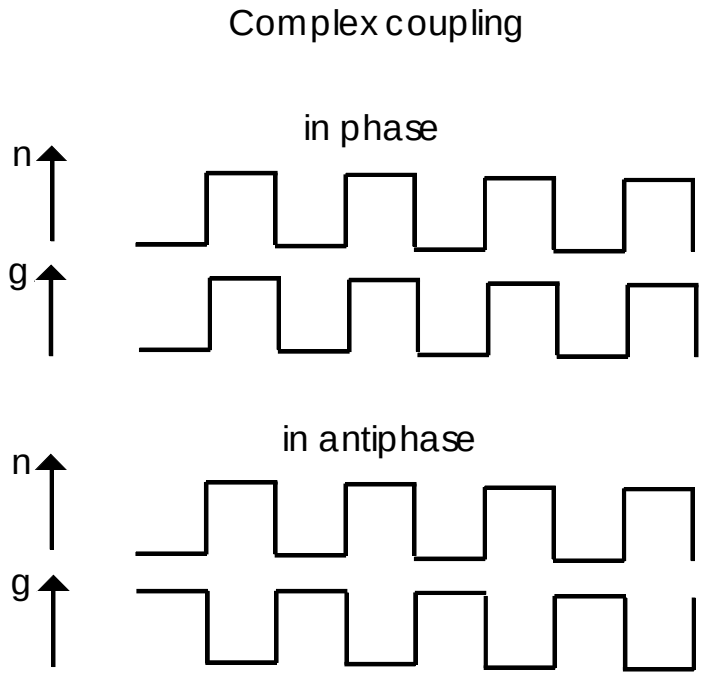

Fig. 2.2.9 Complex coupling regime: refractive index and gain could be modulated in-phase or in antiphase.

In case of the complex coupling regime, in which both the refractive index and the gain are modulated, the emission spectra is again a single mode one, but the lasing wavelength position depends on how the index and gain are modulated – in-phase or in antiphase (see figure 2.2.9). In the case of an in-phase coupling, from the two modes of the pure index coupled DFB, it is selected the longer-wavelength one. This is happening because the threshold curve of a pure index coupled DFB laser is

distorted, resulting in a lowering of the threshold for modes on the long wavelength side of the Bragg wavelength. Correspondently, in the antiphase coupling case, the selected lasing mode is on the short wavelength side of the Bragg wavelength [Carrol98, Schreiner02].

3. Process development

3.1 Basic aspects of processing nitrides laser diodes grown on SiC

To process a nitride laser diode grown on SiC, even if it's easier than in case of using sapphire as substrate due to the vertical structure of the diode (fig 3.1), still possesses a lot of challenges. On the epitaxially grown wafer it is necessary to apply a process that should contain few important steps like: the Mg activation for obtaining conductive p-type layers (as mentioned already the as-grown p-GaN is a semi-isolator due to the formation of the Mg-H complex), the realization by photolithography and etching of the ridge stripe, deposition of the isolator layer, usually SiO_2, evaporation and proper annealing of the electrical contacts (n-contact on SiC and p-contact on GaN), and realization of the mirrors by cleavage.

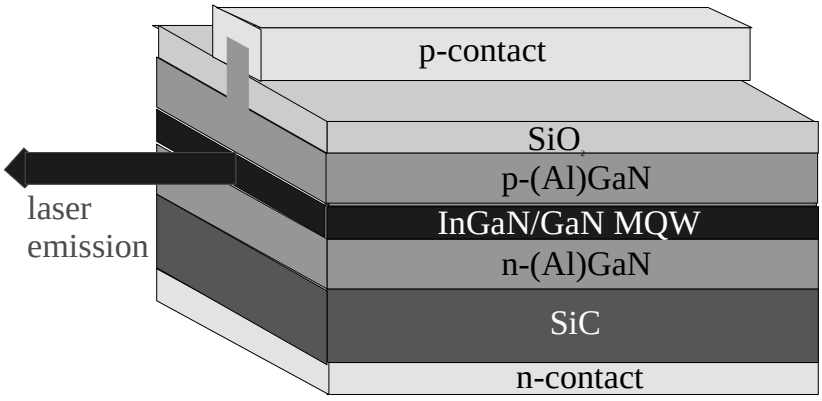

Fig. 3.1 Schematic view of a nitride laser diode structure grown on SiC.

Even if many of these steps are common to any laser diode processing, almost each of them presents particularities specific to special properties of the nitrides. For example, due to the chemical inertness of the nitrides, the etching of the ridge couldn't be done by any wet chemical procedure, so the only option is to use a dry etching method. Also the cleavage step to

realize the mirrors is not at all a trivial one. This is due to the hardness of both nitrides and SiC. Moreover, due to hexagonal crystalline structure, a preliminary wafer orientation is additionally needed for identification of the correct direction (the ridge has to be realized perpendicular on the cleavage direction) and also a thinning of the substrate. But maybe the most challenging step is the realization of the electrical contacts. This is the case especially for the p-type contact, due to difficulties to obtain a heavily p-doped GaN and the absence of metals having a work function larger than that of p-GaN.
And, at last but not the least, is necessary to integrate all this steps into an as simple and reproducible as possible sequential process - because of course all of them has to be realized on the same wafer.
At the beginning of this work it was tried such a process based on the literature data and on the previous experience existing "in house" (4. Phys. Inst., Uni Stuttgart), consisting in following steps:
- Mg activation of as grown wafer by annealing in the RTA system at 800° C for 6 minutes
- thinning the wafer to a thickness of 70-100 µm to carry out the mirror cleavage step
- evaporation of the Ni on SiC as n-contact and annealing at 900° C for 30 seconds
- fabrication of the ridge stripe by photolithography and etching
- deposition of the SiO_2 isolator layer
- evaporation of the Ni/Au p-contact on top of the ridge and annealing at 400°C for 5 minutes
- cleavage of the laser bars

This "initial process" was taking into account that the n-contact, necessitating a higher annealing temperature, has to be realized before the p-one. At the same time, was trying to minimize the exposure of the sample to high temperatures, in order to avoid the possible loss of the nitrogen due to thermal dissociation of the GaN. The nitrogen vacancies act like donors and therefore compensate the p-doping. Furthermore a minimization of the thermal budget after growth was intended to avoid the eventual In segregation (InGaN being growth at lower temperatures).

Anyway, the laser diodes processed in this way were showing very high voltage drops, and also strong degradation of the p-contact. Additionally there were adherence problems of the contacts. Therefore it was obvious necessary to improve the electrical contacts, especially the p-one, and generally to decrease the overall voltage drop on the device.
In order to realize this additional investigations regarding Mg activation, contact metalization and annealing procedure were needed. Typically, such investigations are done employing Hall effect measurements (for obtaining information on carriers concentration and mobility) in the case of Mg activation procedure, or measurements like TLM ones (Transmission Line Method) for evaluating the contact characteristic and finding the contact resistivity using simple test-structures p-GaN/sapphire which assures that the current is flowing through the correct layer (p-GaN one). Anyway the results obtained on such simple test structures can not always be used directly on a real laser structure grown on SiC. This is happening, because the properties of the p-GaN are strongly dependent on the growth conditions. These greatly influence not only the Mg-doping but also the density and types of defects, some of which (dislocations for example) could play a significant role as trapping centres for hydrogen [Pearton96]. Therefore between a p-GaN layer grown in a simple structure on sapphire and one grown on SiC in a structure having also a lot of interfaces which supplementary influences the growth mode can be significant differences regarding the p-doping behaviour. More than this, the information obtained on simple test structures, for example by Hall measurements, are related mainly to the lateral conduction, while for a laser diode on SiC important is the vertical direction. Due to these reasons, it was preferred to use directly a real diode structure grown on SiC for Mg activation and p-contact investigations (fig.3.2a). As figure of merit was considered the voltage drop on the diode structure, this being finally the parameter of interest as regards the working device.

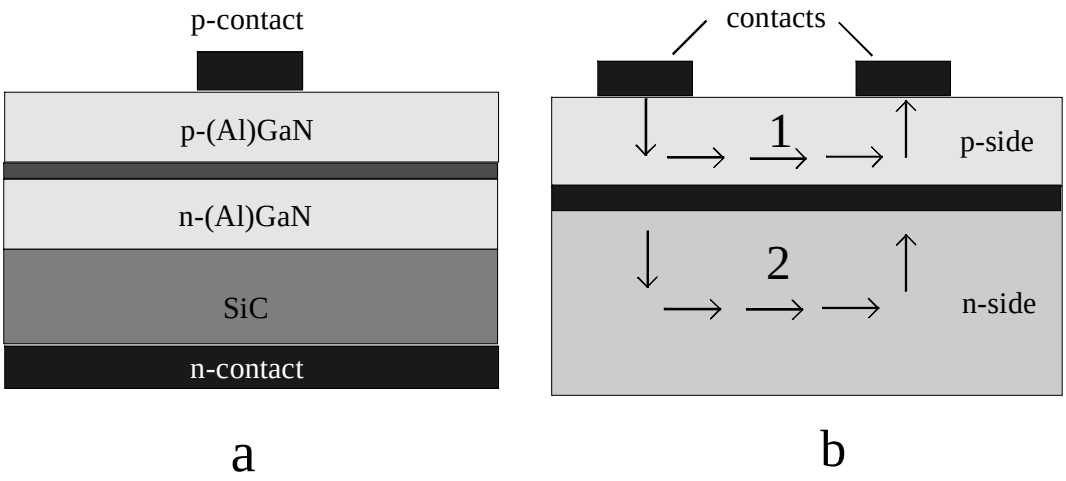

Fig. 3.2 a –Vertical diode structure used for Mg activation and p-contact investigations; b – TLM structure used for checking the contact characteristic.

Additionally, in the case of contact investigations it was also used a TLM–like structure (fig 3.2b). Even if, as mentioned, this kind of measurements require that the current flows through the contact layer (like current path 1 in fig 3.2b), which in case of applying it on a real diode structure could not be always true, it's still able to indicate the contact behaviour. That means that, even if due to high sheet resistivity of p-GaN layer combined with a relatively large reverse current through the diode, a significant part of the total current could also flow through path 2 in fig.3.2b, an eventual non-ohmic contact could still be observed from the non-linearities of I-V characteristics at low voltages (below 3V).

3.2 Realization of the n-contact

As mentioned already, one of potential advantages of using SiC as substrate is the possibility to obtain a vertical diode structure with a backside n-contact. In this case the n-contact will be realized on SiC. Being a potentially useful semiconductor for many device applications, contact technology on SiC was already studied. Many metallizations like Ni, Ni-Cr, Ni/Al, Al/Ni/Al, W, Ni/WSi/Ti/Pt, Ti, TiW, TiC, Mo, Ta, etc… have been investigated for ohmic contacts on n-SiC [Crofton97, Park98, Cole00, Marinova96]. As a result of these studies, Ni ohmic contacts have been suggested as superior candidates due to their reproducible low specific contact resistance, less than $5.0*10^{-6}$ $\Omega cm^{2,}$ and deemed the industry standard ohmic contact to n-SiC [Crofton95, Crofton97]. Generally, the mechanism responsible for obtaining of an ohmic contact is considered to be the formation of metal silicide by high temperature annealing. During the anneal cycle Ni and SiC react to form Ni_2Si. Additionally an important role seems to be played, at temperatures above 900°C, by the movement of the C away from the Ni_2Si/SiC interface [Crofton97] and also by the diffusion of Si into the Ni layer [Kurimoto02]. Anyway, even if the results and opinions of various authors could differ slightly, typically, by a short (few minutes) annealing step at 950-1000°C it's obtained an ohmic, low resistance and stable contact.
As mentioned already, to exposure the laser structure at such high temperatures could provoke an eventual nitrogen loss due to thermal dissociation of the GaN. Such a situation could be detrimental for the p-contact layer, the nitrogen vacances acting like donors and therefore compensating the p-doping. Since the realization of a good p-contact on GaN is in any way a difficult step and due to its small area is more critical for the entire device, initially it was tried to avoid altogether such an eventuality (for this reason the n-contact was annealed at 900°C for 30 seconds in the "initial process"). But, anyway, even if due to much larger area of the backside contact its resistance could be not very critical, its characteristic (ohmic or rectifying) is important. Therefore it was necessary to investigate and to conclude if and

in which conditions it's possible to use this standard metal silicide contact on SiC that needs a high temperature annealing in case of nitrides laser diodes. The alternative could mean to use a protective coating layer during high temperature step or to search for other kinds of contact mechanisms (non-silicides ones) that avoid the high temperature annealing step. Regarding such kind of contacts, few successfully attempts to get ohmic contacts were reported: using Ti, Ta or Mo they employ either a highly doped n-SiC (10^{19}-10^{20} cm^{-3}) [Petit94, Alok93] or a more complicated procedure involving thermal oxidation of SiC followed by etching of the oxide and surface passivation [Teraji97]. Both these approaches could present difficulties in using them in a laser diode processing. Therefore firstly it was tried to clarify the situation of the standard Ni contact. From one side it was searched to find out which are the minimum temperature and time of the annealing procedure necessary to obtain a Ni based ohmic contact, and on other side, which is the maximum temperature before the p-contact starts to be influenced by the p-layer degradation in the case of these laser structures.

For investigating the Ni contact behaviour different annealing temperatures (900°, 925° and 950°C) were tested. For each temperature, the contacts, consisting in 100 nm Ni evaporated by electron-beam evaporator on a CTLM (Circular Transmission Line Method) structure, were characterized by I-V measurements after different annealing times. As can be seen from figure 3.2.1, the contact annealed at 900°C behaves non-ohmic even after an annealing time of 15 minutes. After similar investigations for the other two temperatures, an ohmic contact was obtained after 3 minutes annealing at 950°C (figure 3.2.2). For the 925°C temperature, 10 minutes annealing time was still not enough for obtaining an ohmic contact. An overview of "the best" contacts obtained for each temperature is shown in figure 3.2.3. Longer times were not considered because, as mentioned before, also a minimum thermal budget was searched.

Here, presenting these results it is necessary to make a note: the main topic of this work being the laser diodes process and characterization, the I-V characteristics graphics style typical for

laser diodes was adopted (plotting the current to the abscise) and for consistency it was kept through all the work.

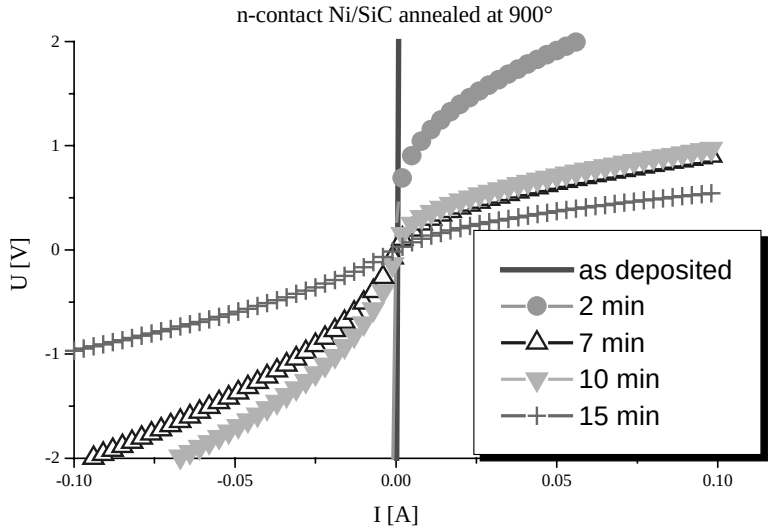

Fig. 3.2.1 I-V characteristics of Ni/SiC contact annealed at 900°C for various annealing times (CTLM structures)

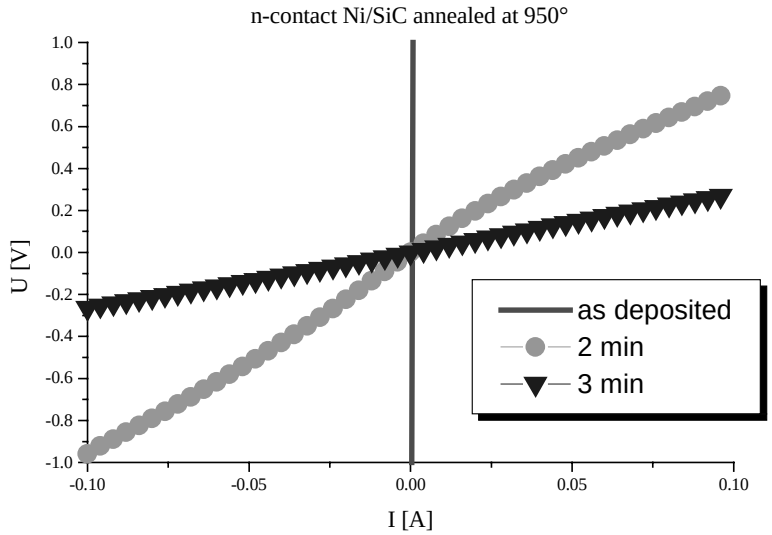

Fig. 3.2.2 I-V characteristics of Ni/SiC contact annealed at 950°C for various annealing times (CTLM structures)

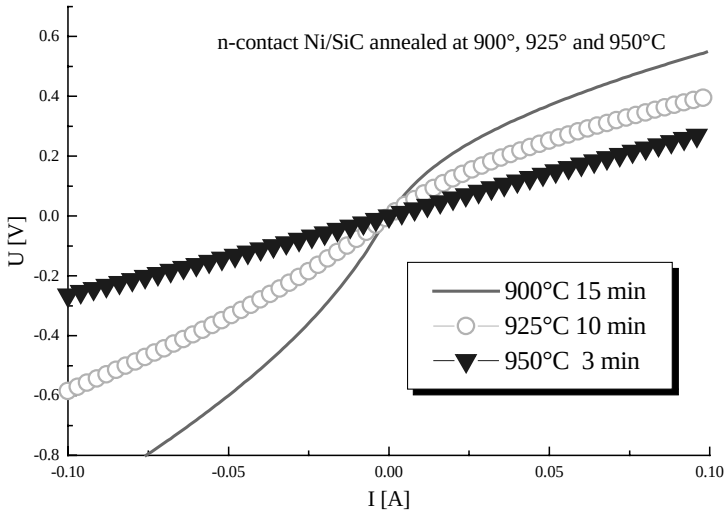

Fig. 3.2.3 I-V characteristics of Ni/SiC contact annealed at 900°C, 925°C and 950°C (CTLM structures)

Also the high temperature annealing process was investigated with respect to its possible negative influence on the p-layer and therefore on the p-contact (which is later on realized). After a series of experiments it was concluded that a clear increase of the voltage drop on the diode due to the high temperature process appears at temperatures around 980° - 990 °C (figure 3.2.4). In this experiment the p-contact (Pd/Au) evaporated after the high annealing step was left in as deposited state, without any supplementary annealing. Indeed, the mechanism responsible for the higher voltage drop of the diodes annealed at these high temperatures (~990°C) consists in a worsening of the p-contact due to surface degradation. This was verified by monitoring the voltage drop on the diode and the p-contact behaviour for pieces from one sample after annealing at 950°C and after a supplementary annealing at 990°C. In both cases, again the p-contact was deposited after the annealing steps and left as deposited. As can be seen from figure 3.2.5a,b the 990°C temperature is responsible for a worsening of the p-contact and for a clear increase of the overall voltage drop on the diode.

In conclusion, it was established that an ohmic contact on SiC using the common Ni metallization could be obtained after a short annealing step (3 minutes) at 950°C. A visible negative effect of the high temperature process (degradation of the p-contact and an overall diode voltage drop increase due to the degradation of the p-layer) could be observed for annealing temperatures of 980°C - 990°C. For lower temperatures any eventual negative effect of the annealing step due to the nitrogen loss is probably counterbalanced by the positive effect coming from improved Mg activation which will be shown in the next section.

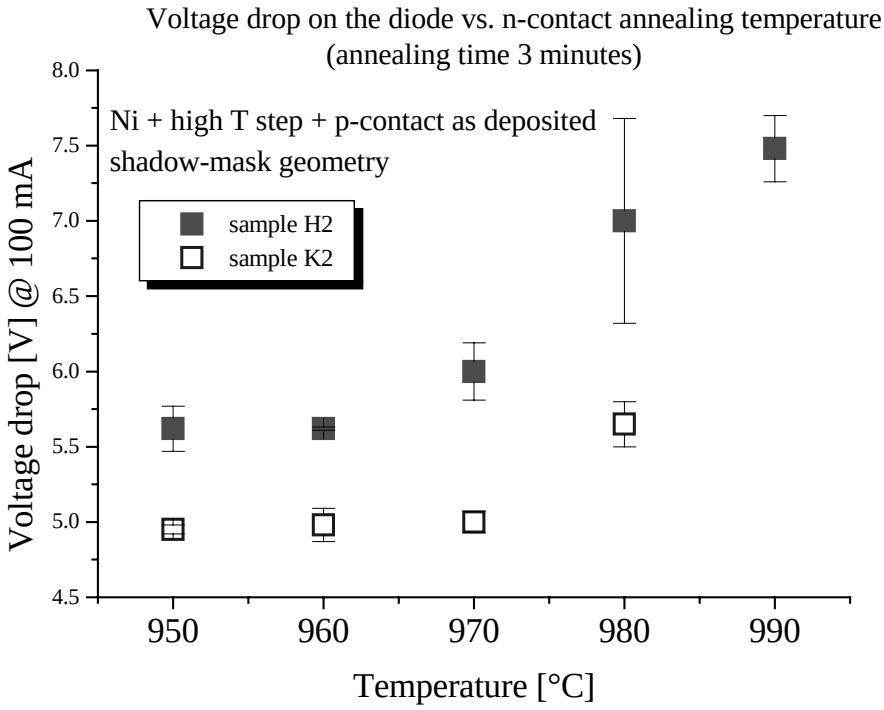

Fig. 3.2.4 Influence of the high temperature annealing on the diode voltage drop. Different epitaxial samples (here shown two) show a similar behaviour.

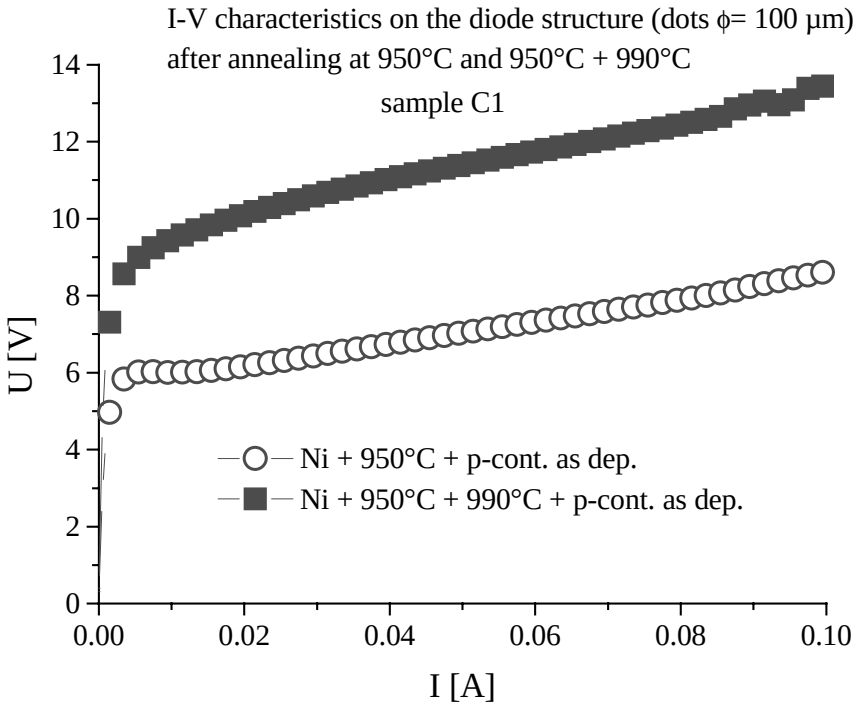

Fig.3.2.5a Influence of the 990°C annealing temperature on the diode voltage drop.

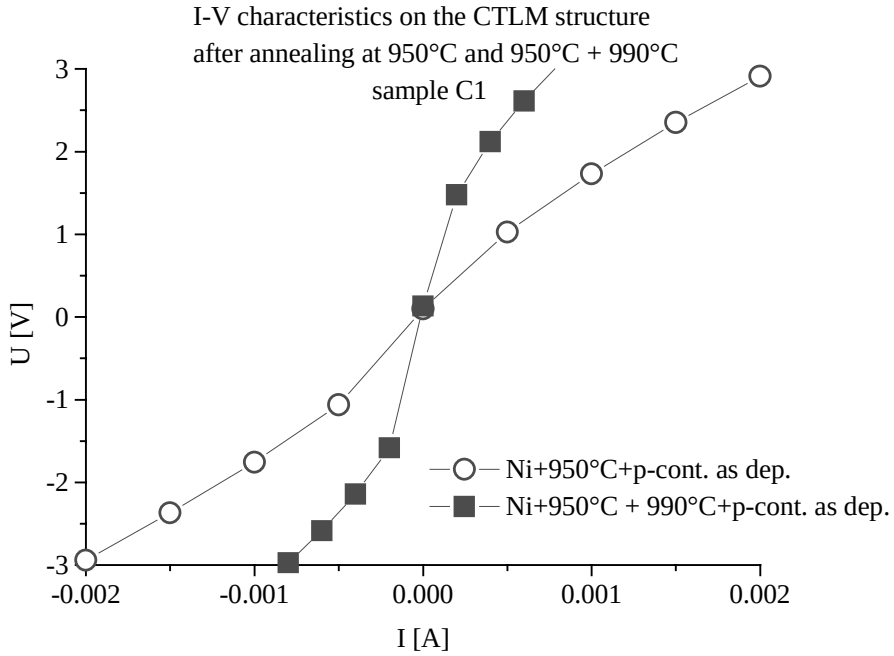

Fig.3.2.5b Influence of the 990°C annealing temperature on the p-contact behaviour.

3.3 Realization of the p-contact

One of the most difficult steps in fabrication of a nitride based laser diode is the realization of the electrical contact on p-GaN. This is due to a few critical factors like the absence of appropriate metals with a work function larger than p-GaN, residual hydrogen passivation effects that reduce the hole concentration in the material [Nakamura92, Pearton96] and difficulty in achieving high hole densities due to large ionisation energy (~170 meV) of the Mg dopants (which limits the hole concentration to values below $10^{18}cm^{-3}$ in most cases).
Therefore for realization of the p-contact it was necessary to perform investigations regarding Mg activation procedure (for obtaining p-type conductive material) as well as contact metallization technology.

3.3.1 Mg activation investigations

The first successful attempt to activate the Mg dopant and to yield the p-type conductive GaN by Amano *et al* in 1989 [Amano89] was the breakthrough which was allowing the tremendous development of the nitrides technology and devices in last years. Before that it was impossible to obtain p-type GaN and therefore any p-n junction based nitride device. Amano and his team have succeeded to achieve low-resistivity p-GaN films by applying a post-growth LEEBI (low energy electron beam irradiation) treatment on the Mg-doped GaN obtained by MOCVD. Later Nakamura *et al*. [Nakamura92] found that simple thermal annealing in an inert gas ambient of the as-grown samples can also produce p-type conductivity, which since then was becoming the standard procedure for obtaining p-type GaN. Responsible for the high-resistivity of the as-grown films was found out to be the hydrogen present in the growth environment when ammonia is used like nitrogen source. Despite the positive role in enhancing the Mg incorporation by omitting the self-compensation effect, the hydrogen remaining in the films forms stable neutral complexes with the Mg acceptors [Vechten92, Neugebauer95, Neugebauer96, Nakamura 92].

Therefore the reduction of the hydrogen passivation is the dominant process required to activate the Mg. For realizing this, behind the LEEBI treatment or thermal annealing, in last years there were investigated different methods employing microwave [Chang01], minority-carrier injection [Miyachi98], or CO_2 laser [Lai00] treatments. Anyway the common procedure and that which is generally used in device fabrication is the thermal annealing in an inert atmosphere originally proposed by Nakamura. For obtaining a stable p-GaN is necessary not only to dissociate the Mg-H complex (having a dissociation barrier of 1.5 eV as calculated by Neugebauer and Van de Walle [Neugebauer95]) and to bring the hydrogen in a metastable state where it is not passivating the Mg, but it is also important to remove the hydrogen out from the films, these being sequential processes [Miyachi98, Pearton96]. Moreover, during the activation process, hydrogen was found to redistribute to regions of highest defects (dislocations). This complicates device technology further since hydrogen is attracted to any region of strain within multilayer structures and has been shown to pile up at the heterointerfaces. In such defective regions of the structure the trapped hydrogen was present even after high temperatures annealing like 900°C [Pearton96].
For these reasons, in this work, in order to establish an Mg activation procedure that should be used during processing of these specific GaN/SiC laser structures, the approach was to realize these investigations directly on the real diodes. Taking as a figure of merit the voltage drop (from I-V measurements – figure 3.3.1) on the diodes with the same contact area, the influences of different parameters (like temperature and time) in the thermal annealing Mg activation process were investigated. The annealing was realized in nitrogen atmosphere using an RTA (rapid thermal annealing) system. In order to avoid any influences coming from supplementary annealing steps, the electrical contacts used in these experiments were Ti/Au as n-contact and Pd/Au as p-one both as deposited (evaporated after the thermal annealing for Mg activation), the contacts quality being not important here since, for one sample, the parameter of

interest was the relative change of the voltage drop versus temperature and time of Mg activation procedure.

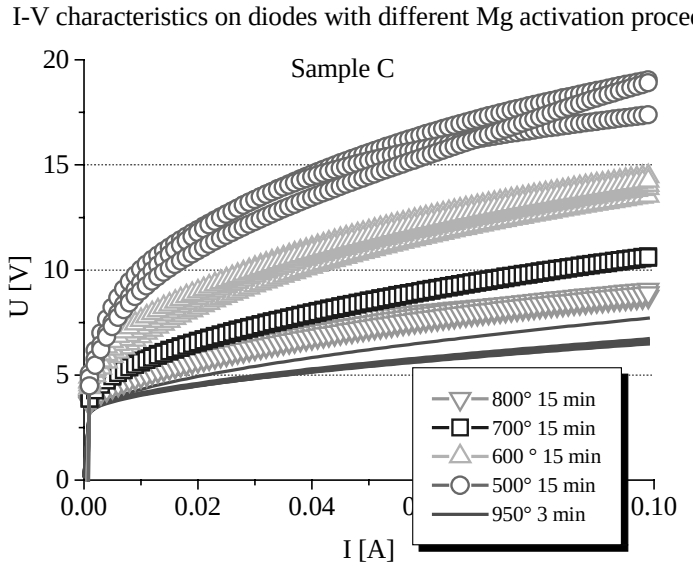

Fig. 3.3.1 Example of I-V measurements on diodes with different Mg activation procedures

After a series of experiments, the results, some of which are shown in figures 3.3.2a and 3.3.2b, were indicating that, generally, as expected for such a process, the activation time has a much weaker effect than the temperature. Moreover, a short activation process at high temperature (like 3 min at 950°C) is more efficient than a longer one at lower temperatures. This result is in concordance also with that previously found by Kuhn (who was comparing the 30 min at 750°C and the 6 min at 800°C processes) [Kuhn02]. Looking also at the behaviour of different samples (figure 3.3.2b) it was found that, especially for low temperatures, the efficiency of the activation process is strongly dependent on the sample. For high temperatures the differences between different samples are not so pronounced. Therefore while it will be difficult to establish a reproducible procedure of activation at low temperatures, at high temperatures the reproducibility from sample to sample is clearly much better. The reason for these different behaviours of samples having basically the same vertical structure is presently not very clear, but it is

related probably to some differences in doping and more probable in defect distribution, with respect of type and density of the defects. These could be due to the influences of some small changes of the growth parameters. Since after activation at high temperatures the differences between different samples are much

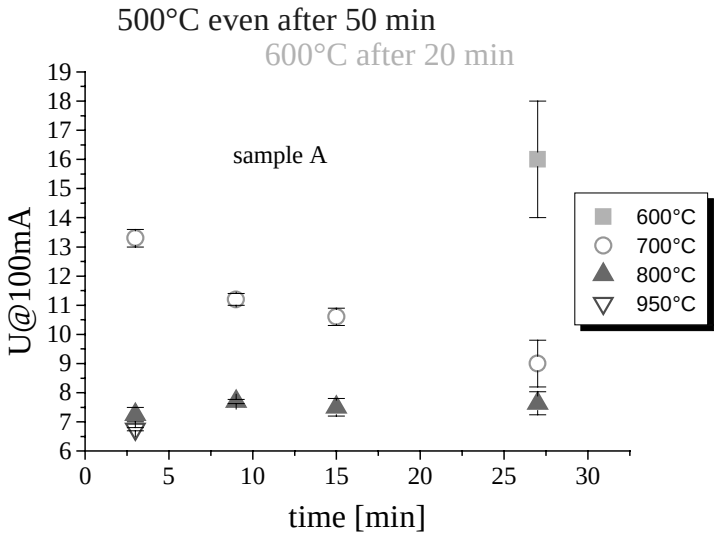

Fig. 3.3.2a Influence of the activation time on diode voltage drop for various annealing temperatures

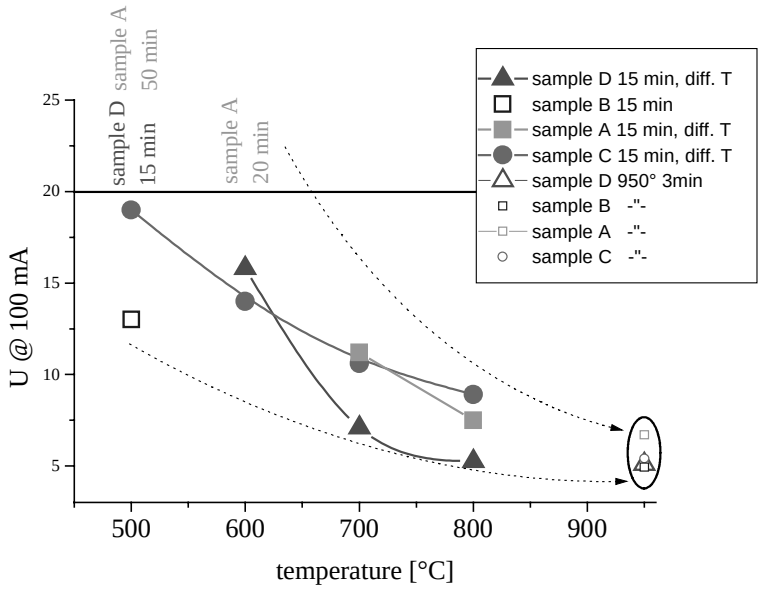

Fig. 3.3.2b Influence on the activation temperature on the diode voltage drop

smaller ones, this could be eventually correlated with the hydrogen redistribution and trapping in the defective regions found by Pearton *et. al.*[Pearton96].
Anyway, from these experiments was coming out that a short activation at high temperature (few min at 950°) is quite efficient and reproducible. At the same time, as previously found, such a high temperature step is also necessary for annealing the Ni n-contact. Therefore a good question was if it is possible to unify the two steps and therefore to skip out the "normal" preliminary activation one. For checking this, two diodes from the same wafer were processed, one with a "preliminary activation" step at 800°C followed by n-contact (Ni) deposition and annealing at 950°C, and a second one without the "preliminary activation" step at 800°C. As can be seen from figure 3.3.3, the 800°C activation step is "masked" by the subsequent higher temperature one, therefore could be eliminated altogether and simplify in this way the entire process.
It was investigated also the effect of a two-step activation process with the second step at a lower temperature. Such a method was proposed by Scherer *et al*. [Scherer01], who have obtained an improved Mg activation by a combination of a high temperature step (960°C) followed by a second lower temperature one (600°). After a series of experiments it was coming out that a second activation step at temperatures around 500° - 600°C could be helpful but it's again depending on the sample quality (figure 3.3.4) In the case of samples which generally present a relatively high voltage drop, a second lower temperature activation step is decreasing it but for better quality samples (with voltage drops already around 5V @ 100mA after the high temperature step for a p-contact geometry of 500 µm * 50 µm) the second lower temperature annealing gives no further improvement, even increase slightly the voltage drop. The exact mechanism responsible for this different behaviour was not clearly identified, but it is probably again related to the epitaxial quality of the structures (in terms of doping, defects, etc…). Anyway it was systematically found that for samples that generally present low voltage drops, a single high-temperature activation step is more efficient.

In conclusion, it was established that an efficient and reproducible Mg activation process employing a thermal annealing method can be obtained by applying a short annealing step at high temperature similar to that necessary for obtaining a Ni ohmic n-contact (3min at 950°C). At the same time it was found that the quality of the epitaxial structure has a strong influence on the efficiency of the Mg activation process. This is probably related to the complex behaviour of the hydrogen in p-GaN, which seems to be strongly influenced by the number, type and distribution of defects (which behave like trapping centres). Due to difficulties of the growing such GaN-based complicated structures and to control and properly adjust the great numbers of parameters involved in the process [Khun02, Off01] that finally affect the properties of the grown sample (in terms of doping – how much Mg but also in which way it is incorporated, the density and distribution of defects – related to Mg doping or generally present in the epitaxial structure, heterointerfaces characteristics, etc…), from device fabrication point of view it is important to establish a technological process which, for one side provides the best results for the best epitaxial samples, and on other side is reproducible as possible with respect to small variations in the samples properties.

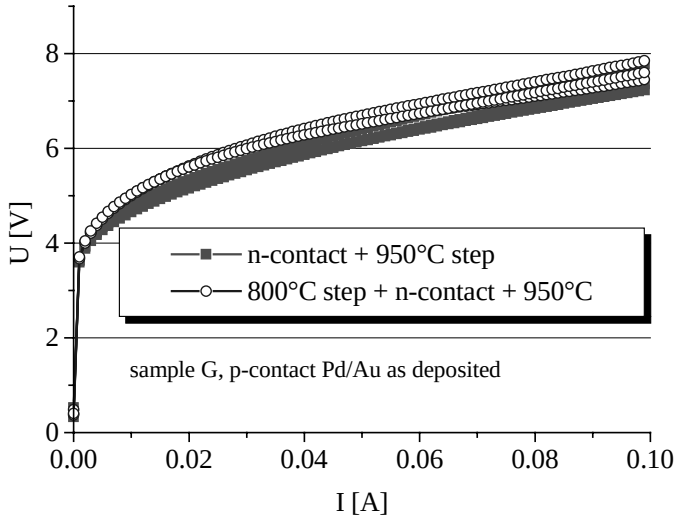

Fig. 3.3.3 Influence of the “preliminary activation” step at 800° C on the diodes I-V characteristics

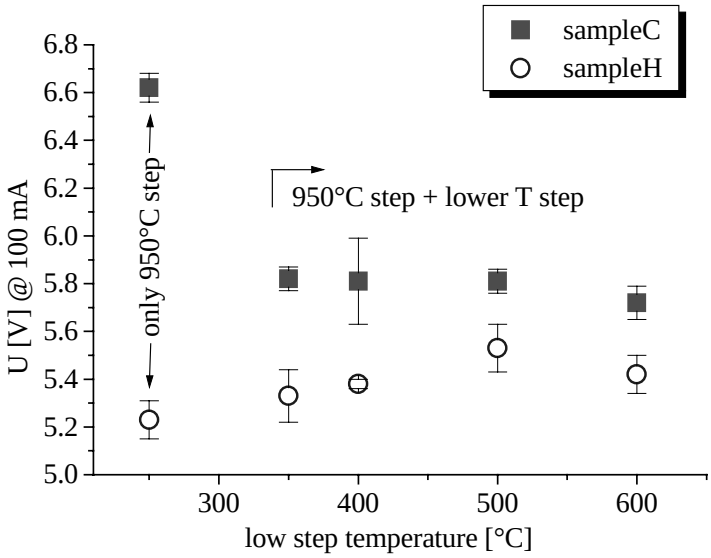

Fig. 3.3.4 The effect of the two-step (high + low temperatures) activation process on the diodes voltage drop. Like reference for every sample was taken the voltage drop on a diode processed only with the high temperature step.

3.3.2 Metallization

An ohmic contact on a p-type semiconductor could be realized either by choosing contact metals with work function greater than that of the semiconductor (figure 3.3.5), or by degenerately doping the semiconductor next to the contact region. The degenerate doping concentration of p-GaN, which was calculated theoretically, is about $3*10^{18}$ cm^{-3} but up to present the available maximum doping concentration is $1*10^{18}cm^{-3}$ and therefore a lot of efforts are being done in this area, including the use of the strain-induced piezoelectric and spontaneous polarization fields for enhancing the free hole concentration near the surface ([Gessmann02], [Li00]).

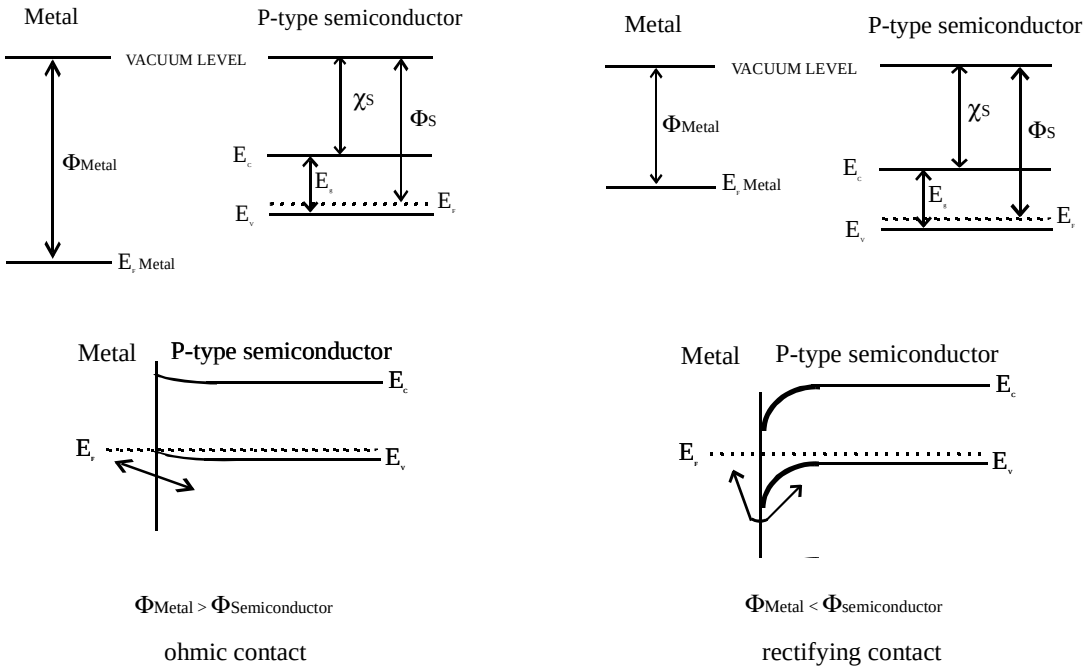

Fig. 3.3.5 Energy-band diagrams describing the Schottky theory of the metal-semiconductor (type p). Top – metal and semiconductor in separate state; bottom – after establishing the contact. Depending on the difference ΦMetal - ΦSemiconductor the established contact could be ohmic or rectifing. The terms "ohmic" refers to an interface without a barrier for the majority-carrier flow (indicated by arrows in the figure).
References: [Henisch84, Robinson85, Sze81]

Regarding the metalization choices, because the band gap of GaN is 3.4 eV, and the electron affinity is 4.1 eV, but metal work function are typically ≤ 5 eV, (see fig. 3.3.6) accordingly to the metal-semiconductor contact theory [Henisch84, Robinson85, Sze81] in the ideal case (without any surface states – the so-called "Schottky limit") at the interface p-GaN – metal it will always appears a barrier energy Φ_B whose height (in eV) is given by:

$$\Phi_B = E_g - (\Phi_M - \chi) \qquad (3.3.1)$$

where E_g is the bandgap, Φ_M is the metal work function and χ the electron affinity of the semiconductor, all expressed in eV (for n-GaN the barrier height will be simply Φ_M - χ, since for a given semiconductor and for any metal the sum of the barrier heights on n-type and p-type substrates is expected to be equal to the bandgap: $\Phi_{Bp} + \Phi_{Bn} = E_g$).

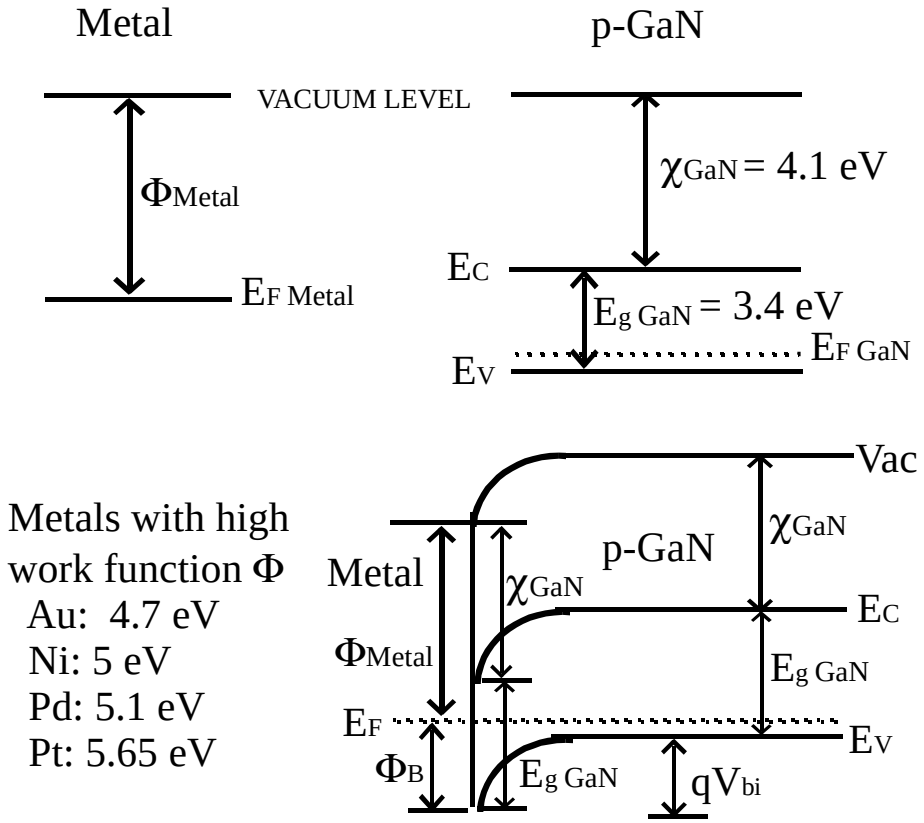

$$\Phi_M + \Phi_B = \chi + E_g \Rightarrow \Phi_B = E_g - (\Phi_M - \chi)$$

Fig. 3.3.6 Energy-band diagram of metal - p-GaN system before (top) and after establishing the contact (bottom), together with few values of metal work functions.

Here is necessary to underline that Φ_B is the barrier as seen from the metal side, and it will be independent (in this simple model) of the bias. From the semiconductor side the barrier is $qV_{bi} = \Phi_S - \Phi_M$ with V_{bi} the built-in potential at zero bias, and it will be bias dependent. Under forward bias V_F conditions (p-type semiconductor positive with respect to the metal) this barrier

reduces to $q(V_{bi} - V_F)$ while for a reverse bias V_R (metal positive with respect to p-type semiconductor) the barrier seen from semiconductor side is increased to $q(V_{bi} + V_R)$ – see fig 3.3.7.
The fact that one barrier is bias-dependent and the other one not is in fact responsible for the rectifying I-V characteristic of Schottky diodes.

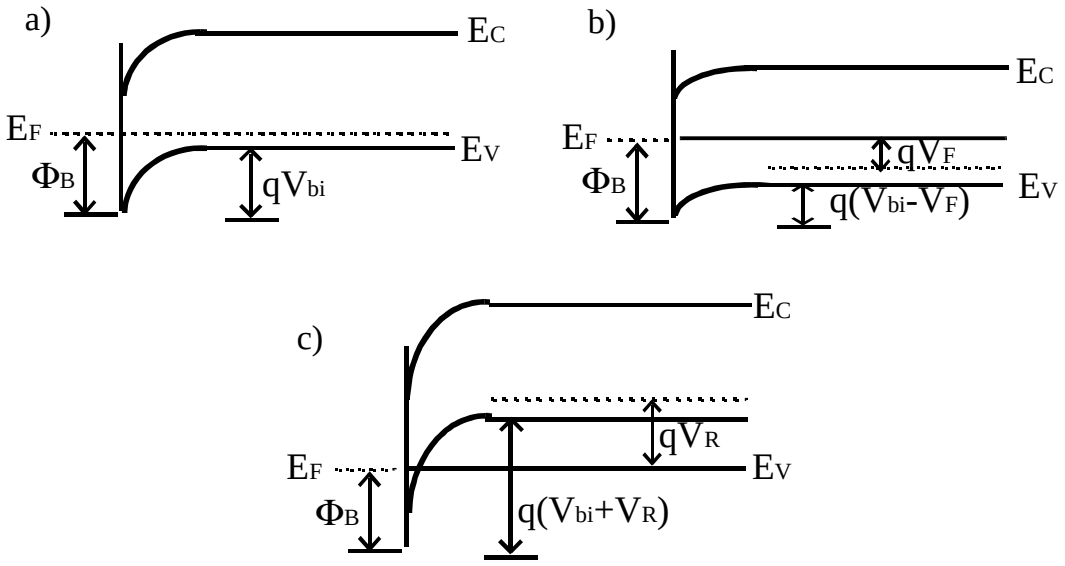

Fig. 3.3.7 Energy-band diagram of metal - p-type semiconductor under different biasing conditions: a) thermal equilibrium; b) forward bias; c) reverse bias

Regarding the possible conduction mechanism in such metal semiconductor systems, firstly it should be mentioned that the current transport is mainly due to majority carriers, in contrast to a p-n junction where the minority carriers are responsible. One of several different physical mechanisms can control the transport of the carriers depending on the semiconductor material, doping, temperature, and energy Φ_B. In thermionic emission theory the current density is given by the majority carriers having enough kinetic energies to overcome the barrier. The corresponding expression for the current density J for an applied bias V is

$$J = A^{*}T^{2}\exp\left(-\frac{\Phi_B}{kT}\right)\left[\exp\left(\frac{qV}{kT}\right)-1\right] = J_S\left[\exp\left(\frac{qV}{kT}\right)-1\right] \qquad (3.3.2)$$

where A* is the effective Richardson constant: $A^* = (4\pi q m^* k^2)/h^3$.
As can be seen, this expression correctly predicts the rectifying characteristic of the Schottky diodes: an exponentially increasing current under forward bias and an almost constant current under reverse bias that is dependent of $\Phi_{B.}$
As the concentration of the dopant in the semiconductor is increased other mechanisms for current flows across a metal-semiconductor interface become important: thermionic-field emission and field emission [Robinson85]. Increasing the doping concentration, even if the barrier height Φ_B remains essentially the same, the barrier width decreases with the square root of the doping concentration and the quantum-mechanical tunneling of carriers through the barrier can occur. At very high doping - usually the degenerate case - or at low temperatures the carriers are field emitted directly from states at the Fermi level in the semiconductor to vacant states in the metal and the field emission tunneling is the dominant conduction mechanism. At moderately high doping, the barrier is somewhat wider and only carriers with sufficient thermal energy to tunnel near the top of the barrier produce an appreciable current (thermionic-field emission). A current density – voltage relation suitable for thermionic-field emission can be expressed acoordingly to [Sharma81] and references therein like

$$J = J_S\left\{\exp\left(\frac{qV}{nkT}\right)-\exp\left[\left(n^{-1}-1\right)\frac{qV}{kT}\right]\right\}$$
$$J = J_S\exp\left(\frac{qV}{nkT}\right)\left[1-\exp\left(-\frac{qV}{kT}\right)\right] \qquad (3.3.3)$$
$$J_S = A^{*}T^{2}\exp\left(-\frac{\Phi_B}{kT}\right)$$

where n is the so-called ideality factor of the contact. When n equals unity this equation reduces to Eq. (3.3.2). According to this expression, for n>2 the Schottky contact shows higher conductivity in the reverse direction because of tunneling-dominated conduction.
Therefore, as mentioned already in the beginning of this paragraph, there are two general approaches that can be applied for obtaining an ohmic (non-rectifying contact): (i) the doping of the semiconductor, at least at the interface, to a such high doping level that extensive tunneling takes place at the contact, and/or (ii) the reduction of barrier height at the interface metal-semiconductor to such an extent that the thermally excited current over the barrier is large enough.

However, it's evident that, accordingly to the Schottky model which predict that by simply choosing a metal with the appropriate work function one could obtain a rectifying diode or an ohmic contact, on p-GaN it will not be possible to obtain by this approach an ohmic contact since there exist no metal with a high enough work function and in consequence it will always exist a large barrier Φ_B of at least 2 eV. However, the experimentally found values of the barrier height of different metals on p-GaN are significantly lower than 2 eV. In the case of Pd one finds a barrier even as low as 0.47 eV whose theoretical one should be 2.4 eV [Kim01].
This is not something specific only to GaN. For most III-V semiconductors it was also experimentally found that the value of Φ_B is in fact almost independent of the metal used to form the contact, and in consequence it's also affected by other parameters, the Schottky model being not a complete description at all of metal-semiconductors interfaces [Robinson85, Williams85]. A first possible explanation of this behavior was suggested in 1947 by Bardeen whose model proposed that if surface states existed at the metal-semiconductor interface in sufficient numbers, then Φ_B will be independent of metal (this case is the so-called Bardeen limit). Surfaces states – which, as it's known, are electronic states localized at the surface of the

semiconductor crystal being produced by the interruption of the perfect periodicity of the crystal lattice and laying energetically in the band gap – may lead to the trapping of charge on the semiconductor surface and to the existence of band bending and a space-charge layer even in the absence of a metal contact. Then, upon contact with a metal electrode the necessary charge transfer will occur to or from the surface states, if the density of surface states is sufficiently large. In this limit of a large density of surface states, the interior of the semiconductor may be screened from the metal so that Φ_B is independent of Φ_{metal} - the Fermi level is "pinned" or "stabilized" by the surface states to an energy Φ_0 above the valence band which therefore gives also the value of the barrier height in case of a p-type semiconductor.
However, it was generally found that the value of the barrier energy is somewhere between the Schottky limit and the Bardeen limit, being determined by both the metal work function and the surface states. A comprehensive model including both Schottky and Bardeen limits was done by Cowley and Sze [Cowley65] who developed a linear interface potential theory. Considering a general situation where an n-type semiconductor has acceptor-like surface states of density D_S states/cm^2/eV uniformly distributed in the semiconductor band gap and in which the metal is separated from the semiconductor by a thin insulating layer of atomic dimensions having the width δ and the relative permitivity ε_1 it was shown [Robinson85] that in this situation the energy barrier can be written as:

$$\Phi_{Bn} = \gamma(\Phi_{metal} - \chi) + (1-\gamma)(E_g - \Phi_0) \qquad (3.3.4)$$

where Φ_0 is the energy associated with a „neutral level" such that if the surface states are occupied up to Φ_0 and are empty above it then the surface is neutrally charged.
For a p-type semiconductor the above equation will be written as:

$$\Phi_{Bp} = \gamma\left[E_g - (\Phi_{metal} - \chi)\right] + (1-\gamma)\Phi_0 \qquad (3.3.5)$$

The quantity γ is given by:

$$\gamma = \varepsilon_1 \varepsilon_0 / (\varepsilon_1 \varepsilon_0 + q \delta D_S) \qquad (3.3.6)$$

where q is the electronic charge and ε_0 the permitivity of free space. It is easy to see that the condition corresponding to the Schottky limit is obtained for $D_S = 0$. On the other hand when D_s is large, γ is small and then

$$\begin{aligned} \Phi_{Bn} &\approx E_g - \Phi_0 \\ \Phi_{Bp} &\approx \Phi_0 \end{aligned} \qquad (3.3.7)$$

That means that the energy barrier is independent of Φ_{metal} and the Fermi level is pinned by the surface states, which corresponds to the Bardeen limit.
Anyway, even if this model was extremely useful in practice and was extensively applied, it was clear that it was too simple as it assumes a distribution of surface states which is highly unlikely to occur universally on all surfaces.
In reality the situation is much more complicated since one should consider also other factors like, for example, the perturbations produced by the existence of a metal or oxide layer on the semiconductor surface - by producing for example lattice defects at or near the surface which in turn produces also surface states that pin the Fermi level (therefore one should refer to the states responsible for pinning as “interface states”). Also, the energy barrier could be influenced by the chemical reaction between the metal and the semiconductor or by the interdiffusion of the elements at the interface. In addition, constituent atoms from the semiconductors may diffuse into the metal contact leaving behind an excess of another constituent or generating point defects in the semiconductor. In consequence, even if, trying to understand the complex behavior of the metal-semiconductor interface there were developed many more elaborated theories about metal/semiconductor or isolator/semiconductor interface (like chemical reaction model [Andrews75, Brillson78], the unified defect model [Spicer80], Metal Induced States Model - MIGS [Heine65, Tersoff84],

Disorder Induced Gap States – DIGS [Hasegawa86], etc…), the ability to control Φ_B prior to or during metal deposition and therefore the quality of the obtained contact it's still a challenge. This is even truer in the case of a new material like GaN, which was less studied from this point of view and therefore for which the realization of ohmic contacts based on lowering the barrier height it's still in the experimental phase, a wide variety of recipes (involving metalizations, special surface preparation, annealing procedures, etc…) and underlying contact mechanism being currently investigated and proposed.

In the search of a low-resistance ohmic contact on p-GaN a wide variety of metallizations have been investigated in the last years, such as Au, Ni, Ti, Pd, Pt, W, $WSi_{0.45}$, Ni/Au, Pt/Au, Pd/Au, Cr/Au, Au/Mg/Au, Pd/Pt/Au, Ni/Cr/Au, Ni/Pd/Au, [Ho99, Pearton99, Lee99, Chu00, Kim01 and references therein], this being a hot topic in the nitrides research area. Based on metals with high work function, these contact schemas try also to further lower the contact barrier height. For this, various approaches and contact mechanisms – from the general ones briefly mentioned above – are proposed. Among those reports the Ni/Au and Pd/Au systems showed the most promising results. Despite the reported different recipes and results an ohmic Ni/Au contact is generally obtained after annealing at 400-750°C in nitrogen or air atmosphere. The ohmic contact formation is considered to be caused by either the Ga vacancies created through formation of the interfacial compounds (gallides) during the annealing in nitrogen [Sheu99, Liu00], or by the formation of the NiO during the annealing in air [Ho99]. The Pd/Au contact system is even more interesting, showing an ohmic characteristic even before annealing [Lee99, Kim01]. Regarding the contact mechanism there are also various models proposed based on the formation of the gallides compounds, the shifting of the Fermi level position from the middle of the band-gap to near valence band by the surface treatment, Ga vacancy formation during Pd deposition [Lee99], or on the Fermi level pinning related to the epitaxial growth of the Pd on GaN which via the stress built in the Pd/p-GaN interface could provoke disorder induced gap states (DIGS)

and may pin the Fermi level near the valence band top, lowering the Schottky barrier height of the Pd/p-GaN [Kim01] (this is maybe the most plausible explanation for the development of an ohmic contact even before annealing).

In this work the realization of the p-contact from device fabrication point of view was investigated. Both Ni/Au and Pd/Au metallization schemas were tested with respect to metals ratio, annealing procedure and reproducibility of the obtained contact on the diode structures. As a figure of merit was considered the voltage drop obtained from I-V measurements on the complete devices (p-n junctions). In order to investigate also the contact characteristics, additionally there were performed I-V measurements on TLM-like structures. Typically, prior to metallization for p-contact, the samples were annealed at 950°C for 3 min in nitrogen atmosphere (in order to realize the Mg activation, as described in previous paragraphs, and to anneal the deposited n-contact in the case of the diode structures). In addition the diode structures were then cleaned with organic solvents and etched in HCl for 10 min for removing the possible native oxides followed by de-ionized water rinse. All metal layers were deposited by an electron-beam evaporation step, at base pressure lower than $1*10^{-6}$ Torr. For I-V measurements on diode structures (p-n junction) the p-contact was deposited using stainless-steel shadow masks, while for contacts characteristic investigations CTLM structures where patterned by photolithography.

After a larger series of experiments involving different metal ratios, annealing procedure, etc… it was concluded that, generally, the Pd/Au contacts are superior to Ni/Au with respect to overall voltage drop on the device, contact characteristics and reproducibility. As an example, in figure 3.3.8 a, b there are compared the results for Pd/Au (50/50 nm) and Ni/Au (50/50 nm) contact layers deposited on parts of the same wafer. Even if the Ni/Au contacts improve appreciable after annealing at temperatures around 600° C, they are still worse compared to Pd/Au (even not-annealed) regarding both the voltage drop on the

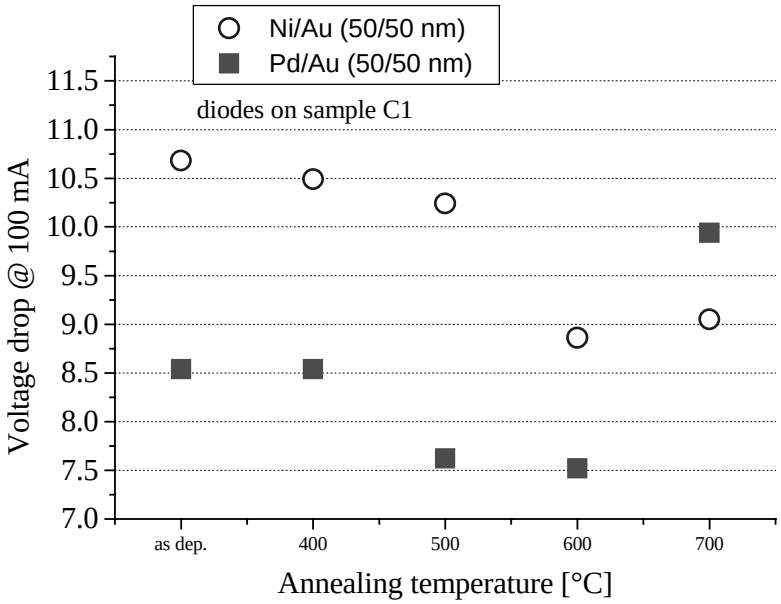

Fig. 3.3.8 a Voltage drop on diodes with Ni/Au and Pd/Au metallizations for various contact annealing temperatures.

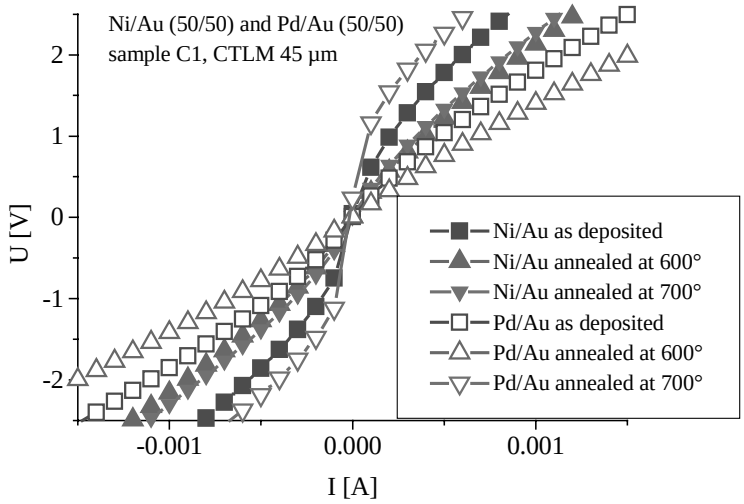

Fig. 3.3.8 b I-V measurements on TLM structures showing the characteristics of the Ni/Au and Pd/Au contacts from fig 3.3.8.a as deposited, after annealing at 600°C (the lowest voltage drop from fig 3.3.8 a) and at 700°C (degradation of the contacts).

device (fig 3.3.8 a) and contact characteristics (fig 3.3.8.b). For annealing at higher temperatures (700°C) both contacts start to degrade (the Pd-based even more dramatically) leading to an increase of the voltage drop on the device.
Before analysing in more detail the dependence of contact properties on annealing temperatures it's worth to highlight another advantage of the Pd-based contact over Ni-one. This is related to the properties of adherence and reproducibility of the contacts that are strongly dependent on the processing conditions. In a standard laser diode process the ridge is realized by etching using a photoresist mask defined by photolithography (fig. 3.3.9a).

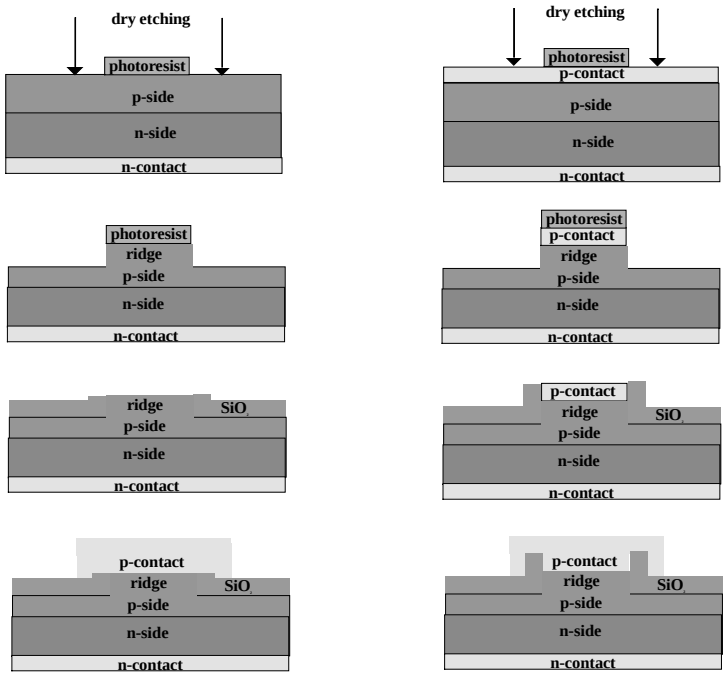

Fig. 3.3.9 a, b Shematic view of the etching and p-conatct metalization steps in a ridge-laser diode processing.

After that the isolation layer (SiO_2) is deposited, followed by lift—off for opening the window for metal contact evaporation. For realization of the good and adherent contact the status of the semiconductor surface is very important. For that approach the cleaning of the semiconductor surface prior to metallization is not

always an easy step (the photoresist has to be completely removed from the top of the µm-size ridge and this checked by visual inspection, etc…). In the case of nitride laser diode processing, the realization of a good p-contact is a challenge itself. For that, a clean and free of native oxides surface of the GaN is crucial to obtain in a reproducible manner a good contact. Therefore it will be more suitable if the surface cleaning and oxide removal procedure will be done at the beginning of the process (before the photolithographic step), followed immediately by the metal contact evaporation in order to preserve the surface. This implies that in the next process step also the metal present on the sample outside the ridge region (fig 3.3.9 b) will be etched. Using Ni based contacts this kind of approach it's not so easy to be realized due to difficulties in etching Ni layer, while Pd-based contacts are much more affordable (Pd is more easy to etch) and it was proved to obtain in a drastically improved reproducible manner adherent contact whose properties are independent of each individual process.
Taking into account the electrical results and the processing considerations it was concluded that Pd based contacts are best choice. Therefore, in order to establish the best fabrication conditions, this metalization was further investigated, especially regarding the influence of the annealing procedure on the contact properties. After a systematic evaluation of the temperature annealing effect on Pd/Au contacts deposited on more samples (for temperatures up to 600°C), the results, some of which are shown in fig. 3.3.10, indicate a rather complicated relationship. More exactly, the effect of the contact annealing temperature is strongly dependent on the sample: for that samples for which the as-deposited contact gives a relative large voltage drop (like samples C1 and C2) an annealing at 500° - 600° C is beneficial, while for the samples for which the as-deposited contact gives already a low voltage drop (like samples H1 and I) the contact annealing increases the voltage drop. This influence of the annealing temperatures is confirmed by the contact characteristics. For first category samples, with higher voltage drops, the beneficial effect of annealing can be seen also on contact characteristic that is improving (as already shown in fig

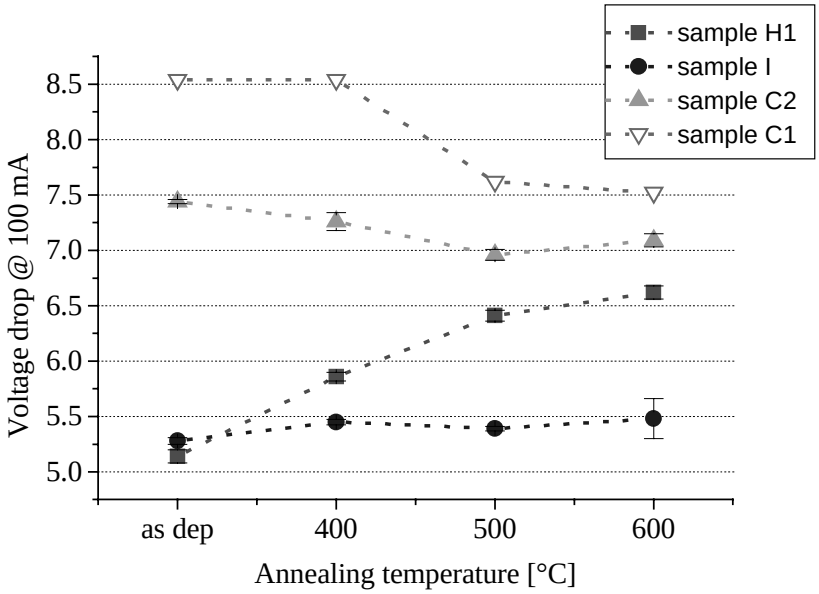

Fig. 3.3.10 Influence of the annealing Pd/Au (50/50 nm) contact on the diode voltage drop for different samples.

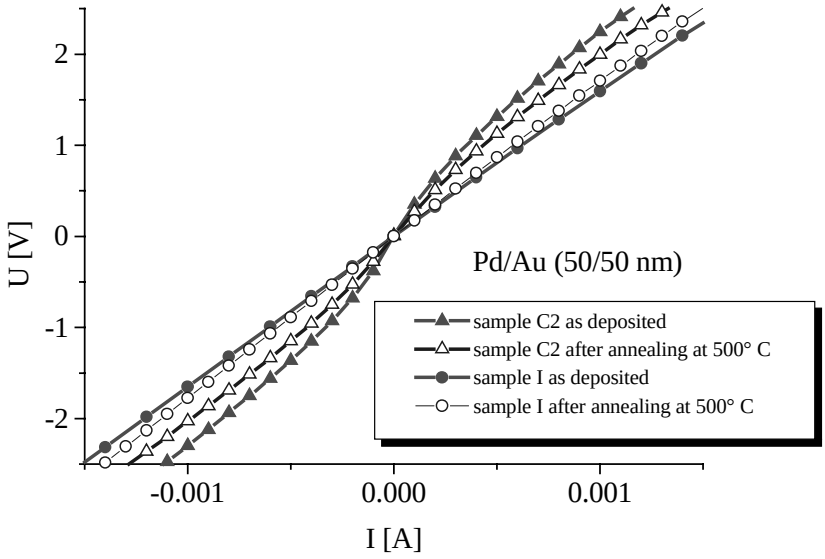

Fig. 3.3.11 I-V characteristic on CTLM structures for two samples with different behaviour of the Pd based contact versus annealing temperature

3.3.8 b for sample C1) even if it still remains a slightly non-ohmic one. The samples that present a low voltage drop with an as-deposited contact show an opposite tendency: the contact characteristic is already an ohmic one for the as-deposited metalization and starts to degrades with the annealing. A direct comparison of the these two different behaviours of the contact characteristics can be seen in fig 3.3.11 for two samples (C2 and I) which have also showed this different behaviour with regard of the voltage drop dependence on the annealing procedure in fig 3.3.10.

This apparently strange influence of the annealing on the contact properties could be to some extent understood if it's remembered that it was seen already before, when it was investigated the two-step (high + low) temperature Mg activation procedure, where the p-contact was deposited only after the low annealing step (at 500° - 600°C), being therefore always in the as-deposited state. Taking this into account it could be considered that, to a great extent, the "strange" influence of the annealing procedure on the contact properties is mainly related not to the contact itself, but to the Mg activation. For the samples with an relatively high voltage drop (for which the second lower activation step was found to be beneficial), the annealing of the contact is in fact further activating the Mg – at least to some degree, because in this case the surface of the GaN being covered with the metal, the hydrogen is probably remaining in some metastable states, not leaving the sample (but this could be the case also for the pure – without deposited contact - two-steps activation case). This, at least, could explain why, for such samples, the same effect - a decrease of the voltage drop on the device - it's observed after an second annealing step at 500°-600°C both with and without the metal contact present on the sample. In this case the observed improvement of the contact characteristic could be, at least in part, due to increased conductivity of the top layer.

Regarding the samples with a low voltage drop the things are a little bit more complicated. The fact that the annealing step at 500-600° C has again basically the same effect (an increase of the voltage drop) indifferent if the metal contact is present ("contact annealing") or not ("second step Mg activation") and that the

contact characteristics are slightly deteriorating, suggest that, indeed, the main effect of the annealing is related to Mg activation (or hydrogen redistribution) not with the contact alloying. But this will mean also that, by alloying the metal contact (Pd/Au) it's not possible to improve further the contact properties. Anyway, what is interesting and in the same time important from processing point of view, is that, for such samples that show the lowest overall voltage drop, the Pd-based contact has an ohmic characteristic in the as-deposited state. In fact these data support the findings of Kim *et.al.* [Kim01] which have observed also a degrading of the already ohmic as-deposited Pd-based contact after annealing in this range of temperatures, and who have correlated the ohmic behaviour of the as-deposited contact with the in-plane epitaxial quality of the grown Pd metal film. In this light one can speculate that these data are suggesting that the epitaxial quality of the samples is the leading parameter which influence form one side the obtaining of the Pd –based as deposited ohmic contact, and in the same time, via the eventual Mg-H-defects relationship, the activation process (the lowest voltage drop was obtained for samples which have shown as-deposited ohmic contact and in the same time for which the single short high temperature activation step was the most efficient one). But, for sure, in order to clarify these aspects and, more generally, the exact formation mechanism of contacts on nitrides much more work is necessary to be done in this field (which is currently a topic itself in the literature) implying detailed contacts studies on much simpler structures grown on sapphire, studies of the interface metals-nitrides, etc…

Anyway, not proposing in this work to realize such detailed studies, it was concluded only that using the Pd based metalization could be obtained an ohmic contact in the as-deposited state (at least for the "good quality " epitaxial structures).

4. Broad area devices realization and characterization

After having established a reliable procedure for obtaining the electrical contacts it was possible to further process and characterize complete devices.
A first approach was to realize by a simple process a fast feed-back tool to epitaxy. Taking into account the numerous parameters involved in the epitaxial process, which have to be optimised with respect to their influence on the laser diode characteristics, as well as the relatively complicated and time consuming processing of the lasers diodes, such a fast and easy tool as a quick feed-back to the epitaxy is needed. Even if the epitaxial growth is not the main subject of this work, in order to realize a device the first step is to have an as good as possible epitaxial structure. This requires from processing and device characterization point of view to contribute with an as fast and reliable possible feed-back to the epitaxy adjustments. This is especially desirable for situations in which the epitaxial growth is in its development status on the laser diode structure level but there are still necessary to be done many fine adjustments of the growing parameters. Then, in order to optimise these parameters with respect to their influence on the device properties, it's essential to enable such adjustments by the feed-back of a real device. As an example of the advantages of this approach the case of optimising the Mg doping process can be given. In this case it was found that the contact layer needs other doping conditions than the bulk layers [Scholz03]. As it it's described in this paper [Scholz03], by optimisation of the Mg-doping of GaN bulk layers according to van der Pauw Hall results it was possible to achieve, in 1µm thick layers, lowest resistivities slightly below 1Ωcm corresponding to carrier concentrations around $6 \cdot 10^{17} cm^{-3}$ and hole mobilities of about $10 cm^2/Vs$ for Mg concentrations of about $5 \cdot 10^{19} cm^{-3}$. However, in case of laser structures it was possible to reduce the contact resistivity significantly when increasing the Mg concentration in the contact layer by about

50%, although the bulk properties measured by the Hall effect already decreased.
Therefore, in order to further improve the quality of epitaxial structures it was used like a fast feed-back to the epitaxy a so-called "shadow-mask device", which in fact is a broad area electroluminiscent diode realized using shadow-masks. The advantages of this technique are that, while allowing a fast and much simpler processing than a ridge or oxide stripe laser, it still provides valuable information regarding the influence of different epitaxial parameters on the device characteristics. The process is shown schematically in fig. 4.1.1. As can be seen, is a very simple one, consisting in:
(1) realization of the n-contact on SiC by deposition of 100 nm of Ni followed by an annealing step (3 min at 950°C) which in the same time "activate" the Mg for obtaining conductive p-layers;

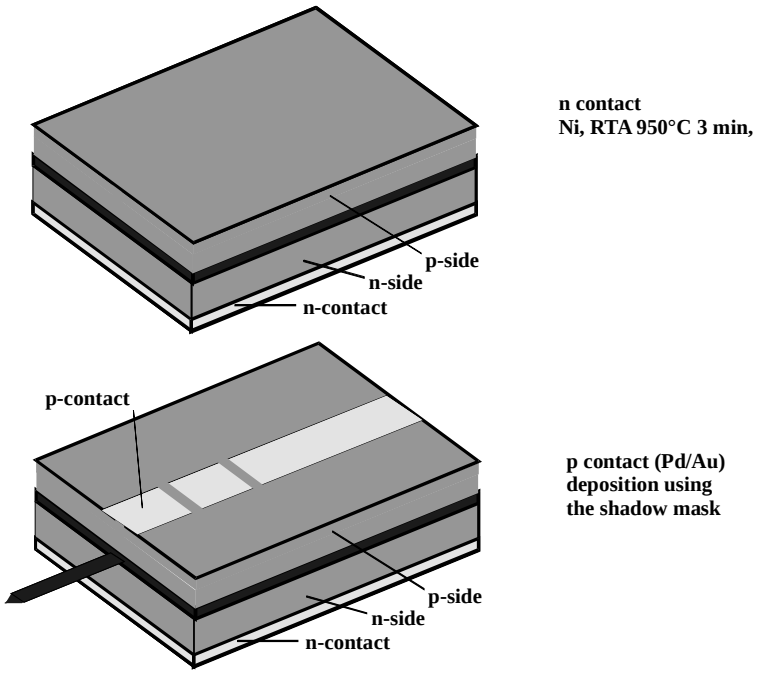

Fig. 4.1.1 Schematic view of the "shadow-mask process"

(2) oxide removal on the nitride surface by HCl treatment and evaporation of Pd/Au layers (50/50 nm) as p-contact using a shadow mask with a typical geometry of 50 x 500 μm;

(3) optionally, evaporation of a contact strengthening Au (300nm) layer also over n-contact for easier measurements and also for preventing eventual oxidation of the contact with the time;
Such a device could be used for electrical and, with some supplementary precautions taken during processing (which will be detailed later on) also optical characterizations.

4.1 Electrical characterization

Typically the shadow-mask devices were characterized from the electrical point of view by DC current-voltage (I-V) measurements up to 100 mA (~400 A/cm^2) using an HP 4145 parameter analyser. However, using only such an I-V characteristic it's difficult to extract the desired information regarding the influences of different parameters involved in epitaxy or processing. But if the I-V measurements are used comparatively, that means to look after the influence of changing one of the involved parameter on the I-V characteristics, taking for example as figure of merit the voltage drop at 100 mA, the desired information is much more easy obtained. Of course, in order to get more reliable information it is advisable to change the investigated parameter (and only that) systematically in a small series. The underlying physics involved is based on taking into account that the real laser or electroluminiscent diode is in fact a complex device including the p-n diode itself, a series resistance and eventual additional rectifying heterojunctions and metal-semiconductor contacts. Therefore, considering an overall I-V characteristics like:

$$I = I_S\left\{\exp\left[\left(V - IR_S - \Phi\right)q/kT\right] - 1\right\} \qquad (4.1.1)$$

it's coming out for a forward bias that

$$V = (kT/q)\ln(I/I_S + 1) + IR_S + \Phi \qquad (4.1.2)$$

where Rs is the overall series resistance and Φ is the eventual voltage drop on the additional rectifying junctions. For example if the p-contact presents an energy barrier Φ_B at the interface metal - p-GaN (see chapter 3), this will be included in Φ since the current through such a reversed biased contact is

$$I \sim \exp\left(-\frac{\Phi_B}{kT}\right) \qquad (4.1.3)$$

Therefore, the shadow-mask device used in this manner - taking as a figure of merit the voltage drop at the same current for identical devices except one parameter – can give us information regarding the influence of the investigated parameter on the Rs and Φ. Regarding the accuracy provided by the shadow-mask device, should be mentioned that this broad area device is not very sensitive to a change of Rs coming from p-side of the structure, but, however it is very precisely indicating any change of Φ.

In fact, some results of electrical measurements on such devices were already shown in the chapter related to process developments. There, trying to figure out the processing parameters influences, these were varied one by one, keeping all the rest constant, and using for one experiment the same epitaxy. Here, the aim being to offer a feed-back to epitaxy, the processing parameters were kept constant in order to investigate the influences of various epitaxial parameters.
By this approach it was tried to obtain a reduction of the overall voltage drop on the device. For this there were compared different cap layers for p-contact technology like GaN, GaN/AlGaN superlatices, InGaN, as well as optimised the InGaN cap layer growth with respect to the gas flows, growth temperature, etc… Furthermore other epitaxy changes related to deeper layers (looking from p-side) were investigated with respect to their effects on the overall voltage drop. An example is the n-side buffer layer. Also, maintaining a constant process and in the same time constant contact geometry, it was possible to

generally monitorize from the electrical properties point of view the different epitaxial runs.

InGaN contact layer investigations

One possibility to decrease the p-contact resistivity and to reduce in this way the total series resistance and the overall voltage drop on the laser structure may be via a reduction of the band gap of the contact layer, as it is successfully done in other material systems like InGaAs/GaAs. However, the situation is less straightforward for the nitrides, as the epitaxial growth of high quality InGaN as potential low-bandgap material is a challenge by its own. For the incorporation of substantial amounts of In, the epitaxial growth temperature has to be drastically reduced resulting in a larger defect density and thus potential p-type compensation centers. On the other hand, strain-induced piezoelectric polarization fields may even enhance the hole concentration near the surface and thus reduce the contact resistivity as reported by Gessmann et al. [Gessmann02]. Also, Kumakura et al. [Kumakura00, Kumakura01] observed a drastic improvement of the p-contact resistivity when using a thin (2-15nm) InGaN:Mg top layer, which they attribute to the large polarization-induced band bending as well as to the high hole concentration in p-InGaN.
Therefore in this work it was investigated the possibility of exchanging the GaN:Mg contact layer normally covering the laser structure by InGaN:Mg. After few experiments was coming out that, indeed, in this way a clear improvement of the contact characteristic and a significant reduction of the voltage drop on the device could be obtained. In order to optimise the InGaN contact layer a systematic investigation of the influence of different growth conditions on the contact quality was done. For this we prepared few series of experiments aimed to figure out the optimum growth temperature, TMIn flow, Cp_2Mg flow and layer thickness (detailed epitaxy process parameters can be found in [Scholz03]). As a figure of merit for the contact quality we took the voltage drop at 100 mA on the shadow-mask processed diodes.

Variation of growth temperature

The growth temperature of the InGaN contact layer directly influences the In concentration. The decrease of the In concentration in InGaN with increasing temperature can be described by an Arrhenius like relation $x(In) \sim \exp(-E_A/kT)$ with $E_A \approx 1.7eV$ [Kobayashi02]. Also, the crystalline layer quality and the Mg concentration may be a function of the growth temperature, which could not directly be evaluated in this experiment. However, after measurements of a larger series of samples for better statistics, one found a decrease of the voltage drop on the shadow-mask devices with decreasing growth temperature (fig. 4.1.2). The error bars indicate the scattering of the results for different stripes on the same sample. The reason for the larger scatter of the data at lower temperatures was not completely clear. For the lowest temperature of 770°C, In droplets formed on the sample surface under these growth conditions. Therefore, a temperature around 800°C seems to be an optimum.

Variation of TMIn flow

By reducing the TMIn flow during growth of the contact layer, the voltage drop on the device increased steadily (fig. 4.1.3). This indicates that not only the changed growth conditions (i.e. temperature, effective nitrogen partial pressure), but also indeed the In concentration itself in the layer plays a significant role for the reduced voltage drop. Due to technical limitations, we could not study larger In flows. However, the formation of In droplets on the epitaxial surface when further increasing the In/Ga ratio in the gas phase under these growth conditions would be expected. [Scholz03])

Variation of Mg flow

Of course, the Cp_2Mg flow is expected to directly influence the carrier concentration and thus the contact properties and voltage

drop on the device. Under those growth conditions, an optimum could be found for a Cp_2Mg flow of about 70 sccm (fig. 4.1.4).

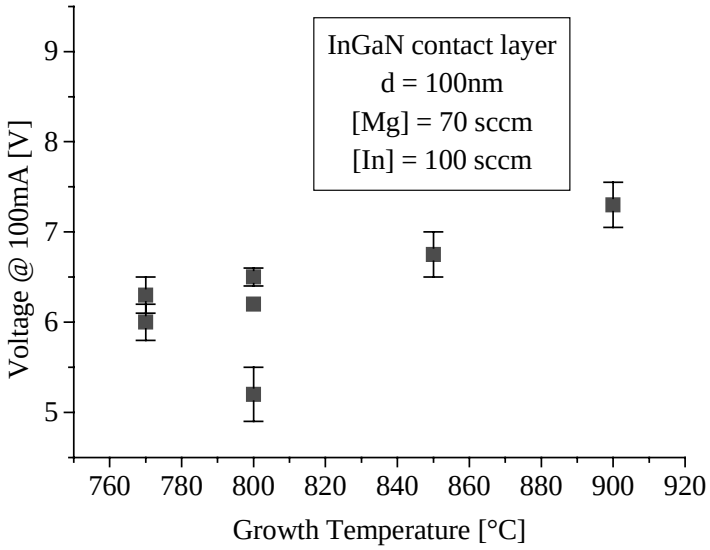

Fig. 4.1.2 Voltage drop of laser structures (shadow mask process) at 100 mA versus growth temperature of the InGaN:Mg contact layer.

Thickness of contact layer

When varying the thickness of InGaN contact layer between 50 and 150nm grown under best conditions at 800°C, it could not be observed a systematic change of the voltage drop of the laser structures.

In conclusion of these experiments was found that the best results were obtained for the InGaN:Mg contact layers grown at 800 °C with a TMIn flow of 100 sccm, a Cp_2Mg flow of 70 sccm, and a thickness about 100 nm. Such a layer showed an In content of about 2 % measured by high resolution X-ray diffraction and

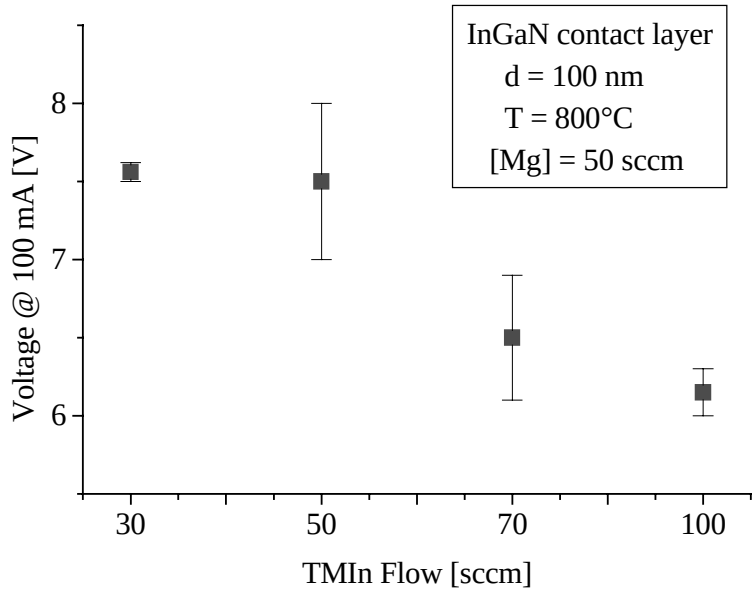

Fig. 4.1.3 Voltage drop of laser structures (shadow mask process) at 100 mA versus TMIn flow rate of the InGaN:Mg contact layer.

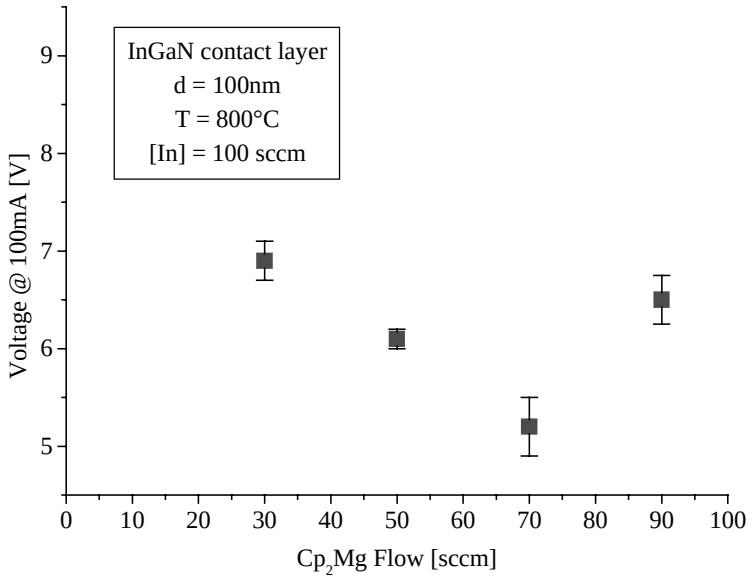

Fig. 4.1.4 Voltage drop of laser structures (shadow mask process) at 100 mA versus Cp_2Mg flow rate of the InGaN:Mg contact layer.

therefore the estimated lattice mismatch induced strain with respect to the underlying AlGaN layer was about 0.2% [Scholz03]. This could be responsible for a slightly increased hole density near the AlGaN:Mg – InGaN:Mg interface. However, it is not directly evident why this should result in a better contact. Therefore, one could speculate that by the In incorporation and the changed growth conditions, the band bending at the nitride surface is changed in such a way that the hole barrier between the metal film and the InGaN:Mg is reduced.

A direct comparison between a InGaN and a standard GaN contact layer showed a voltage drop reduction of around 2 V at 100 mA for the InGaN layer (fig. 4.1.5). Also regarding the contact I-V characteristics fig. 4.1.6 demonstrates a clear improvement of the InGaN:Mg contact layer compared to the GaN:Mg one.

On other hand this low In content of the contact layer (2%) is advantageous, because higher In contents could rise problems with respect to the waveguide properties of the laser structure due to its higher refractive index. As it was calculated for such a structure [Härle02], an In content of more than about 3%, could seriously affect the waveguiding behaviour reducing the optical confinement in the active zone of the structure. Fortunately this improved InGaN:Mg contact layer with only 2% In should not provoke such waveguiding problems.

Regarding the quality of this contact in terms of contact resisitivity, even if an exact value couldn't be obtained (as mentioned in the beginning of chapter 3, the TLM structures applied directly on these laser diodes couldn't provide reliable quantitave measurements due to the complicated current path) from the very low differential resistivities of the ridge-laser diodes provided with such contact layer - in the range of 10^{-5} Ωcm^2 as will be presented in the next chapters – could be estimated that, the contact resisitivity, only contributing partly to the diode total differential resistivity, has an even smaller value. Such data compare favourable to those found on currently best nitride lasers.

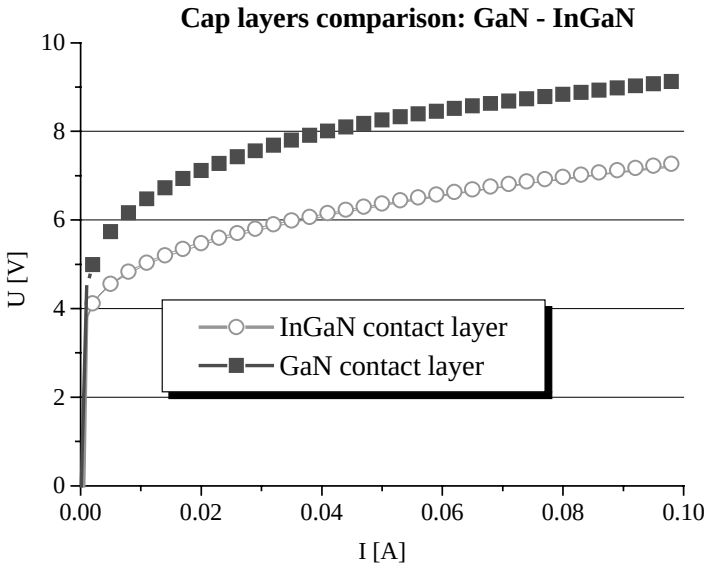

Fig. 4.1.5 I-V characteristics of two laser diodes having the same structure except the contact layers (shadow-mask processing)

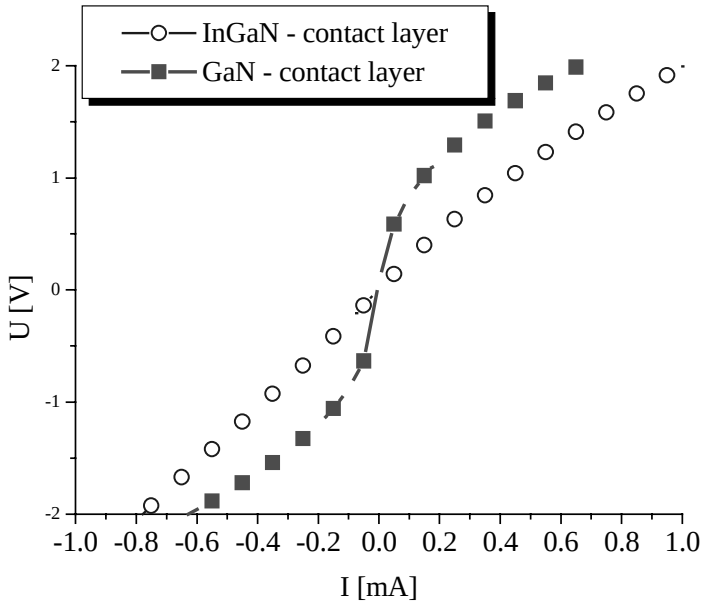

Fig. 4.1.6 Contact characteristics for Pd/Au on GaN:Mg respectively InGaN:Mg contacts layres (CTLM-5 μm structures)

Other electrical investigations with shadow-mask devices

As mentioned already in the beginning of this chapter, the main advantage of employing the shadow-mask device approach is that, due to its fast and easy processing, it makes possible the realization of a large number of experiments aimed to adjust the epitaxial process parameters. Even if, due to the large p-contact area, the attainable current densities in such device are much smaller ones than in a ridge- or oxide-stripe laser diode structure, it is still a real diode with which the effects of changing the different parameters of the epitaxial process could be seen on a real device. Because, as it was already shown, being used by doing relative measurements, this tool was proved a very effective instrument for adjusting the epitaxial process, it was employed, behind the contact layer investigations, for testing many other epitaxy adjustments with respect to their influence on the electrical properties of the device. Without describing here all these experiments (which, to some extent, are belonging more to the epitaxy development) it will be presented only one related to the buffer layer, which was showing promising results as regarding the reduction of the overall voltage drop on the diode.
The buffer layer, being the first layer grown on the substrate in the vertical structure of the diode, is an extremely important factor in the heteroepitaxial growth of the nitrides, due to the lack of substrate materials with lattice constants and thermal expansion coefficients close to those of GaN and the nitride alloys. Therefore, the development of buffer layer technology for nitrides by Amano *et al* [Amano86], who have proposed the use of a low temperature AlN buffer layer for growing GaN on sapphire, was a real breakthrough which was allowing the tremendous development of the nitrides epitaxy and device fields. The mechanism responsible for the obtaining of the high-quality GaN layers by this approach was the control of the growth mode: three-dimensional growth dominates when the GaN is grown directly on the sapphire substrate, whereas quasi-two-dimensional growth dominates when GaN is grown with the low-temperature buffer layer. The essential role of the low-

temperature buffer layer was found to be related to both the supply of high-density nucleation centers having the same orientation as the substrate and the promotion of the lateral growth of the epitaxial films due to the decrease in the interfacial free-energy between the epitaxial film and the substrate [Akasaki97]. By using this method, not only the crystalline quality, but also the luminescence and the electrical properties of the grown films have been dramatically improved. Today, the use of the low-temperature buffer layers like AlN (originally proposed by Amano in 1986) or GaN (used by Nakamura in 1991 [Nakamura91]) are indispensable and are standard for the growth of the nitrides on sapphire substrates by MOVPE.
Regarding the laser diodes grown on SiC substrate "in house" (that means in the Crystallographic Lab, 4. Phys. Inst. Uni Stuttgart) they employ an AlGaN buffer layer which was previously developed (details could be found in [Kuhn02]). However, trying to make further improvements, there were realized more investigations in this area. One interesting result was that, by inserting a thin (20 nm) undoped GaN layer, together with applying a special in-situ treatment of SiC (to be patented), it was observed a significant reduction of the voltage drop on the device [Ivanov03]. This result is shown in fig 4.1.7. Even if it is not completely elucidated the mechanism by which the insertion of an undoped layer leads to a voltage drop reduction in this vertical structure (probably this nominally undoped GaN layer has in fact a large residual donor concentration) this result is anyway a promising one. However, it remains to be investigated also other than electrical possible effects of this new buffer layer in the structure – especially related to the defects acting like non-radiative recombination centers, etc…

After having established the shadow-mask process (based on the investigations done during the processing development), it was possible to realize also a general monitorizing of epitaxial runs with respect to the electrical properties of the grown structures. As can be seen from fig. 4.1.8, it was obtained, over time, a significant reduction of the voltage drop and in the same time an improved reproducibility. More than this, such a "map" is a

useful tool not only in order to highlight the influences of the different epitaxy parameters adjustments, but also for taking into account some eventual hidden ones (not intentionally changed). For example, eventually, could be identified some influences coming from different substrate qualities by assigning a suddenly unexpected modification of the voltage drop for an entire epitaxy series with the changing of the substrate wafer, or other such effects (like maybe the "memory-effect" related to Mg [Off01]), etc…

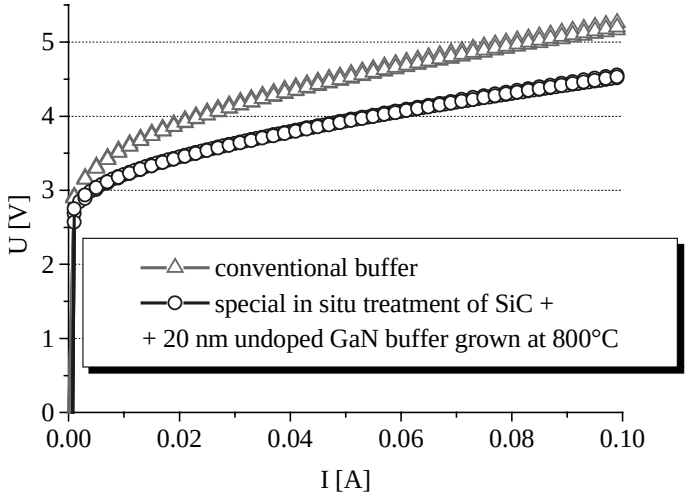

Fig. 4.1.7 I-V characteristics on diode structures with the conventional buffer (AlGaN) and the newly developed one.

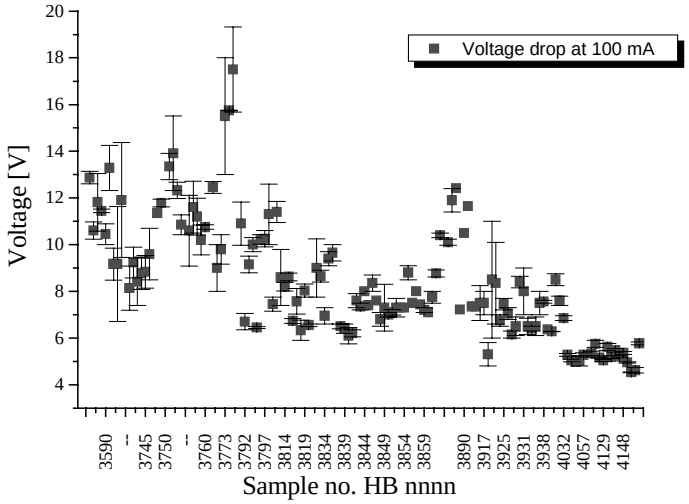

Fig. 4.1.8 Electrical characterization of epitaxial runs by the shadow-mask technique

Finally, because already since the previous chapter it was very often mentioned about the improvements obtained related to the overall voltage drop reduction, etc…, it's maybe the moment to show some results regarding the I-V characteristics on fully processed oxide-stripe laser diodes structures, even anticipating a little (the detailed processing and characterization will be presented later on). Like a summation of the improvements done by the process developments and by the epitaxy adjustments helped by the shadow-mask technique feed-back (of course the epitaxy improvements are mainly own to the "epitaxy people" from the Crystallographic Lab, but in building such a device the team-work is absolutely necessary), in fig. 4.1.9 are shown the current density – voltage characteristics of the first processed oxide-stripe laser at the beginning of this work and of some realized during the last year.

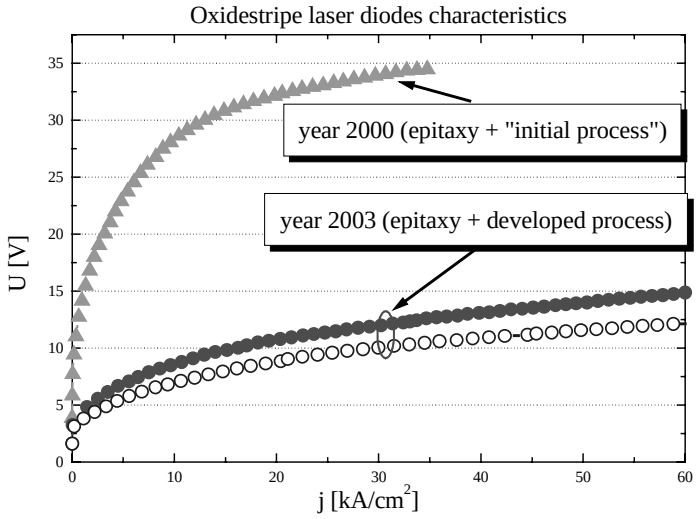

Fig 4.1.9 Current density – voltage characteristics of oxide-stripe laser diodes showing the improvements done over time (pulsed measurements 200ns/1ms)

Even if no one of them was lasing, the realized progress in reducing the voltage drop on the diode is evident. This is important not only for reducing the heating of the diode (which in case of the first processed diode was even leading to the

degradation of the contacts), but also because having achieved this relatively low voltage drop on the device, it is offering some supplementary degrees of freedom for further improvements. That means, that, having not anymore a problem related to the high voltage drop, it would be possible to test also other approaches aimed to bring improvements related to other factors important in the device functioning, which, as sidelines effects could lead to a increase of the voltage drop. As examples could be the use of another buffer layer (eventually derived from the thin GaN one) for reducing further the defects density and thus the non-radiative recombination process, or the changing of the Mg doping profile in the vicinity of the active zone for reducing the waveguide loss, etc…, some of this being possible to lead also to an increase of the voltage drop.

4.2 Optical characterizations

The shadow–mask (broad area) devices were also used in order to realize optical characterizations of the epitaxial grown structures. For realizing this, few supplementary precautions has to be taken during the processing of the device otherwise already described in previous section. In order to be possible to perform accurate optical measurements (electro-luminescence - EL - spectra) it's necessary to obtain a cleaved facet for light extraction and also to ensure that the electrical contact is positioned exactly near the facet (on the border of the sample) in order to avoid the existence of un-pumped regions that will affect the collected spectra. Therefore, in such a situation, prior to realizing the contacts, the sample has to be oriented relatively to the crystallographic directions in order to obtain the metal contact stripes perpendicular to the facet. Leaving the orientation and cleavage steps to be described in details in the laser diode's chapter, here will be mentioned only that, even using a thick substrate, the obtained facet enables the light extraction for EL measurements. In order to get contacts having precise area (length) positioned correctly near the facet and to avoid deposition of the metal also on the facet during p-contact evaporation, it's better to evaporate firstly longer metal stripes on a big area of the sample and after that to make the cleavage for obtaining the facet. Finally the segments of desired length - typically 500 μm - were obtained by cutting the metal contacts stripes. This was done by removing the contact metalization on a length of 15-30 μm using a commercial scratcher with a metallic needle as tip. Due to high lateral resistance of p-doped layers this practically ensures electrical isolation of the obtained segments but in the same time maintain the optical coupling between them (due to the hardness of the nitrides the metal tip doesn't penetrate the epitaxial layers).
In this way it was realized basically a multi-segment device which could be used for obtaining more information about the investigated samples. Besides the EL spectra, such a device could be, in principle, used also for obtaining measurements on gain and optical waveguide loss. The method for realizing these measurements using multi-segment devices, based mainly on the

commonly used variable stripe length method (VSLM) [Shaklee73, Frankowsky96, Kimura01, etc…] and which was applied for the AlGaInP system by Lewis et. al. [Lewis02] is schematically presented in fig. 4.2.1. By this approach it is in principle possibly to get the net modal gain spectra and at the same time, from the long wavelength side, the waveguide loss coefficient.

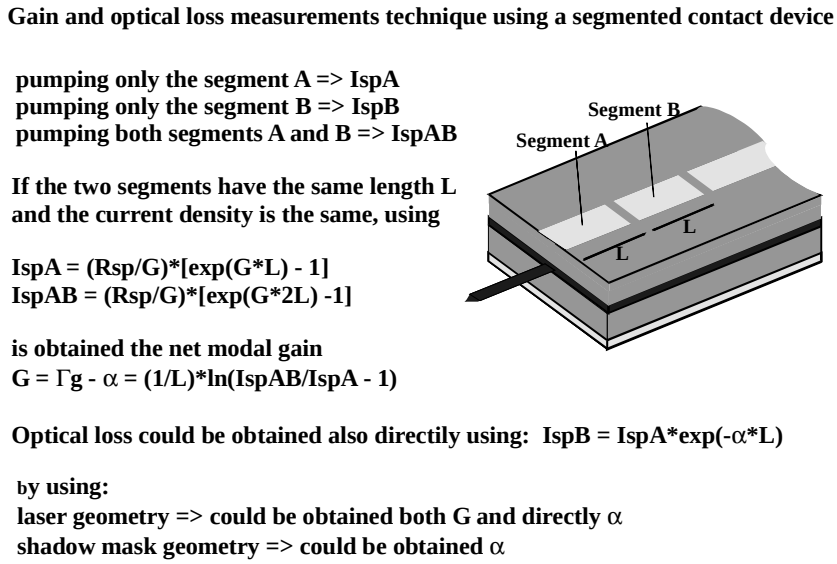

Fig. 4.2.1 The method for gain and optical loss measurements using multi-segments devices. Notations stand for: Isp – amplified spontaneous emission intensity; Rsp – spontaneous emission intensity; G – net modal gain; g – material gain; α - optical loss coefficient of the waveguide, Γ - optical confinement factor

However in the case of the shadow mask devices realized in this work on the available laser structures, due to the large area of the p-contact, the attainable current densities were too low (by comparison with that necessary for lasing in these structures) so practically the gain spectra couldn't been obtained. Therefore the shadow-mask devices were employed to get, besides the EL spectra, only directly (see fig 4.2.1) the optical waveguide losses. This approach was previously applied on nitrides also by Summers et. al. [Summers01]. For this there were used the electro-luminescence spectra collected from the front of the facet

obtained by pumping with the same current density subsequently each of the two segments. The emission from the first section (segment A) is taken as the source light, IspA The intensity IspB collected when pumping with the same current density the segment B situated at the distance L from the facet is then related to the source light by the well-known expression:

$$I_{spB} = I_{spA} \exp(-\alpha L) \qquad (4.2.1)$$

where α is the optical loss coefficient. At the long wavelength limit re-absorption of the luminescence within the un-pumped segment is avoided because of bandgap renormalization within the pumped section which red shifts the emission spectrum relative to the passive material. Thus the loss coefficient correlates directly to the waveguide loss α. In fig. 4.2.2a the EL spectra collected with an optic fibre and measured with a CCD camera using a two-segments shadow-mask device are shown.

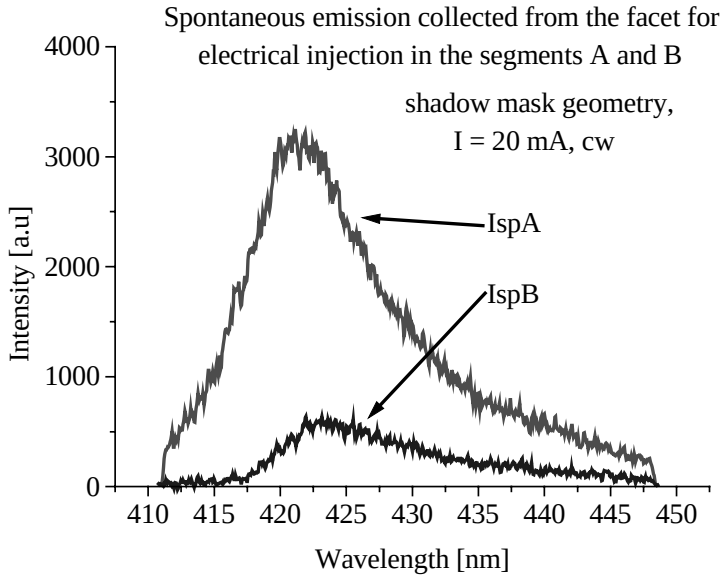

Fig. 4.2.2a Spontaneous emission spectra collected from the shadow-mask facet for electrical injection in the segments A respectively B.

The spectrum from the segment B shows a reduction in intensity due to optical loss within the un-pumped segment A, which is particularly apparent at shorter wavelengths (due to absorption within the InGaN quantum wells). The optical loss derived from these spectra is shown in fig. 4.2.2b. At longer wavelengths, beyond the absorption edge of the wells, the loss tends to a constant value of about 25 cm^{-1} in case of this sample.

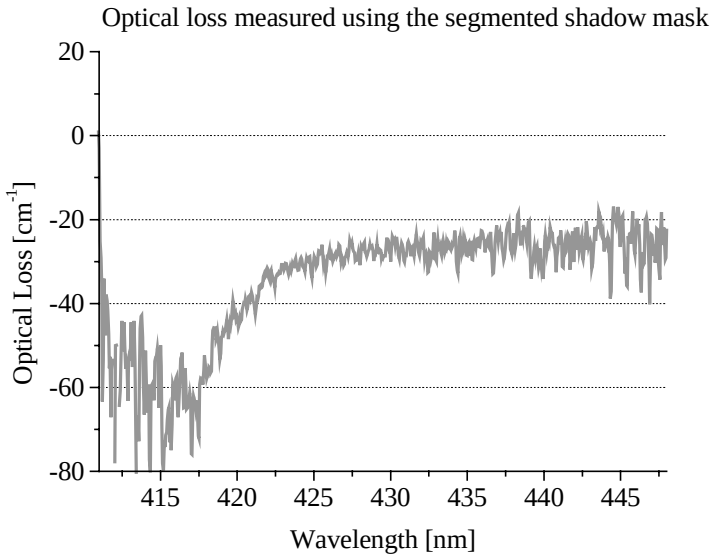

Fig. 4.2.2b Optical loss coefficient calculated using the emission spectra from fig 4.2.2a.

However, after performing such measurements on various devices it was found out that between different samples could be significant differences regarding the waveguide loss coefficient values and also the electro-luminescence spectra. In case of some samples, the EL spectrum collected at low injection currents was showing two peaks: one situated at 410-415 nm and another one at longer wavelengths, whose position was varying from sample to sample between 430-450 nm. An example of such spectrum it's displayed in fig. 4.2.3. The two peaks are situated at 412 nm (3.0 eV) and respectively 433 (2.86 eV) in the case of this sample. If the shorter wavelength peak could be assigned to the band-to-band transitions in InGaN, the longer one originates from the defects related emission centers in GaN. Such emission, from

defects related centers, situated energetically at around 2.8 eV, it's relatively known in GaN [Akasaki97]. A great contribution to these defects could be attributed to the self-compensation mechanism associated with high levels Mg-doping [Kaufmann98, Alves03].

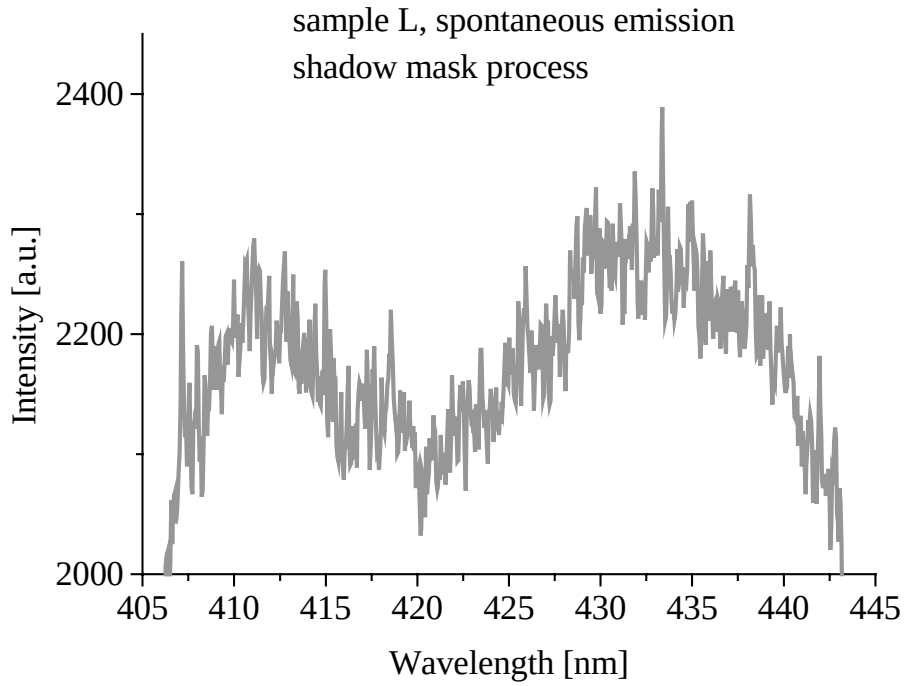

Fig. 4.2.3 EL spontaneous emissions spectrum with two peaks at low injection current.

Looking at the dependence of such a spectra on the injection current it's worth to mention that the two peaks have a different behaviour. This it's shown in figures 4.2.4 and 4.2.5 where the EL spectra at different pumping current densities are displayed. Even if the longer wavelength, broad, defected related peak is dominant at very low injection currents, it saturates at increased currents. On the other hand the band-to-band transitions peak starts to grow strongly and finally dominates the spectrum. Such behaviour could be understood if one assumes that the defects centers are present in a limited number, therefore by increasing the pumping current, at some levels, the defect-related recombination saturates and the band-to-band starts to dominate the spectrum. With this assumption, in principle, such EL spectra

on shadow- mask devices could be used for monitorize the defects quantity in different samples - by taking, for example, like a figure of merit the current density value for which the two peaks have the same intensity.

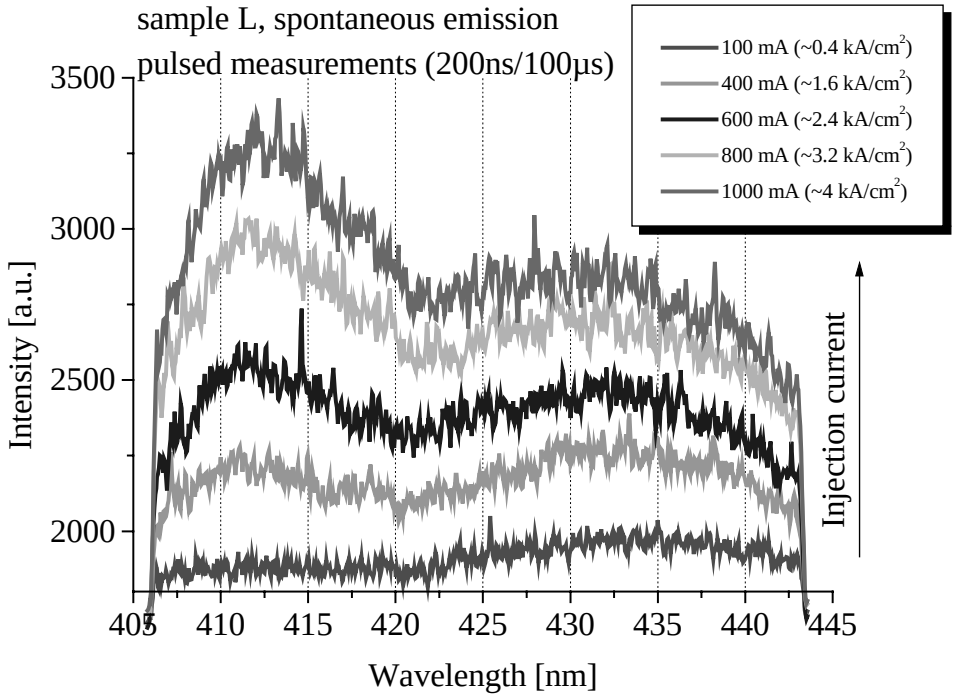

Fig. 4.2.4 EL spontaneous emissions spectrum with two peaks measured on shadow-mask device at different (lows) injection currents

The presence of the optically active defects in the sample should have an influence also on the overall waveguide absorption loss. This is particularly true in the case of the defects spatially localized close to the active region in the diode structure. This is understood if it's taken into account the optical field distribution in such a laser structure. As it was shown in chapter 2.2, the vertical distribution of the optical field in a laser structure even if it has its maximum in the quantum-well region, has also significant intensity values in the regions that are in the immediate vicinity of the active zone. Therefore, the change of the defect density in the regions close to the active zone should also have a strong influence on the waveguide absorption loss.

Because a great contribution to these defects is brought by the Mg-high doping in the p-side of the structure, a possible way to reduce the waveguide loss of the laser structure is by reducing or removing altogether the Mg-doping in the vicinity of the active zone. The latter approach was proved by Takeda et. al. [Takeda02] and by Ikeda and Uchida [Ikeda02] which were changing the position of the AlGaN:Mg electron blocking layer relative to the active zone by inserting an undoped InGaN or AlGaN layer with various thickness.

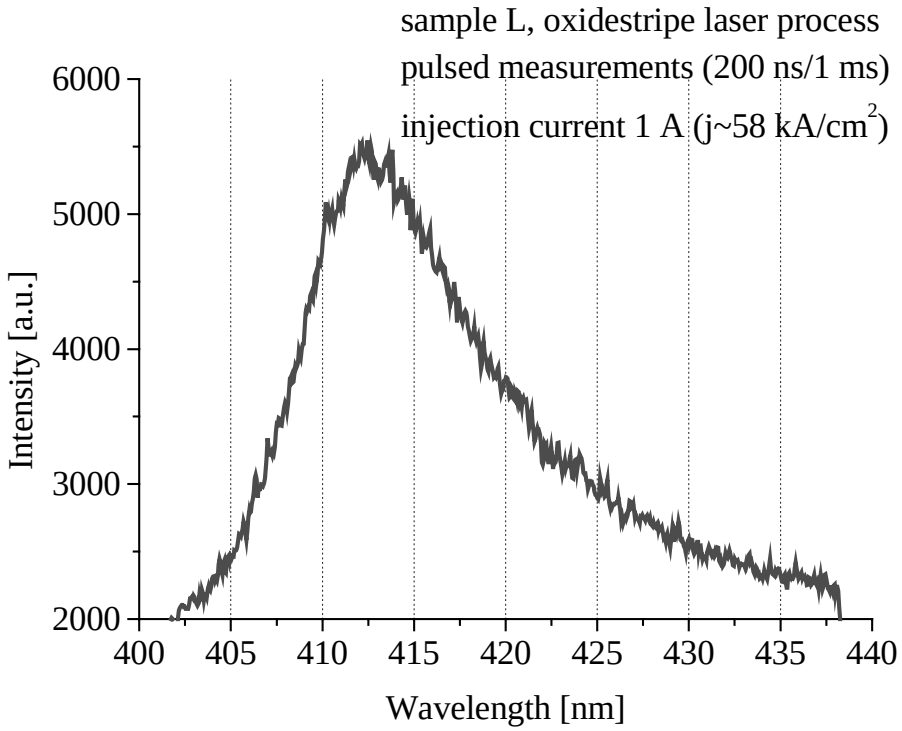

Fig.4.2.5 EL spectrum at high injection current

In this work, as a first approach, the influence of the reducing the Mg-doping level in the vicinity of the active zone was tested, without changing otherwise the vertical structure of the laser diode. For this laser diode structures with various Mg doping level in the AlGaN:Mg electron blocking were investigated. In figure 4.2.6, which shows the energy band diagram of the standard laser structure in the vicinity of the active zone, the region affected by the modified Mg-doping profile is schematically indicated as a shadowed one.

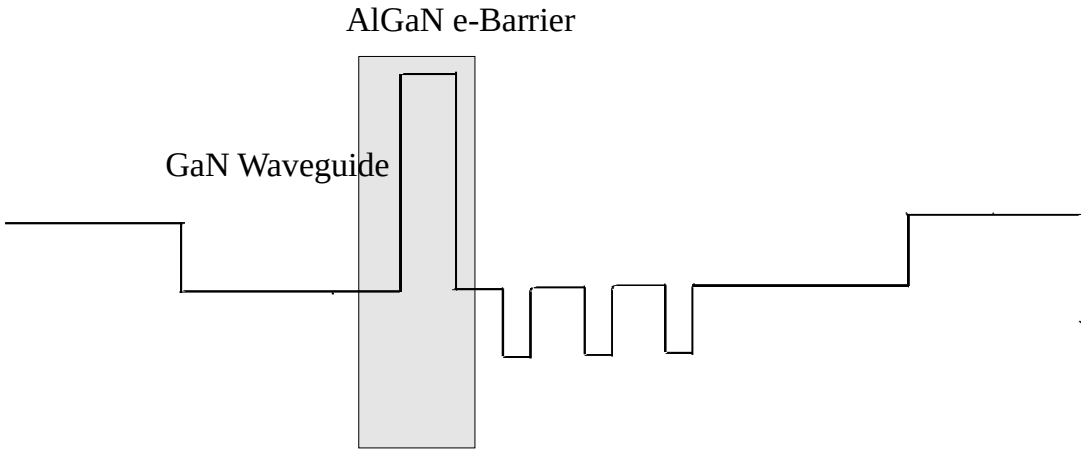

Fig. 4.2.6 Schematic energy band diagram of the laser structure (conduction band) in the vicinity of the active zone. The shadowed region is that affected by the change in Mg-doping level.

The Mg doping profile variation was realized by changing the Mg-flow during the epitaxial growth of the electron blocking layer. The effectiveness of these changes on modifying the Mg doping profile in the structure's region close to the active zone was checked by SIMS measurements. As can be seen from figures 4.2.7a, b, decreasing the Mg flow from 95 sccm to 25 sccm during growth of AlGaN:Mg electron blocking layer changes significantly the Mg doping profile near the active zone. The figure 4.2.7a shows the SIMS diagram of a laser structure grown with an Mg flow of 95 sccm, which is typical for the most of the structures grown "in house" (Crystallographic Lab, 4. Phys. Inst., Univ. Stuttgart). In figure 4.2.7b can be seen the SIMS diagram of a similar structure but with a decreased Mg flow during the growth of the electron blocking layer.
The effect of the changing Mg doping profile in the vicinity of the active zone on the electro-luminescence spectra can be seen in figure 4.2.8a. The two EL spectra were measured on shadow-mask devices at the same injection current density, high enough in order to get a clear resolved peak corresponding to the band-to-band transitions. However, at the long wavelength side of the two spectra, there are clear visible the different contributions of the defects-related peaks - appearing, at this injection current

density, as a shoulder in the long wavelength side of the main band-to-band related peak. Therefore, from the different shapes of the EL spectra corresponding to the different Mg-doping, could be estimated that, indeed, the higher Mg doping (95 sccm) is responsible for an increased defect centers density, and that an effective method for reducing them could be by decreasing the Mg doping in the region close to the active zone. The effect of this reduction of the defects near the active zone by decreasing the Mg doping in the same region on the waveguide absorption loss can be seen in figure 4.2.8b, which displays the optical loss coefficients calculated using the EL spectra from fig. 4.2.8a. It's clear visible the reduction of the waveguide loss in case of the sample grown with less (25 sccm) Mg flow in the AlGaN:Mg electron blocking layer, proving that, indeed, this approach could be an effective one for the overall improving of the laser diodes properties. However, for this, further, more detailed investigations in this direction will still be necessary.

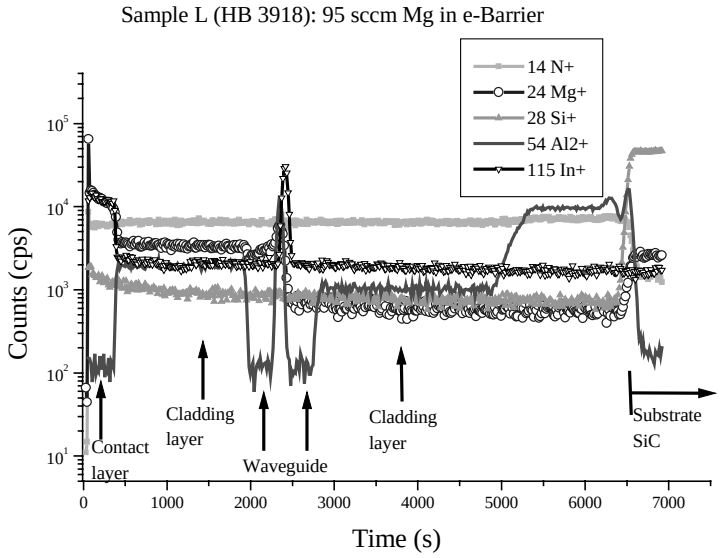

Fig. 4.2.7a SIMS diagram of a typical laser diode structure with standard (95 sccm) Mg flow doping in the AlGaN:Mg electron blocking layer (grown in Crystallographic Lab, 4. Phys. Inst., Univ. Stuttgart)

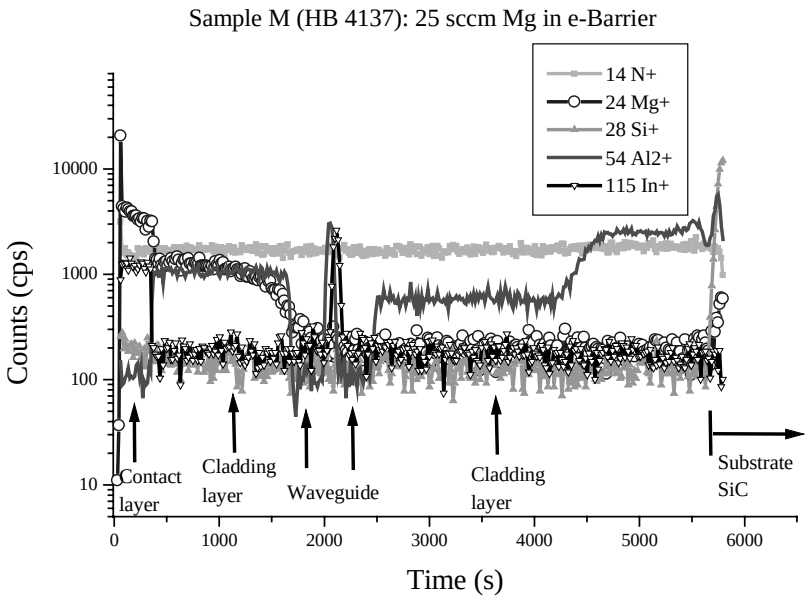

Fig. 4.2.7b SIMS diagram of a laser diode structure with modified (25 sccm Mg flow) doping of the AlGaN:Mg electron blocking layer (grown in Crystallographic Lab, 4. Phys. Inst., Univ. Stuttgart)

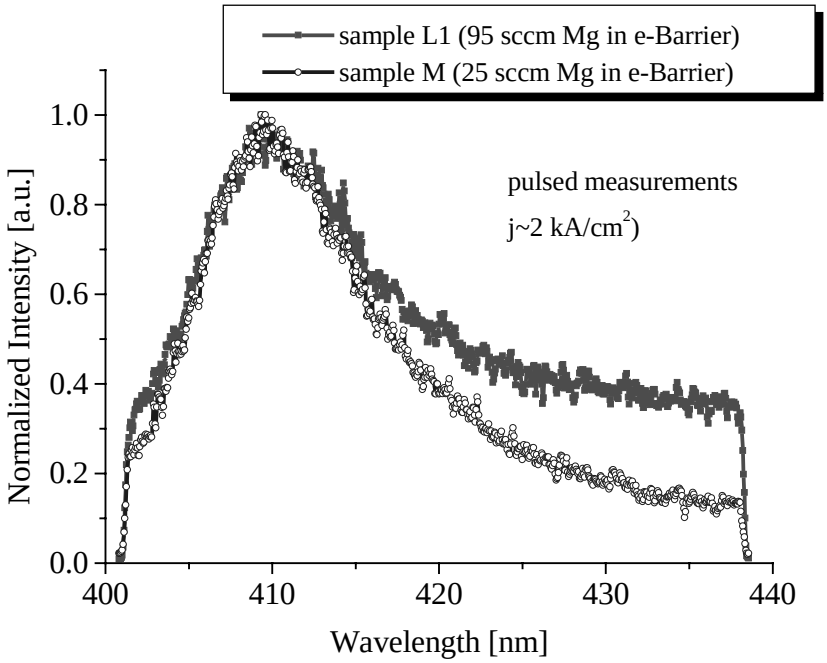

Fig. 4.2.8a The effect of changing the Mg doping in the AlGaN:Mg electron blocking layer on the EL spectra.

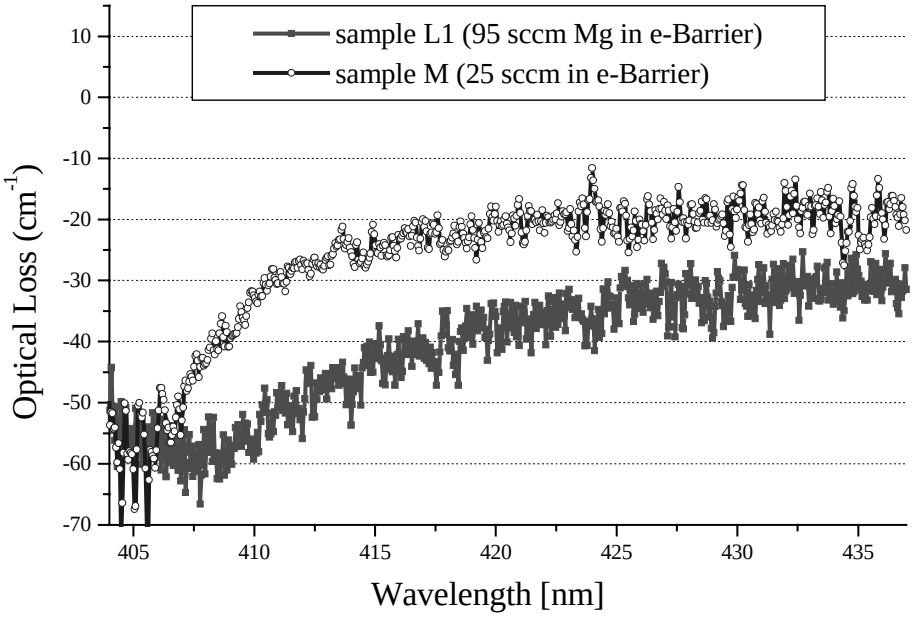

Fig. 4.2.8b The effect of changing the Mg doping in the AlGaN:Mg electron blocking layer on the .optical loss coefficient.

5. Laser diodes realization and characterization

5.1 Fabry-Perot laser diodes

5.1.1 Fabrication and characterization

In this chapter the way in which nitride based Fabry-Perot laser diodes were fabricated will be presented. Furthermore characterization measurements of this type of devices will be discussed.
As raw material both epitaxial structures grown „in house“ (Crystalographic Lab, 4. Phys. Inst., Uni Stuttgart) as well as provided by the company OSRAM Opto Semiconductors were used. Based on the developed process described in chapter 3, different types of laser diodes could be realized. A complete fabrication procedure of a ridge-waveguide diode is shown schematically in fig 5.1.1.
The first step of the process consists in substrate thinning (fig.5.1.1a). This is necessary in order to enable cavity mirror cleavage. Due to the great hardness of nitrides and of the SiC substrate it is necessary to thin initially the substrate till a thickness of around 80-100 µm. For this, the sample – a piece of around 1cm^2 that was preliminary cut from the wafer – is glued up-side down on a metallic holder and polished mechanically using pulverized SiC or diamond based emulsions. During the polishing the sample thickness is monitorized along the sample area for checking the thickness uniformity.
After the substrate thinning and cleaning of the sample, the next step is realization of the electrical contacts. For this, firstly are deposited by e-gun 100 nm Ni on the SiC as the n-contact of the structure (fig.5.1.1.b). After an annealing step – 3 min at 950 C – in a rapid thermal annealing (RTA) system, by which, as described in chapter 3, there are realized in the same time the annealing of the n-contact and the “Mg activation” procedure, the sample is basically ready for realization of the p-contact. Before this, the nitride surface being still without metallization, it is necessary to check the sample orientation, in order to identify the crystallographic directions. This is necessary because, due to the

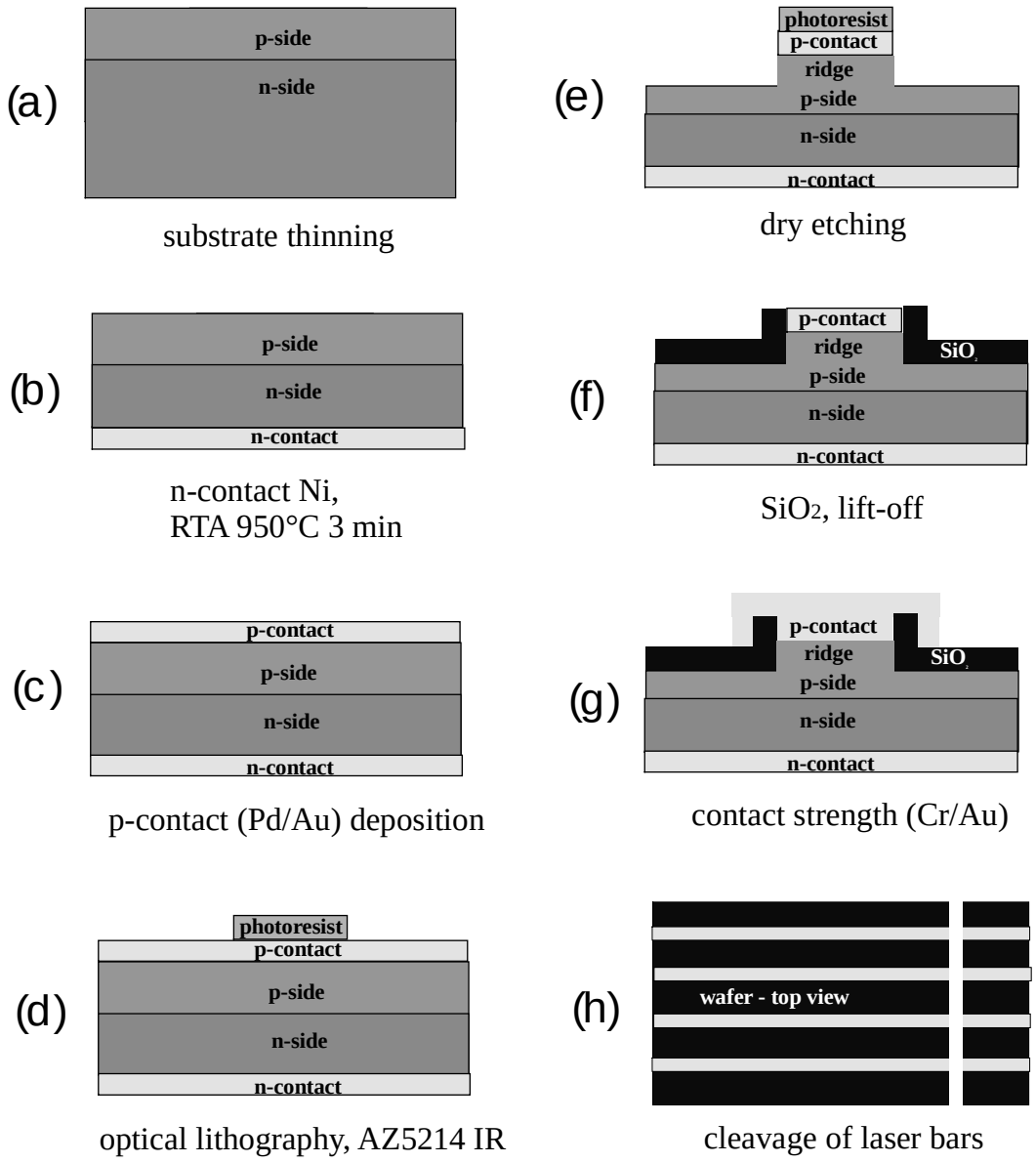

Fig.5.1.1 Schematic view of the Fabry-Perot (ridge-waveguide) laser diode processing.

hexagonal crystalline structure of the nitrides, for obtaining the laser cavity mirrors, the cleavage has to be realized parallel with the {1-100} planes and therefore the laser cavity has to be defined along [1-100] crystallographic direction. In order to find it there were employed X-ray diffraction measurements using the Laue method at the beginning of this work. However, after gaining some experience, the orientation could be more easily

detected by using only an optical microscope. For this method it was used the fact, that typically the sample surface presents a lot of defects. Among them, the so-called V-defects are appearing as hexagonal pyramids with the hexagon side perpendicular to the [1-100] crystallographic direction [Off01]. An illustration of this "orientation method" using the optical microscope is shown in fig.5.1.2.

For realization of the p-contact, after a preliminary nitride surface treatment – 10 min in HCl 37% - for oxide removal followed by H_2O rinsing, the sample it's immediately loaded in the e-gun deposition system for evaporation of the Pd/Au metallization layers (fig.5.1.1.c). In this way, by realization of the p-contact in the early stage of the process, before the photolitographic and etching steps, therefore preserving a clean and free of oxides nitride surface prior to metallization, it's greatly improved the reproducibility of obtaining high quality contacts as already presented into chapter 3.

The next step of the process consists in fabrication of the ridge waveguide using optical lithography and dry etching. For this, the photoresist AZ52/14 is spin-coated on the sample and baked at 120°C for 45s. Then, stripes 2 µm-wide are defined by optical lithography (Karl Suess MJB 3) with a positive mask. The exposed structure is post baked at 130°C for 1 min and flood-exposed for 30s to change the positive process into a negative process and then is developed (fig.5.1.1.d). The developed photoresist acts as mask for the subsequent dry etching step (fig.5.1.1.e), which is realized by

ECR-RIE (Electron Cyclotron Resonance Reactive Ion Etching) or CAIBE (Chemical Assisted Ion Beam Etching) methods. After that an amorphous isolation layer – typically about 200 nm of SiO_2 – is deposited onto the sample by sputtering or PECVD employing again the photoresist as mask (fig.5.1.1f). The lift-off process is performed to remove the rest photoresist in aceton and propanol, scrubbing also with a soft textile tip if it is necessary. Now, basically the ridge-waveguide laser structure is completely realized, with both n and p contacts. In practice it is difficult to contact with a needle the 2 µm – wide p-contact stripes. Therefore it is necessary to apply a second photolithographic step

– this time a positive process – in order to pattern larger opened stripes on which contact strengthening metal layer Cr/Au (10/500 µm) will be evaporated (fig.5.1.1g).

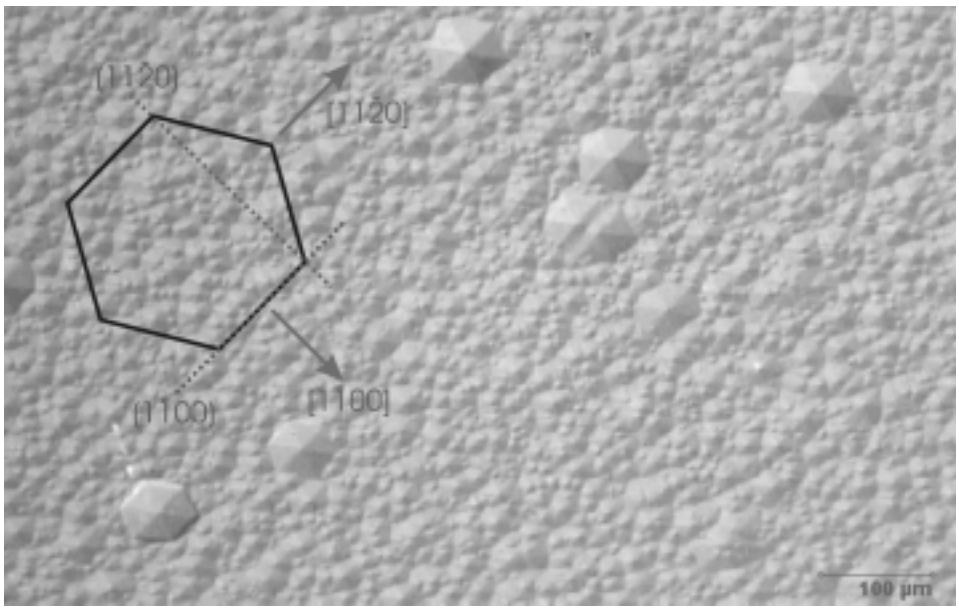

Fig. 5.1.2 Optical microscope image displaying hexagonal defects (pyramids) together with a schematic diagram of the crystallographic directions.

At the same time this large and thick contact strengthening metallization is improving the heat dissipation. The isolation layer is also important for keeping the large metal layer far away from the active zone in order to keep the optical absorption low. From this point of view – and, of course, also from the electrical isolation one - the isolation layer should be as thick as possible, but, at the same time, it is necessary to keep it removable from the top of the ridge at the lift-off process step. Therefore, as a balance between these two opposite requirements, the SiO_2 layer thickness was chosen to be around 200 nm. The thin Cr layer was used for enhancing the adherence of the contact strengthening metallization.
After lift-off process-step and metallization step, the sample is now ready for the cleavage.
Despite of the advantages of the SiC substrate, the laser cavity mirrors cleavage is itself a difficult processing step due to the

hardness and very bad cleavability of the SiC substrate. From the processed piece of sample it is necessary to cleave, parallel with the previously identified, and eventually marked, (1-100) crystallographic planes, laser bars having few hundreds μm in width, each bar containing several individual lasers oriented perpendicular on the bar (fig.5.1.1h). In order to realise this, a simple method was largely used during this work. The sample is placed up-side down on a relatively soft surface – for example a stack of few papers. Cleavage is obtained by rolling a small cylinder (can be a metal pin) on the surface (see fig 5.1.3) under gentle pressure. If the roller axis has the correct orientation, the sample will cleave easily. If this is not happening it is necessary to adjust slightly the roller orientation and to try again, without forcing, till the correct cleavage is realised. For increase the cleavage accuracy – in terms of both mirrors quality and laser cavity length – accordingly to [Hofmann00] it is advisable to scratch firstly with a diamond tip on the nitride side of the sample on a length of a few mm, deep enough in order to reach the substrate. However, in practice this was not very effectively with the available scratcher. Anyway, with or without scratching firstly the sample, a good cleavage could be realised by the method described above. The leading parameter influencing its quality is the thickness uniformity of the polished substrate.

After cleavage the obtained laser bar must be carefully taken away from the rest of the sample, avoiding metal flitters from the contacts hanging over the facet and shadowing the light emission or even shortening the laser diode.

A completely processed ridge-waveguide laser diode after the cleavage step is shown in figure 5.1.4. In the SEM image taken from the facet side, the n and p sides of the structure, the ridge geometry, as well as the isolator and p-contact strengthening layer can be identified.

Regarding this process it should be also mentioned that, by simply adjusting the etching depth one can fabricate laser diodes structures with different heights of the ridge or even without a ridge at all – in this case being obtained the so-called oxidestripe laser diode structure.

After finishing the processing, the laser diode bars are glued with two-components conductive silver mixture on a copper block serving both as heat-spreader and for easy manipulation of the devices that are now ready for measurement.

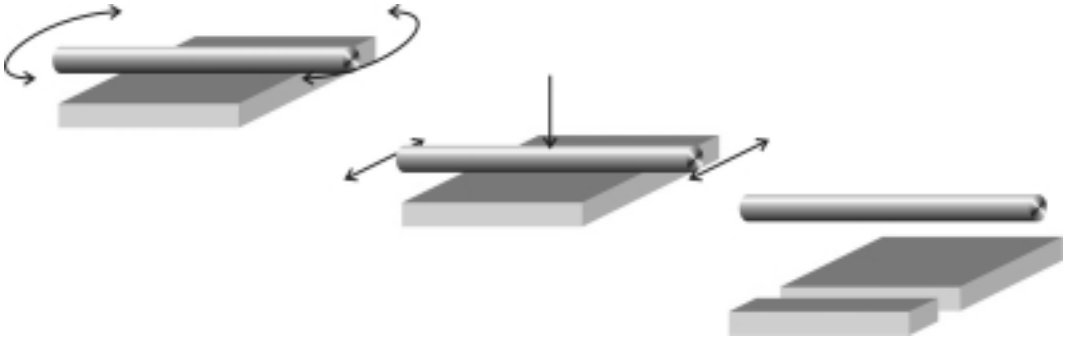

Fig. 5.1.3 Schematic illustration of the cleavage procedure

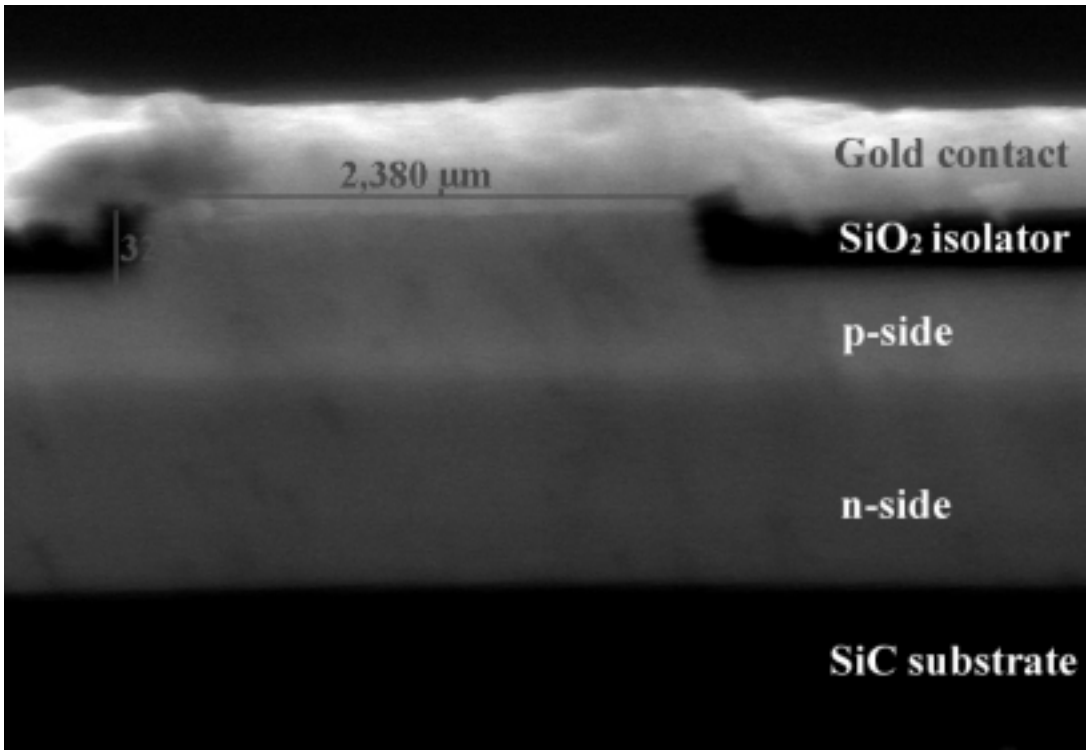

Fig. 5.1.4 SEM image of a processed ridge-waveguide laser diode. View from the laser facet side.

For characterizing the obtained laser diodes there were performed current-voltage (I-V), power-voltage (P-I) as well as electroluminiscence spectra measurements. Besides the DC current-voltage measurements using the HP 4145 parameter analyser, which allows pumping currents up to 100 mA, for attaining the higher current densities for which the available laser structures were susceptible to show laser activity, there were also realized measurements at higher injection currents, up to 2 A. In order to avoid overheating of the diode at these high injection currents, the measurements were performed in the pulsed mode, typically with a repetition frequency of 1kHz and a pulse width of 200 ns (a duty-cycle ratio of 0.02%).
The used set-up, which is shown in figure 5.1.5, contains a pulse generator (Hewlet Packard 8114A) for electrical pumping the laser diode, an oscilloscope (LeCroy LC334A) which collect via an electronic circuit the signals corresponding to the voltage drop respective current, on the laser diode, as well as on the photodiode used for optical output measurements and an computer for data acquisition and automatic control of the measurements. Emission spectra from the facet of the diode were collected with an optical fibre and measured with a CCD camera. In order to allow also measurements at various temperatures, the sample holder, on which the laser diode was mounted on the copper block (see fig. 5.1.5), is provided with a Peltier element connected with a temperature controller. This integrated measurements set-up allows a relatively easy electrical, optical and spectral characterization of the laser diodes.
Like a first step in the characterization of the processed laser diodes there were measured I-V curves in the above-described conditions. An example of the obtained I-V characteristic – expressed in current density – for one of the laser diodes realized integral “in house” (4. Phys. Inst., Uni Stuttgart) could be seen in figure 5.1.6. Even if, probably due to the large amount of defects acting like non-radiative recombination centers still present in these structures, they were not yet lasing, their electric properties are very promising for a GaN based diode. As can be seen, the voltage drop remains less than 12 V even for current densities as high as 50 kA/cm^2 and the differential resistivity has an excellent

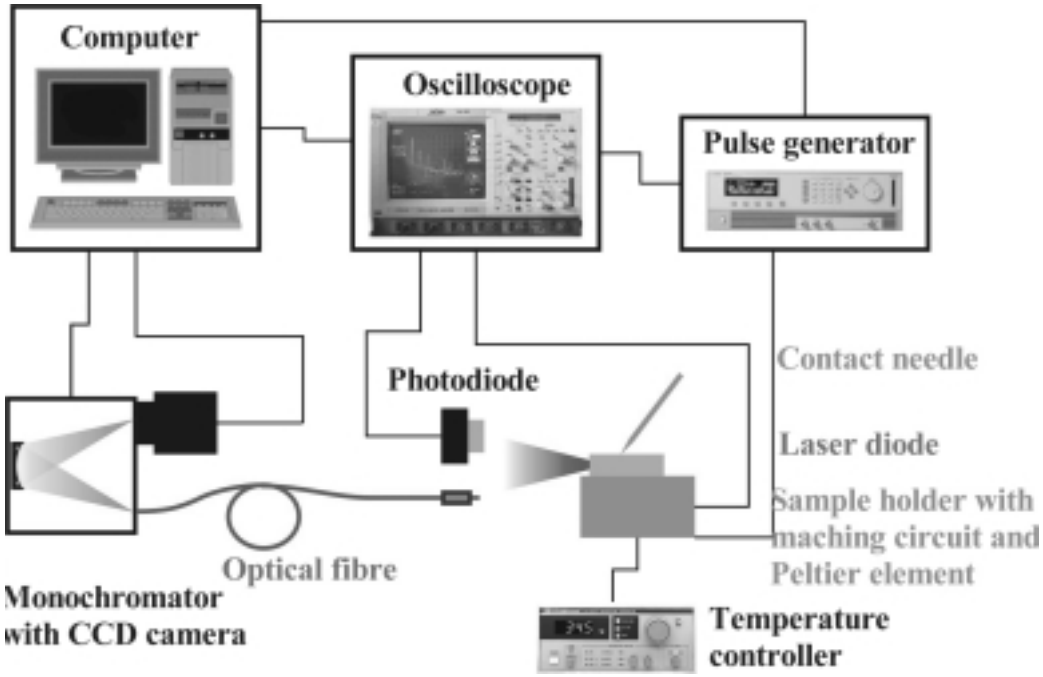

Fig. 5.1.5 The measurement set-up used for laser diodes characterization

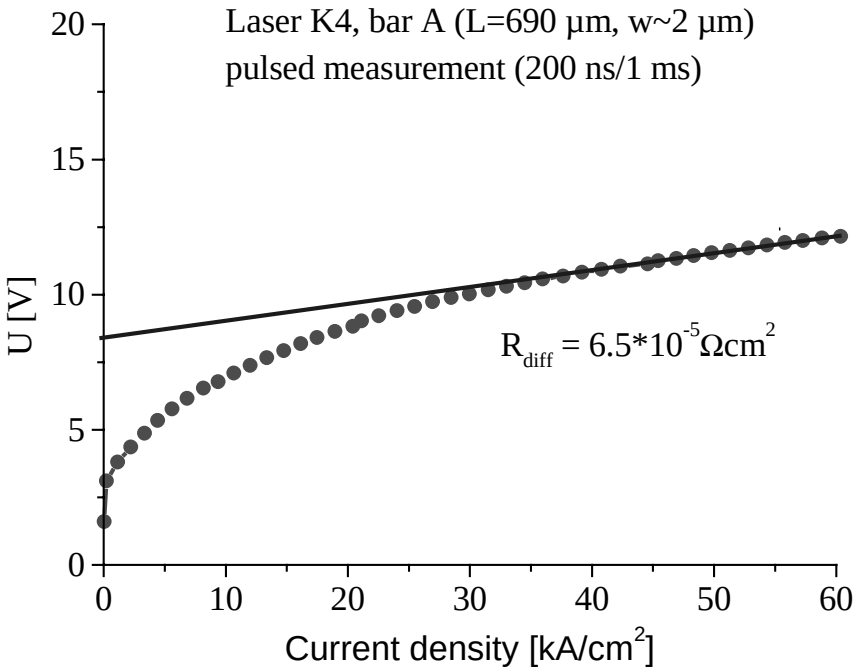

Fig. 5.1.6 Current density - voltage characteristic of an laser diode integral realized - grown and processed - "in house".

value of around $6.5*10^{-5}$ Ωcm^2, both certifying the results of processing and contact layer epitaxy developments presented previously.
Furthermore, using better quality epitaxial structures – in terms of reduced non-radiative recombination centers – provided by the company OSRAM Opto Semiconductors, one obtains, by identical processing laser operation of the diodes. As an example, in figure 5.1.7a the current-voltage (I-V) and light output–current (P-I) characteristics of such a structure processed as oxidestripe laser diode are shown. A strong indication of laser activity is provided by the suddenly, drastically increase of the light output for an injection current of about 900 mA (the correspondent voltage threshold being 12.7 V). The laser emission is further confirmed by the emission spectra of this diode measured above threshold, which is shown in figure 5.1.7b. As can be seen, the found laser emission wavelength at room temperature was around 411 nm.

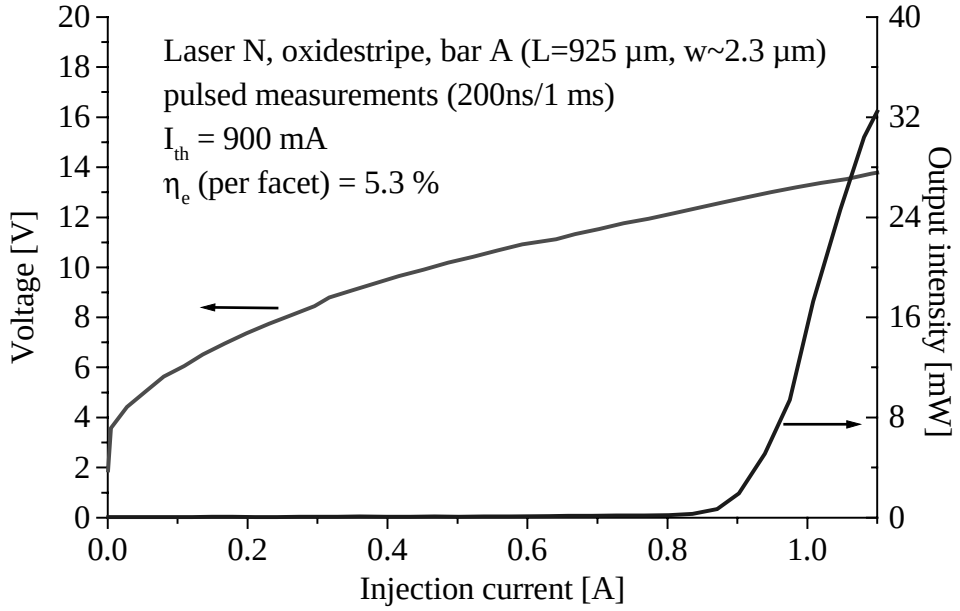

Fig.5.1.7a Room temperature current – voltage and light output – current characteristics of an oxidestripe laser diode.

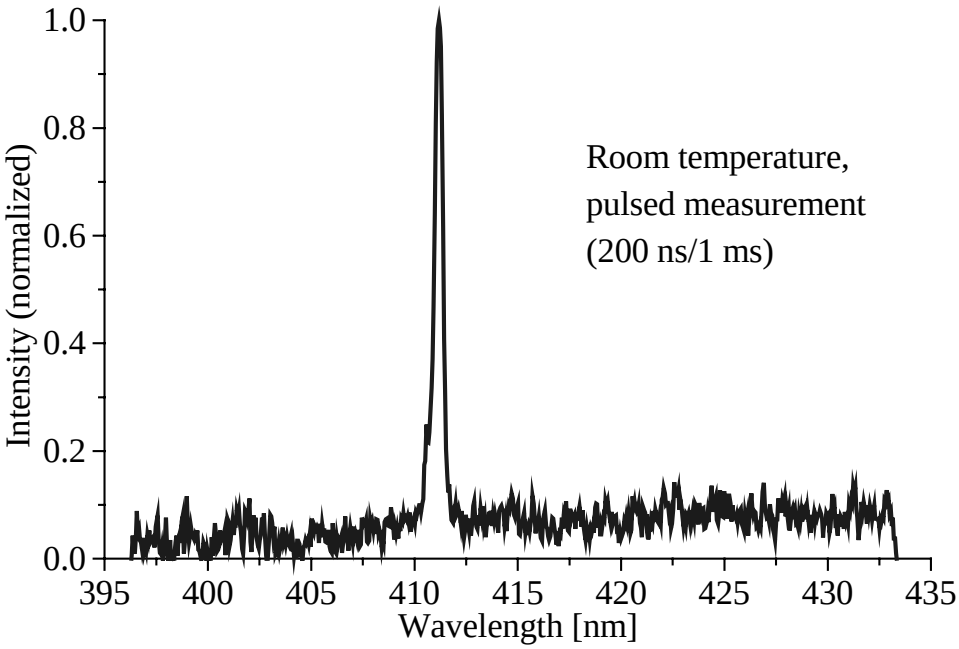

Fig. 5.1.7b Emission spectra of the laser N above threshold (I = 1.1*I_{th})

5.1.2Threshold considerations

Taking into account the diode geometry, the obtained threshold current for the diode presented in fig. 5.1.7 gives a value of around 42 kA/cm^2 for the threshold current density. Generally, this value is, of course, dependent on the laser diode geometry but also on the quality of the epitaxial structure - in case of the best structures processed during this work the obtained threshold current densities were between 20 and 30 kA/cm^2. However, these values are still high ones even for the nitrides based laser diodes.

Responsible for this could be more factors. Most probable ones could be related to: i) the quality of the mirrors – that were uncoated, and, ii) to the still high number of the non- radiative recombination centers presents in these structures as indicated by the relative low external differential quantum efficiency value. Accordingly to the relations described in the chapter 2,

$$\eta_e = \frac{dP_{out}/dI}{\hbar\omega/q} = \eta_i \frac{\alpha_m}{\alpha_m + \alpha_i} \qquad (5.1.1)$$

where η_i is the internal quantum differential efficiency, defining the percentage of the injected carriers that contribute to the radiative recombinations, and the threshold current density

$$J_{th} = \frac{qdn_{th}}{\tau_e} \qquad (5.1.2)$$

Taking into account the threshold condition for identical mirrors

$$\Gamma g_{th} = \alpha_i + \frac{1}{L}\ln\frac{1}{R} = \alpha_i + \alpha_m \qquad (5.1.3)$$

and a linear relation for the peak gain coefficient vs. carrier density such as

$$g(n) = a(n - n_{tr}) \qquad (5.1.4)$$

with a being the differential gain and n_{tr} the transparency concentration when the gain is zero, is coming out that

$$n_{th} = n_{tr} + \frac{g_{th}}{a} \qquad (5.1.5)$$

and thus

$$J_{th} = \frac{qd}{\tau_e}\left[n_{tr} + \frac{\alpha_i}{\Gamma a} + \frac{1}{\Gamma aL}\ln\left(\frac{1}{R}\right)\right] \qquad (5.1.6)$$

which further could be written as

$$J_{th} = J_0 + \frac{qd}{\tau_e} * \frac{\alpha_i}{\Gamma a} + \frac{qd}{\tau_e} * \frac{1}{\Gamma aL} \ln\left(\frac{1}{R}\right) \quad (5.1.7)$$

$$J_{th} = J_{th0} + \frac{1}{L} * \frac{qd}{\tau_e} * \frac{1}{\Gamma a} \ln\left(\frac{1}{R}\right) \quad (5.1.8)$$

where $J_0 = qdn_{tr}/\imath_e$ is the so-called transparency current density, that represents the injected current needed to reach the carrier inversion.

The significance of J_{th0} is evident: It gives the threshold current density for a laser of infinite length, representing the pure material threshold current. Therefore, finding its value by varying the laser length, could give a first indication about the source of the high threshold currents. In case of these diodes, the threshold current density change little with the laser length - by reducing the laser length at roughly a half (from 925 μm at 485 μm), the threshold current density changes only from 42 to 49.6 kA/cm^2 . As can be seen from figure 5.1.8, plotting the threshold current density versus inverse of laser length, the found value for the J_{th0} is 33.6 kA/cm^2, which remains a very high one. This means that the major source for the generally high threshold current density values in these samples is not related with the mirrors quality, but, indeed, most probable with the presence in the high number of the non- radiative recombination centers in these structures. Additional contributions to this, however, could come also from the presence of the leakage current due to carrier leakage process – where high-energy conduction electrons in the active region spill over the potential barrier into the cladding region – as well as from the existence of some current spreading –lateral spreading of the current outside the stripe region. Both have an effect of a pseudo-increase of the measured threshold current density. Anyway, by the large amount of generated heat, these high threshold currents were preventing cw mode operation of lasers.

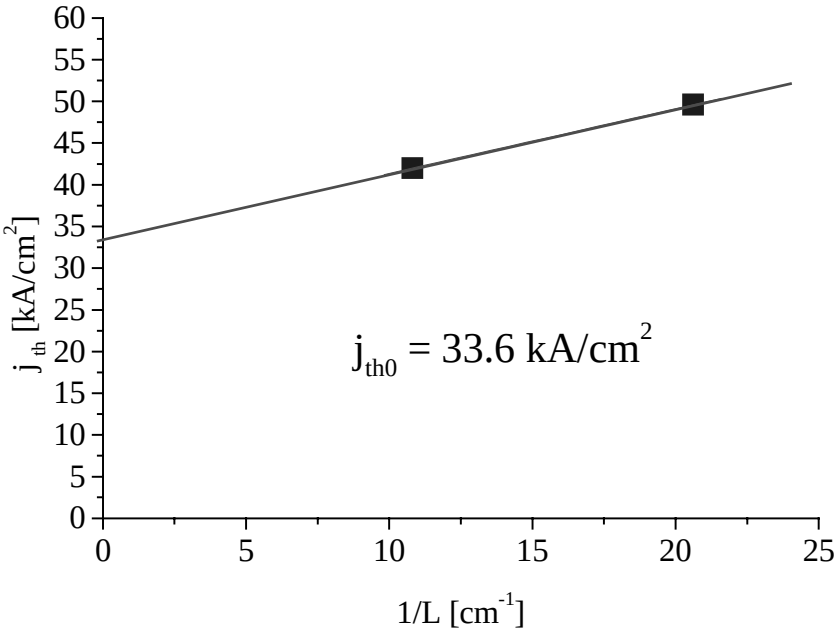

Fig. 5.1.8 Threshold current density function of inverse of laser length. From the extrapolation at infinite length is found the J_{th0}.

5.1.3 Temperature characteristic of threshold current

The temperature characteristic of the threshold current is usually formulated as:

$$I_{th} = I_0 * \exp\left(\frac{T}{T_0}\right) \qquad (5.1.9)$$

where I_{th} and I_0 are the threshold currents at absolute temperature TK, and at 0K, respectively, and T_0 is the so-called characteristic temperature which characterizes the temperature dependence of threshold current and is an important parameter of the laser diode. Accordingly to Eq. 5.1.9, the temperature dependence of the laser diode becomes weaker – therefore more stable – for larger value of T_0. In order to determine this parameter for the obtained laser diodes, there were done P-I measurements at various temperatures.

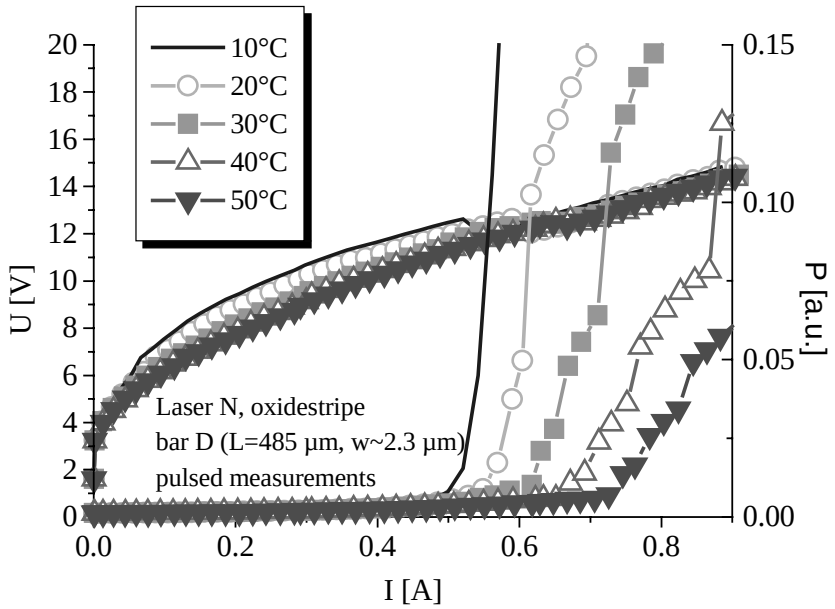

Fig.5.1.9a I-V and P-I characteristics of an oxidestripe laser diode measured at different temperatures. The observed kink in the P-I characteristic can be attributed to a transversal mode jump.

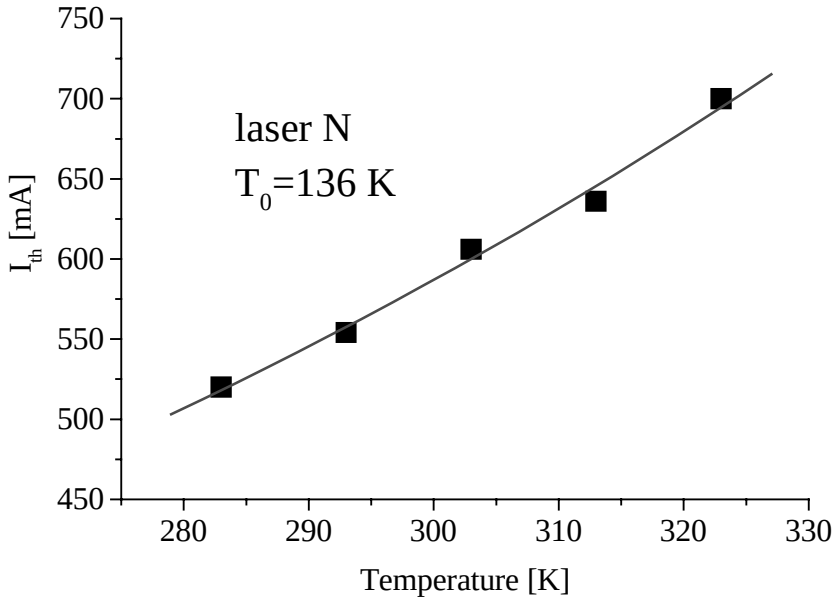

Fig. 5.1.9b Threshold current – temperature dependence extracted from P-I measurements shown in fig 5.1.9a. The characteristic temperature T_0 is calculated using Eq. 5.1.9.

From the obtained data, some of which are shown in figure 5.1.9a, it was estimated the threshold current for every temperature, and, using Eq 5.1.9, it was calculated T_0 (figure 5.1.9b). The found value, of 136 K, is itself a high one and concords well with those reported by others authors [Kuramata98], [Kneissl00] for GaN on SiC laser diodes. In the same time, because this relatively high value of T_0 is associated also with high threshold current values it gives an indication that defect recombination plays an important role in these diodes.

5.1.4 Temperature characteristic of the lasing wavelength

An important parameter, especially from applications point of view, of any laser diode is its lasing wavelength dependence on temperature. In order to investigate this characteristic lasers emission spectra measurements at various temperatures were performed. An example is shown in figure 5.1.10a,b where there are depicted the emission spectra of a processed laser diode

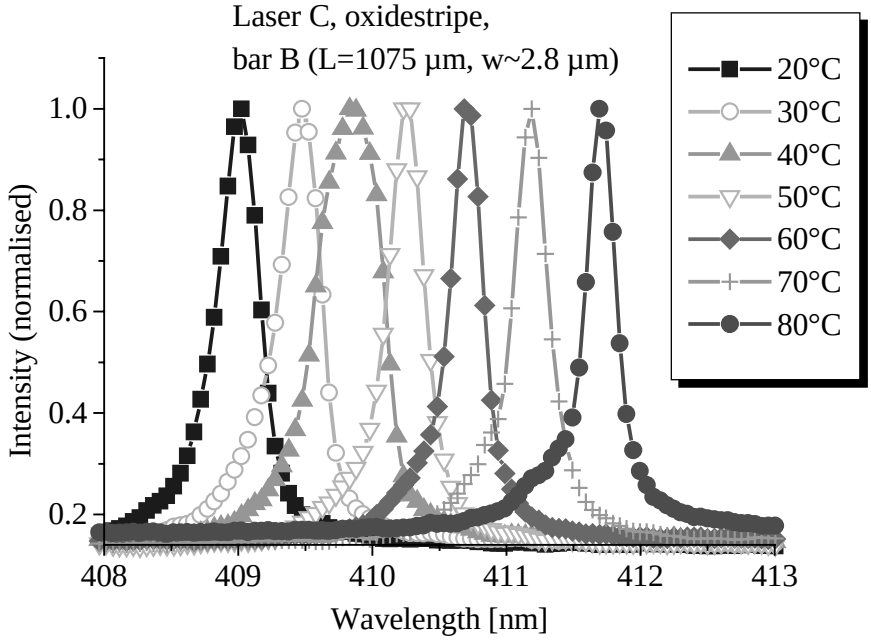

Fig. 5.1.10a Emission spectra of an obtained oxidestripe laser diode measured in the pulsed mode (200ns/1ms) at different temperatures.

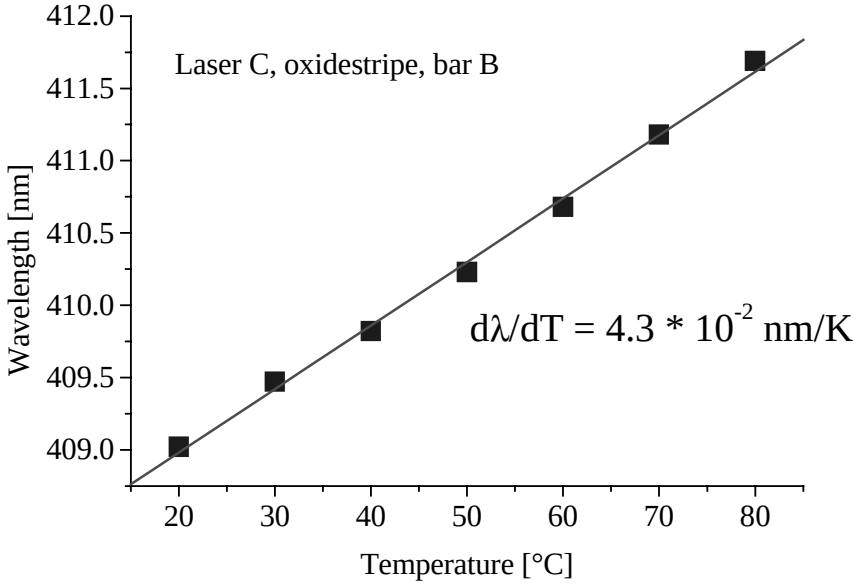

Fig. 5.1.10b Laser emission wavelength as function of temperature obtained for the measurements from fig. 5.1.10a.

measured at different temperatures between 20° - 80° C (fig. 5.1.10a), and the obtained dependence of the lasing wavelength on temperature (fig. 5.1.10b). Firstly should be mentioned that, as can be seen, the diode was showing laser emission in the pulsed mode at temperature as high as 80° C. Secondly, that the obtained wavelength shift with temperature - of 4.3 * 10^{-2} nm/K (-0.31 meV/K) for this laser diode - is a very low one, at least one order of magnitude lower than for long-wavelength Fabry-Perot lasers, and it is lower also than the reported value of 6.5 * 10^{-2} nm/K (-0.47 meV/K) for an optical pumped GaN laser [Hoffmann00]. More than this, after performing similar measurements on laser diodes fabricated on different epitaxial wafers, it was found that the value of wavelength shift with temperature seems to depend also on the epitaxial wafer – for example in case of the diodes from sample N presented in fig. 5.1.7 –9, the found value was 3 *10^{-2} nm/K (-0.2 meV/K) – but, anyway, generally these values were lower than 4.5 *10^{-2} nm/K (-0.33 meV/K).

How these results could be understood? Well, firstly, it should be taken into account that in the case of the Fabry-Perot laser diode the lasing wavelength is determined by the gain profile (gain peak) of the laser medium, therefore its change with temperature follows the gain peak. The temperature coefficient of the peak wavelength of the laser gain is given using the bandgap energy E_g of the laser medium as

$$\frac{d\lambda_g}{dT} = -\left(\frac{hc}{E_g^2}\right)\left(\frac{dE_g}{dT}\right) \qquad (5.1.10)$$

where h and c are Planck's constant and the velocity of light in vacuum, respectively. Therefore, it is expected that, due to its large material bandgap, a GaN based Fabry-Perot laser diode will have a weaker wavelength shift with temperature than its long-wavelength counterparts, being more stabile from this point of view against temperature variations.
Furthermore, this stability could be enhanced in case of the GaN based lasers by another feature specific to nitrides: the presence inside the epitaxial structure of strong piezo- and (spontaneous) polarization fields. These fields, giving rise to a strong quantum confined Stark effect (QCSE), led to a reduction of the effective bandgap and accordingly, to a red-shift of the quantum well emission with respect to an ideal square potential well. By increasing the carrier concentration, these fields could be partly screened, therefore leading to an increase of the effective bandgap and consequently to a blue-shift of the emission wavelength. Therefore, in case of the nitrides, the temperature-related bandgap shift of the gain curve it's modified by these internal polarization fields. This situation is schematically depicted in figure 5.1.11a - f. As can be seen, there are two counterbalancing effects in the bandgap shift, and, accordingly, in the emission wavelength one with temperature: a red shift induced by the temperature increasing via the reducing of the bandgap Eg with the quantity dEg, and a blue shift induced by the increased screening of the internal fields by injected carriers at higher temperature. Consequently the effective bandgap

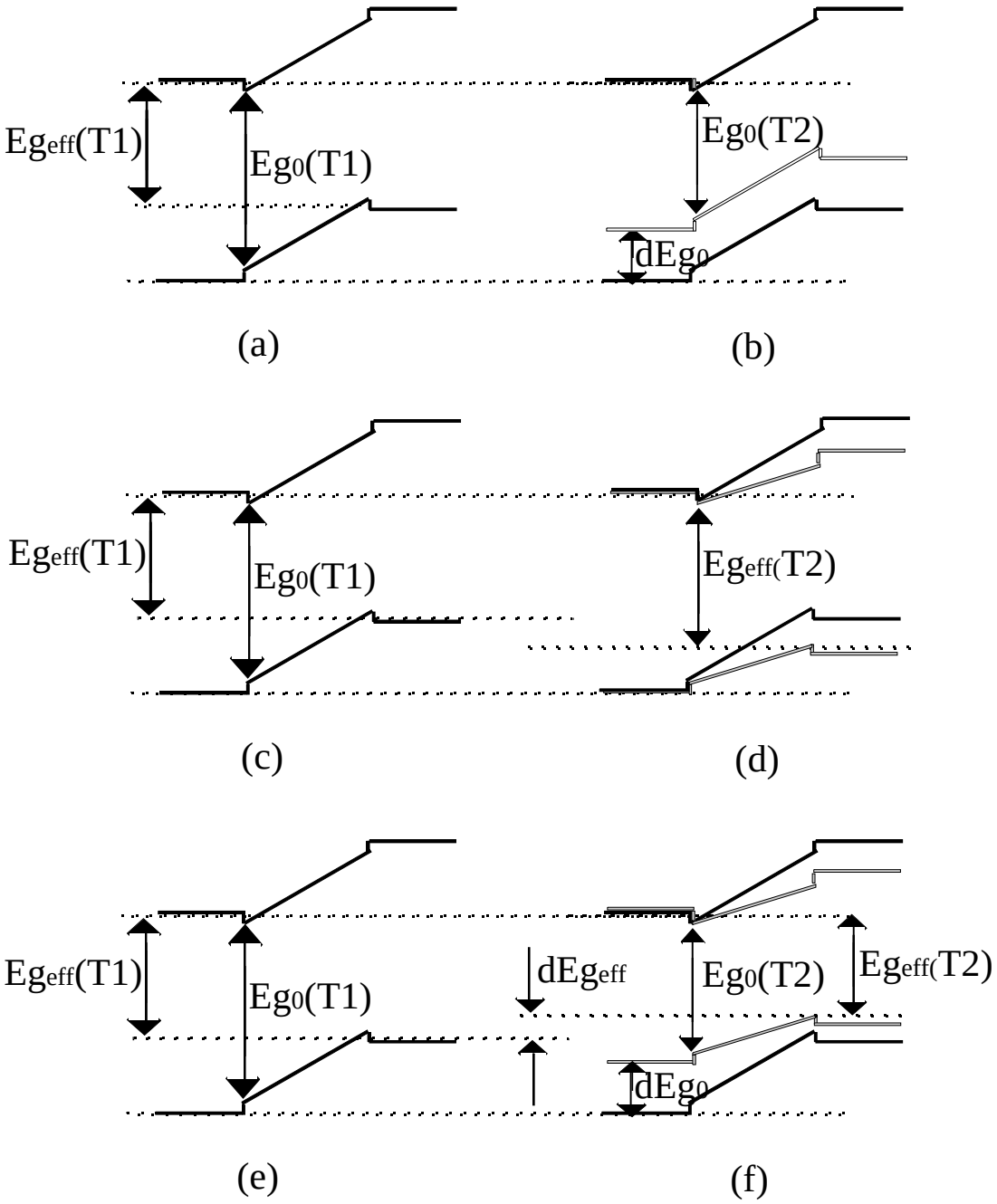

Fig. 5.1.11 Schematic view of the quantum well with built-in field and effects of increasing the temperature from T1 at T2>T1: (a) – (b) the "pure" bandgap reduction by increasing temperature resulting in a red-shift; (c) – (d) the "pure" Eg^{eff} increase by the increased screening of the internal fields by injected carriers at higher temperature, leading to a blue-shift; (e) – (f) the superposition of both effects - the real situation

reduction dEg^{eff} could be significant smaller than the nominal one dEg and, therefore, accordingly to Eq 5.1.10, the resulting emission wavelength change with temperature could be smaller that the one expected for the material without any built-in fields present. Based on these considerations, it can be imagined that, eventually the fabrication of a laser diode with extremely high wavelength stability against temperature variation is possible, if the internal fields could be precisely controlled (so to obtain for a temperature variation a dEg^{eff} ~0)

However, coming back to the obtained results, it should be pointed out that in the case of complete screening of the built-in field by the injected carriers, the wavelength shift with temperature should be that predicted by Eq 5.1.10 for the nominal Eg. This was confirmed by Hoffmann [Hoffmann00] comparing the value – of 6.5 * 10^{-2} nm/K (-0.47 meV/K) - found for the optical pumped GaN laser with the published bandgap temperature coefficient of GaN (-0.45 - -0.67 meV/K). Therefore, the systematically lower values found here-<4.5*10^{-2} nm/K (-0.33 meV/K)- for the obtained laser diodes, suggest that in this case, of the electrically injected lasers, the screening of the internal polarisation fields by the injected carriers is incomplete (in optically pumped structures the overall carrier densities are higher and therefore the internal fields are screened more efficiently). Therefore the remaining unscreened fields could be held responsible for lower values of the wavelength shift as well as for the observed variation of these values for different epitaxial wafers, every grown probably with its own built-in field.

Further confirmation of this incomplete fields screening in case of the electrically injected lasers will be shown in the chapter related to the DFB laser.

5.1.5 Current spreading investigations.

As mentioned in the previous section, in the oxidestripe lasers diodes a possible source for increasing the threshold current density consists in the lateral spreading of the current outside the contact region which lowers the peak concentration of carriers at the center of the stripe below the value that would apply in a broad contact laser at the same current density. Therefore, the current density flowing into the stripe must be increased to counteract this effect. To account for the current spreading effect, which is schematically depicted in figure 5.1.12, an approximate formula for the injected current density J(y) can be used [Chuang95]:

$$J(y)=\begin{cases} J_0 & |y| \le w/2 \\ J_0 e^{-K|y|-w/2} & |y| \ge w/2 \end{cases} \qquad (5.1.11)$$

where y is the lateral direction and w is the contact stripe width.

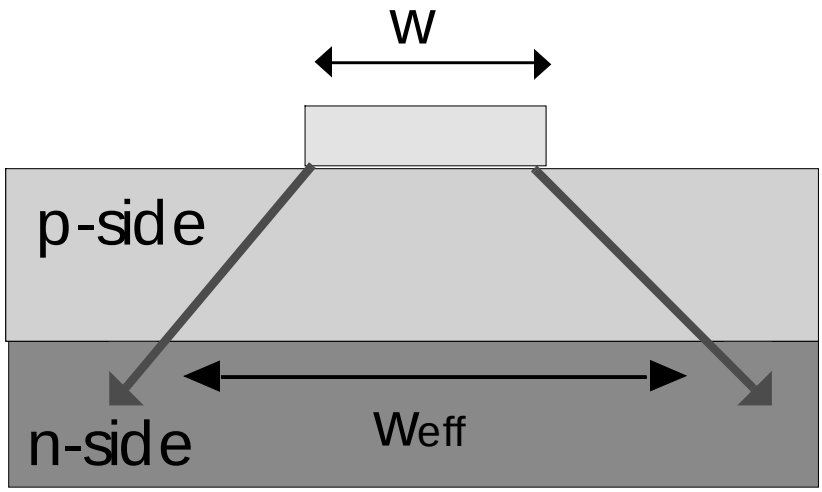

Fig.5.1.12 Schematic representation of the current spreading along lateral direction in the stripe lasers

Therefore, in order to estimate if such effect exists and could be partly responsible for the high threshold current density obtained

in the case of the fabricated laser diodes, it was necessary to investigate the current spreading in these structures. This could be realized by comparative I-V measurements on diodes having various contact stripe widths and also comparing the oxidestripe structures with their ridge-waveguide counterparts - in which the lateral current flow is restricted by ridge fabrication.
If the current is not spreading laterally, being confined to the region under the contact, then the effective width w_{eff} = w (see fig. 5.1.12) and the diode area (A=L*w) is the same as the p-contact one. In this case, the current density should only depend on the applied voltage but not on the contact width, or more generally, on its geometry or size. This was nicely verified by measuring I-V characteristics on laser diodes with the same width but different stripe lengths – terminated by normal cleaved facets, therefore restricting physically the current spreading in the longitudinal direction – and calculating the correspondent current density curves. As can be seen in figures 5.1.13a,b, indeed, the current is proportional with the contact area (I=j*A=j*L*w) therefore, extracting the area influence one obtains the same current density-voltage characteristic for various laser lengths.
In contrast to this, in the case that the stripe length is kept constant and the width is varied the obtained result is totally different. As can be seen in figure 5.1.14a,b, the current density depends strongly on the stripe width, decreasing, at a given voltage, with the increase of the stripe width. This is similar to say that the current – which is physically measured – is not any more direct proportional with the “nominal” diode area – that meaning the p-contact area – which is also measured. A direct comparison of these two opposite behaviours can be seen in figure 5.1.15, where is plotted the measured current through the diode at a given voltage (12V) versus nominal diode area. Therefore these results suggest, at least at a first glance, that in the present structures exists a strong current spreading effect, with a spreading length of at least few tens of μm. This can be seen comparing stripe widths of 32 μm and 64 μm in figure 5.1.14.
In order to determine more accurately this spreading length, it was necessary to extend the stripe width variation beyond 64 μm.

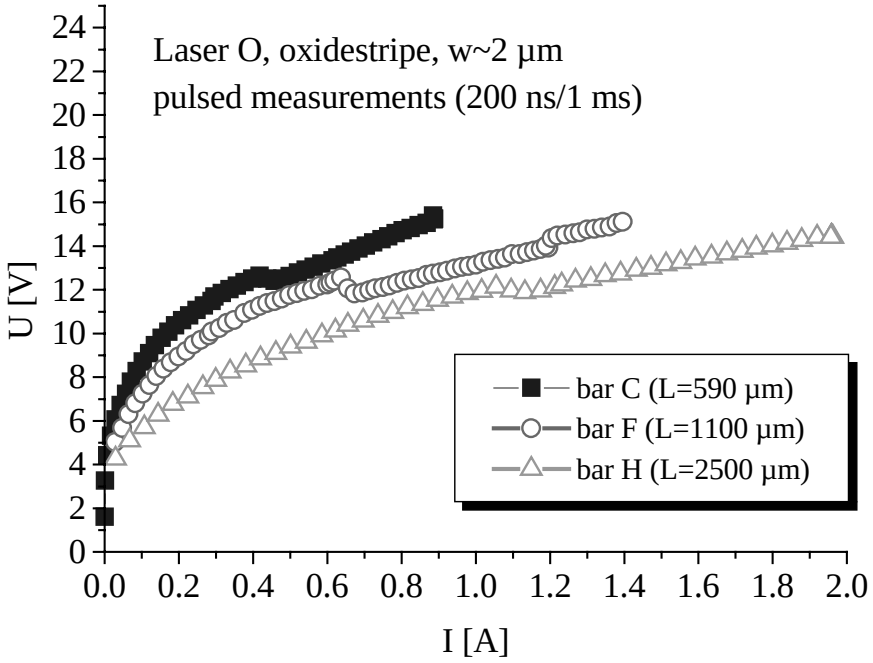

Fig. 5.1.13a I-V characteristics on oxidestripe lasers having the same stripes width but different lengths.

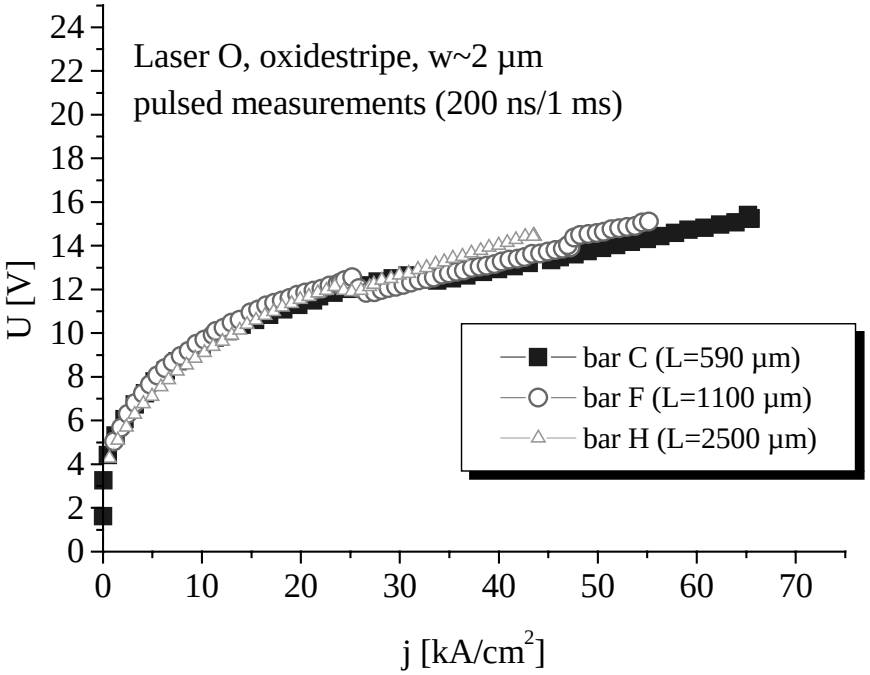

Fig. 5.1.13b Current density-voltage characteristics corresponding to the I-V ones from fig. 5.1.13a

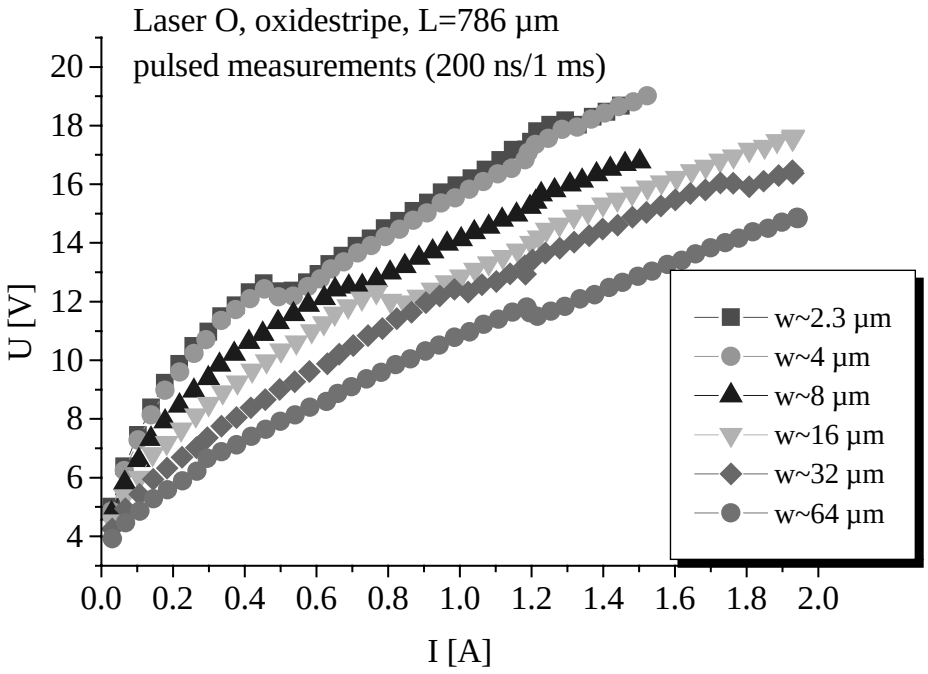

Fig. 5.1.14a I-V characteristic on oxidestripe lasers having the same length but different stripe widths.

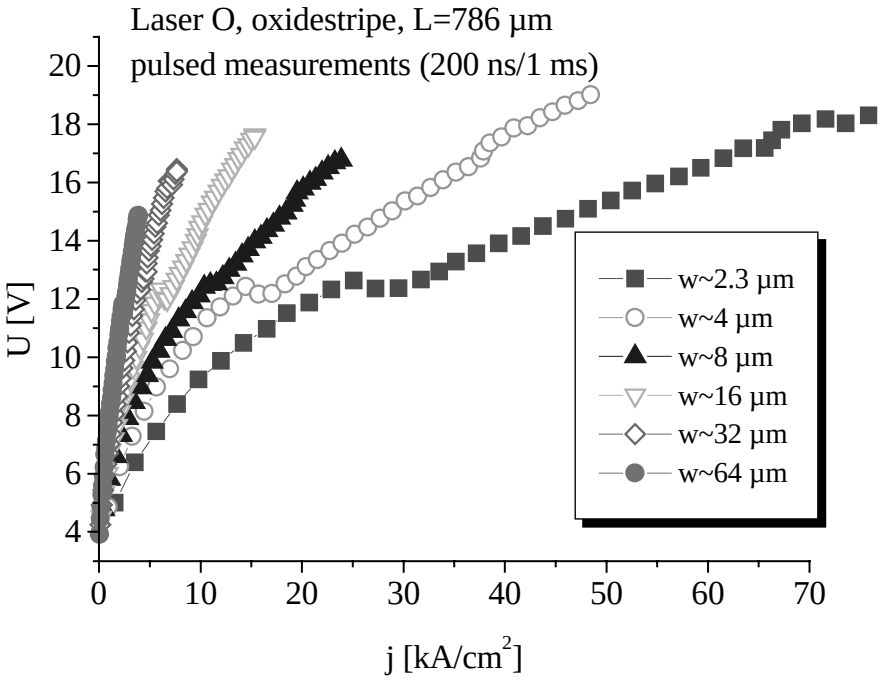

Fig. 5.1.14b Current density-voltage characteristics corresponding to the I-V ones from fig. 5.1.14a

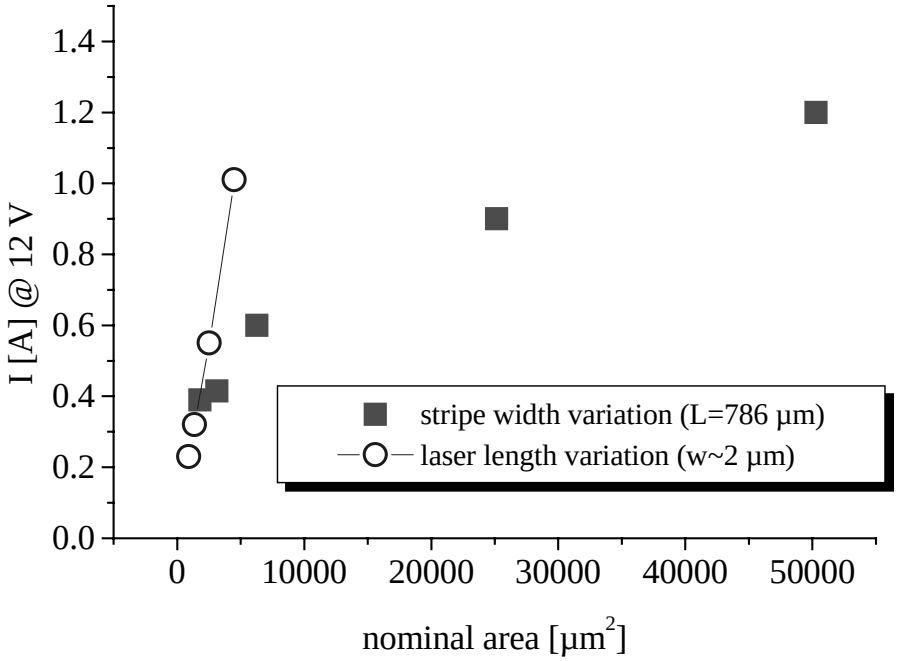

Fig. 5.1.15 Diode current at a certain voltage (12V) versus nominal diode area (p-contact area) for the diodes showed in fig. 5.1.13, 14

As there was no possibility to realize it practically the variation was simulated by segmenting the p-contact of a long, 2-μm wide stripe using the method applied for the 2-segments optical measurements. In this way one obtains stripes with the same width and various lengths – from 35 to 567 μm, but without cleaved ends, as shown schematically in figure 5.1.16. This therefore enables the observation of the current spreading effect. From the I-V characteristics measured on these segments (fig. 5.1.17a,b) one can see that for the short segment lengths the current density – voltage curves are again starting to deviate from the reference one – measured on a long, normal laser, with cleaved facets. Therefore it seems that again it is seen the current spreading effect, the diode current being not direct proportional with the nominal contact dimensions, for the short segments. Indeed, this is clearly seen plotting again the measured current through the diode at a given voltage (12V) versus nominal segment length (figure 5.1.17c).

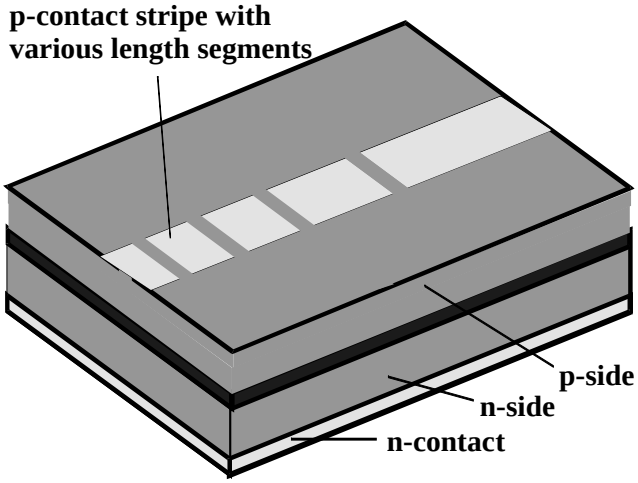

Fig. 5.1.16 Schematic view of the multi-segments device used for current spreading distance estimation

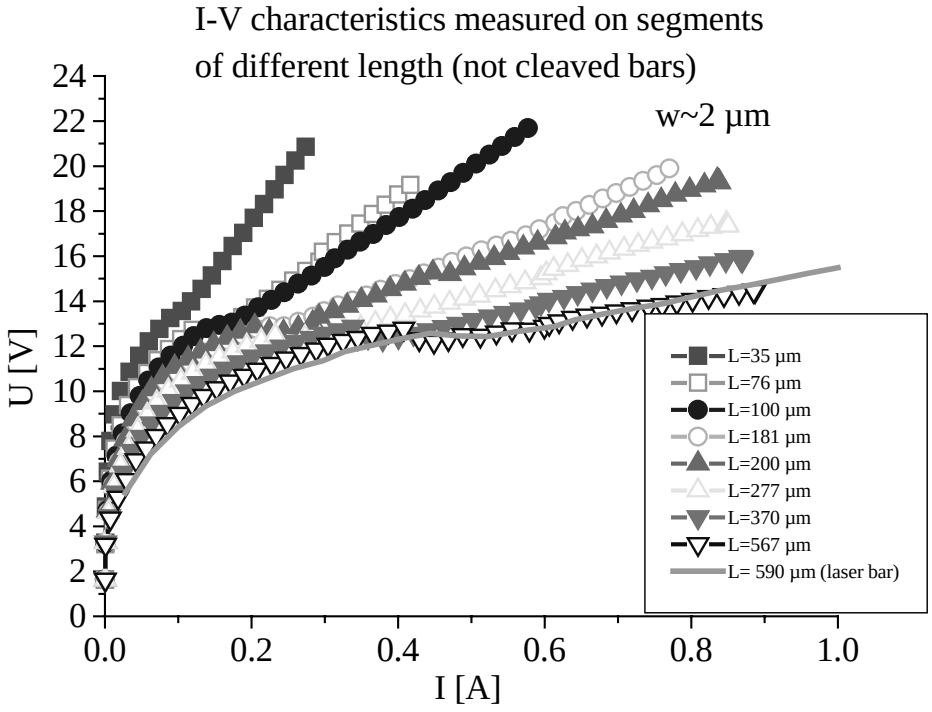

Fig. 5.1.17a I-V characteristics measured on the various length segments indicated in fig. 5.1.16. As reference was measured also the long, cleaved-ends oxidestripe laser.

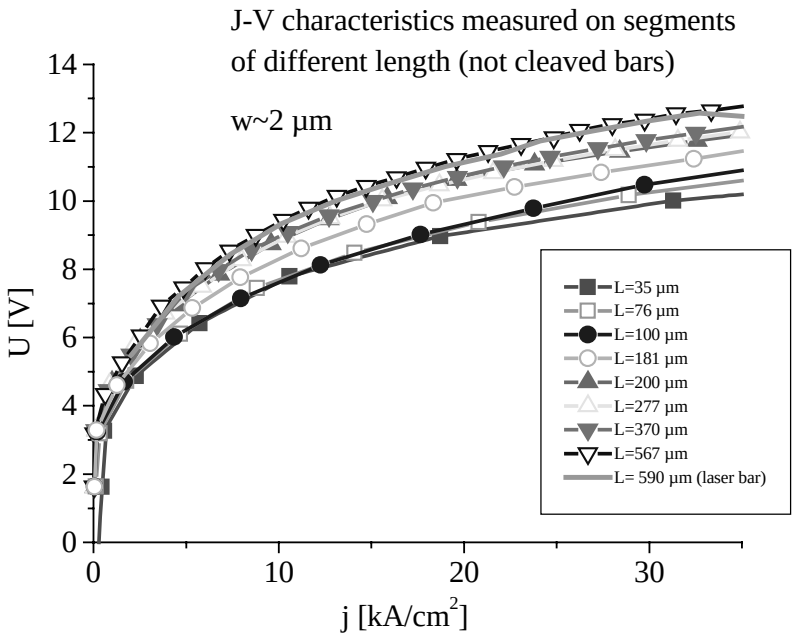

Fig. 5.1.17b Current density-voltage characteristics corresponding to the I-V ones from fig. 5.1.17a

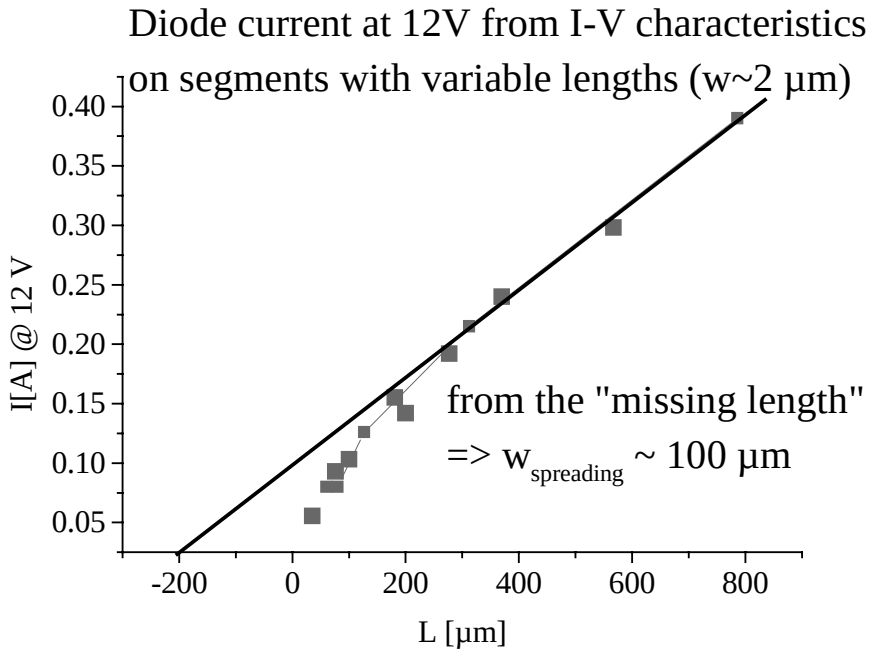

Fig. 5.1.17c Diode current at a certain voltage (12V) versus nominal segments length extracted from fig. 5.1.17a

By extrapolating at zero the linear dependence from the long segments region - where the current spreading is not observable because the spreading distance is small comparative with the contact dimension – could be estimated a value of around 100 μm of this distance (for each end of the segment).
To find such a strong current spreading effect in these laser diodes is quite surprisingly, taking into account the high resistivity of the bulk p-(Al)GaN layers (especially of the clading one). A relatively important current spreading in GaN based laser diodes was reported only in case of using an AlGaN:Mg/GaN:Mg strained layer superlattice (SLS) in the structure [Böttcher03]. In that case the twodimensional hole gas which forms at the interfaces of the SLS leading to an anisotropy of the conductance and enhacing the in-plane carrier transport was found to be responsible. Such an effect, however, should not be present in our structures, which have a bulk cladding layer.
However, fortunately it is an easy way to check if, indeed, such a strong current spreading appears on the p-side of these laser diodes. This is shown by comparison of oxidestripe and ridge-waveguide diodes. Even, if, a direct comparison of the threshold current densities in the two types of structures was not possible to be done because the used samples were showing no laser emission, the current spreading effect should be already evidenced by I-V measurements. As already mentioned, in the ridge-waveguide structure case, the lateral current flow is restricted by the ridge itself (see figure 5.1.18 a,b). Therefore the presence of such a strong current spreading should show a clear difference in the current density-voltage characteristics. However, after direct comparison between oxidestripe diodes and “normal” ridge-waveguide ones – with the ridge height smaller than the thickness of the p-side of the epitaxial structure (like in fig. 5.1.18b) – it was found, as can be seen from figure 5.1.19, no difference in the current density-voltage characteristics. Therefore, this result suggests that, if the current spreading exists, it can’t be localized in the upper part of the p-side of the epitaxial structure.

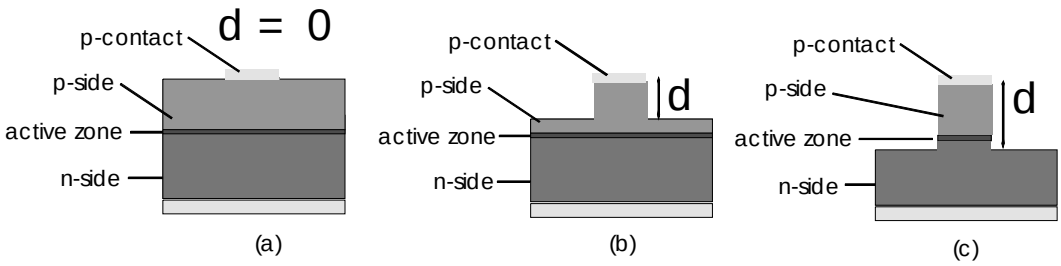

Fig.5.1.18 Schematic view of the oxidestripe (a) and ridge-waveguide (b,c) structures. In the case of the ridge structure shown in (c) the ridge height d is larger than the thickness of p-side of the structure - the etching is done also through the active zone.

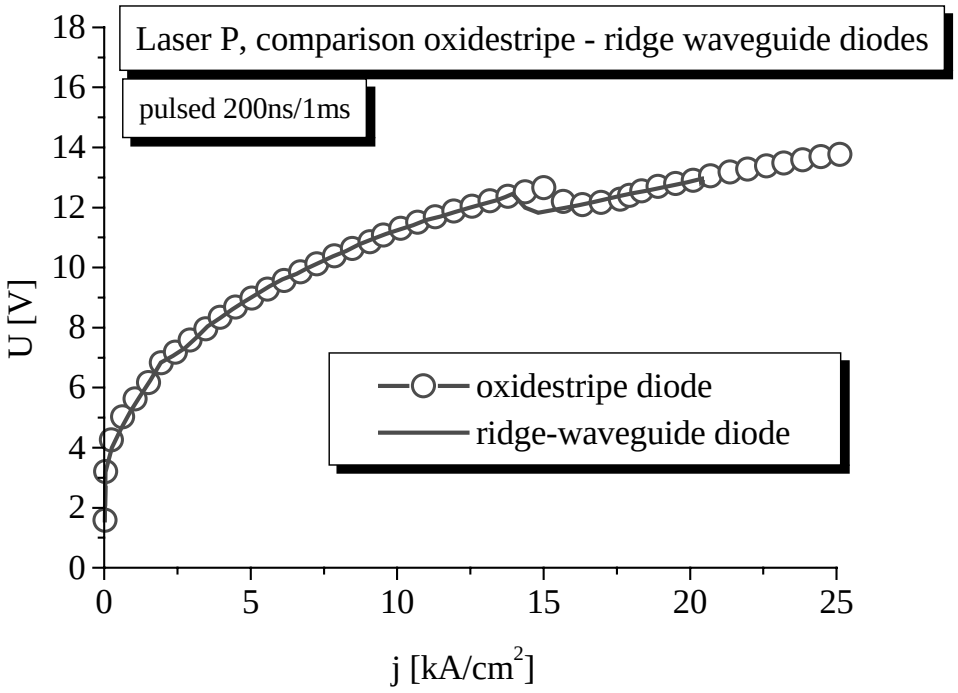

Fig. 5.1.19 Current density – voltage characteristic of oxidestripe and respectively ridge-waveguide diodes processed on the same wafer. The ridge height was in this case smaller than the p-side layers thickness (see fig. 5.1.18b). The kink present on both characteristics is a measurement artefact.

In order to clarify if it could happens still in the p-side, but very close to the active zone there were also investigated ridge-

waveguide diode structures having different ridge heights, in the extreme case, being larger than the overall thickness of the p-layers (like in fig. 5.1.18c). The resulting current density – voltage characteristics, which are displayed in figure 5.1.20, show no differences between different ridge heights d, even for that with d larger than the entire p-side of the structure.
Therefore, these experiments demonstrate that on the p-side of the diode structure, and thus also in the active region, appears no significant current spreading effect. That means also that the current spreading effect couldn't be thought responsible as a major contributor to the found large threshold current densities.

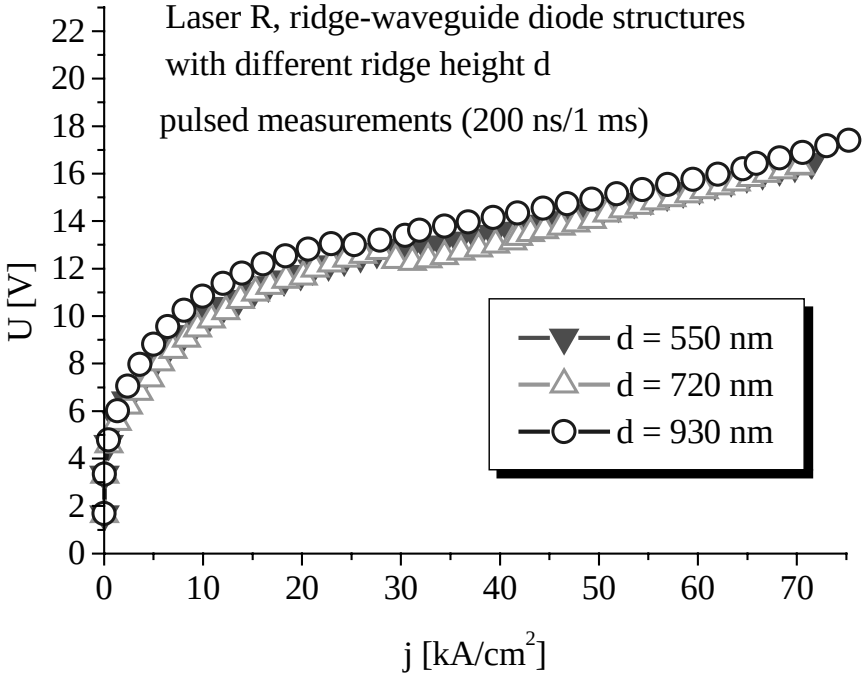

Fig. 5.1.20 Current density – voltage characteristics of three ridge-waveguide diode structures with different heights d of the ridge. For the largest d, the ridge starts from the n-side of the structure (corresponding to fig. 5.1.18c).

Once clarified the fact that on the p-side of the diode no appreciable strong current spreading effect occurs, it remains anyway interesting to understand in which way the observed current spreading, which must be localized on the n-side of the

structure, leads to the observed effects on the I-V and their correspondent current density-voltage characteristics. Because on the p-side of the structure no any important current spreading is present, the p-n junction area is the same as the p-contact one. Therefore the observed effect on the I-V characteristics can come only via a resistance situated in the n-side of the structure. This is clearly seen writing the diode equation considering also a series resistance:

$$I = I_0\left[\exp(q(V - IRs)/kT) - 1\right] \qquad (5.1.11)$$

If the series resistance is supposed to arrive mainly from the p-contact, therefore being written like Rs= ρ/Ap, where ρ is the contact resistivity and Ap is the area of the p-contact and - without any current spreading - also of the diode, one obtains for the current density

$$j = I/A = \left(j_0 Ap/Ap\right)\left[\exp(q(V - j\rho Ap/Ap)/kT) - 1\right]$$
$$j = j_0\left[\exp(q(V - j\rho)/kT) - 1\right] \qquad (5.1.12)$$

It is evident that with this assumption, the current density will not depend on the contact geometry or size. But if the series resistance has an additional component coming from the n-side of the structure which could be also written as Rn = ρ_n/An and whose area An is much larger than that of the diode and p-contact, Ap, the current density will depend on both Ap and An, or more exactly on their ratio, as could be seen if the diode equation is rewritten with Rs = ρ/Ap +ρ_n/An:

$$j = j_0\left[\exp(q(V - jAp(\rho/Ap + \rho_n/An))/kT) - 1\right]$$
$$j = j_0\left[\exp(q(V - j\rho - j\rho_n Ap/An)/kT) - 1\right] \qquad (5.1.13)$$

Now it is easy to understand the current-density – voltage characteristics behaviour observed in figures 5.1.13-15: it is not related to a change of the ratio between p-contact area and p-n junction area, since these two are identical without any current spreading in the p-side of the structure, but it is related to a change of the ratio Ap/An. This is tried to illustrate schematically in figure 5.1.21. This ratio depends on the way in which the p-contact area Ap is varied: In the case where the length of the cleaved laser bar is changed, the Ap and An change themselves in the same way, so their ratio is constant and do not influence the current density – voltage characteristics (like in figure 5.1.13); In the case that the width of the p-contact stripe is varied – let's say by Δw, and therefore Ap is varied by $\Delta Ap = L*\Delta w$, the An varies also, supposedly by $\Delta An = L*\Delta w = \Delta Ap$ but, due to the large difference in their initial widths values, its relative change is much smaller than of the Ap one, and therefore the ratio Ap/An changes to $(Ap+\Delta Ap)/(An+\Delta Ap)$ and accordingly changes also the current density – voltage characteristic (like in fig. 5.1.14).
However, is it plausible to assume such a series resistance situated on the n-side of the structure and to assume that its contribution to the total series resistance is significant? Well, if the figure 5.1.14a is inspected more closely, the answer is definitely "yes": by changing the stripe width from, let's say, 2 to 64 µm, that means by a ratio of around 30, the Ap increases in the same manner and therefore the series resistance coming from the p-side of the structure, $Rp=\rho/Ap$, should decrease by a factor of around 30. But the real differential resistance of the structure (the slope of the I-V characteristic) is visible barely changing! Comparing the larger widths, for example 16 and 64 µm, it is even clearer that basically the I-V slope is not changing, even if the p-contact area is varied by a factor of 4. Therefore, it is clear that, inside the total series resistance exists a component which is not influenced, or it is very less influenced, by a change of the p-contact area and thus of the p-side resistance, and which account significantly to the total series resistance. This is true at least for the diodes with larger stripes, for which the p-contact resistance has to be already a very small one.

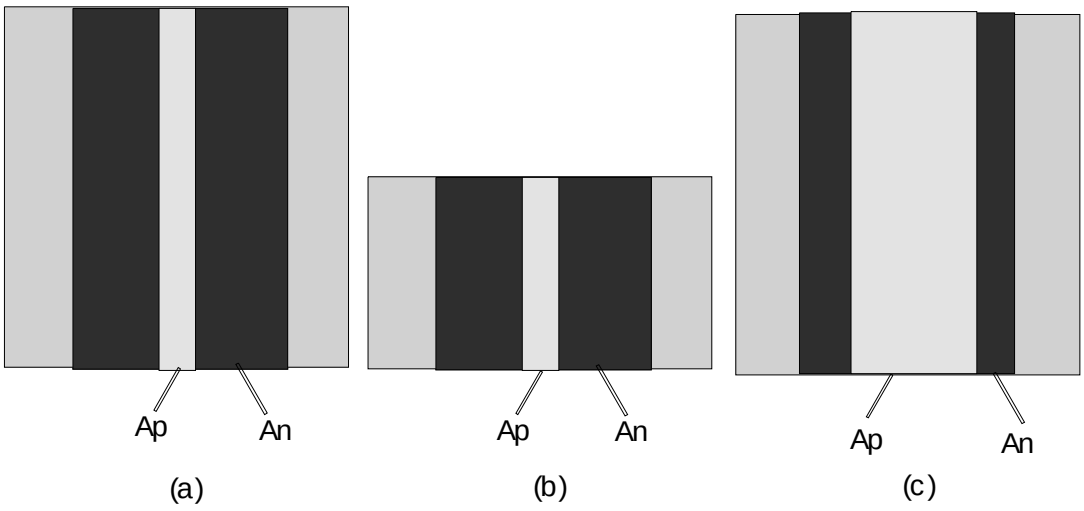

Fig. 5.1.21 Schematic top view of the ratio Ap/An variation with changing the Ap size and geometry; (a) – (b) compares the two areas variation in case of a change in the length of laser diode – with cleaved ends – corresponding to fig. 5.1.13; (a) – (c) compares the same variation in case that the width of the p-contact is changed – corresponding to fig. 5.1.14

This conclusion is important because, on the one hand, this certifies the quality of the obtained p-contact, whose contribution to the total series resistance of these laser diodes is not anymore an extremely important one – this is remarkable since one of the major problems encountered in GaN laser diodes is related to the high series resistance coming from the p-contact. On other hand this findings indicate that for further improvements related to further reduction of the series resistance and overall voltage drop on the device, significant attention has to be paid to the n-side of the diode structure.
Regarding the physical source of this n-side resistance, besides the SiC itself and n-contact, an important contribution could come also from the heterointerface SiC- nitrides, which, as it has been found by Kuhn [Kuhn02], could be a highly resistive one. But, for a more precise picture regarding this, and also the exact location of the associated current spreading effect, more investigations in this direction are still remaining to be done.

Anyway, as a conclusion of this section, it could be said that no such significant current spreading effect on the p-side of the diode structure could be found, - at least in the measurement limit of these experiments. Therefore the current spreading effect could be neglected as a major contributor to the observed large threshold current densities. The most plausible source responsible for this remains the presence of the high number of the non-radiative recombination centers in these structures, as already mentioned previously. An important current spreading was found to be present on the n-side of the diode structure associated with a resistance which has a significant contribution at the total series resistance of the device. This resistance should be taken into account for the further optimisations of GaN laser diodes.

5.1.6 Thermal resistance investigations.

As already discussed (chapter 5.1.3) the threshold current I_{th} of a semiconductor laser depends exponentially on the temperature. I_{th} increases exponentially with the temperature which in turn increases with current injection due to the heat generation. Therefore a situation can occur where an increase in drive current causes a rise in temperature of the active region which in turn causes I_{th} to increase more than the original increase in the drive current. This can not only prevent the cw laser operation but can lead also to its destroying by thermal runaway. Responsible for the heat generation is mainly the Joule heating in the contacts and series resistance. Additionally, heat is generated by non-radiative recombination within the thickness of the active layer and also by re-absorbtion of the spontaneous emission in the substrate, contact, or unpumped parts of the active layers - especially in high-power lasers.
Anyway, it's clear that, besides trying to reduce as much as possible the heat generation, another important aspect that should be taken into account for the laser diodes optimization, is the heat dissipation and removal, especially from the active zone region. To account for this, an important parameter of the laser diode is its thermal resistance defined as

$$R_{th} = \Delta T_{act} / P_{th} \qquad (5.1.14)$$

where ΔT_{act} is the temperature rise in the active layer and P_{th} is the heat generation rate. P_{th} could be expressed as the difference between the total electrical power supplied to the laser and its light output power $P_{th} = P_{el}-P_{opt} = U*I-P_{opt}$. Considering also $U=U_{th}+I*Rs$, true for $I>I_{th}$, where Uth is the threshold voltage and Rs the series resistance, it could be expressed the active zone temperature T_{act} as

$$T_{act} = T_S + R_{th}(IU_{th} + I^2 R_S - P_{opt}) \qquad (5.1.15)$$

with Ts being the heat sink temperature.

Using the Rth value also other important parameters for laser diode operation like the maximum operation temperature defined as the temperature for which the output power vanishes [Thompson80,Makino97,Hatakoshi99,] can be estimated. Also the cw lasing condition [Drenten94] given as:

$$F = T_0 /(2.7 * I_{th,p} V R_{th}) > 1 \qquad (5.1.16)$$

where T_0 is the characteristic temperature, Ith,p is the pulsed threshold current, and V is the voltage drop over the laser.

As already mentioned, in the case of the laser diodes obtained during this work, cw operation was not possible to achieve. The main reason for this were the overall large threshold currents attained, which in their turn, as previously discussed, are due, besides to the poor reflectivity of the uncoated mirrors, mainly to the high number of non-radiative recombination centers presents in these samples. However, as suggested by the above cw lasing condition, another critical parameter from this point of view could be also the thermal resistance of the fabricated laser diodes. That, indeed, this was the case, it is suggestively illustrated by comparing the obtained lasers characteristics measured at various temperatures – heat sink ones – and, respectively at various duty-cycle ratios. As can be seen from figures 5.1.22a,b, the laser behavior is very different in the two cases. By increasing the heat sink temperature, at a constant duty-cycle ratio, the P-I characteristics indicate a significant - exponential - increase of the threshold current, as already presented in the section 5.1.3. In this case, at a temperature increase from 23° to 65°C, the threshold current increases from 0.88A to 1.18A. The effect of increasing the pulse duty-cycle ratio on the same laser diode while keeping the heat-sink temperature constant is quite different. For a duty-cycle increase from 0.02% to 4% the threshold current remains under 1A, but the output power and the external quantum differential efficiency indicated by the slope of the P-I curve visibly decrease dramatically (even if numerical values are not indicated because unfortunately the photodiode

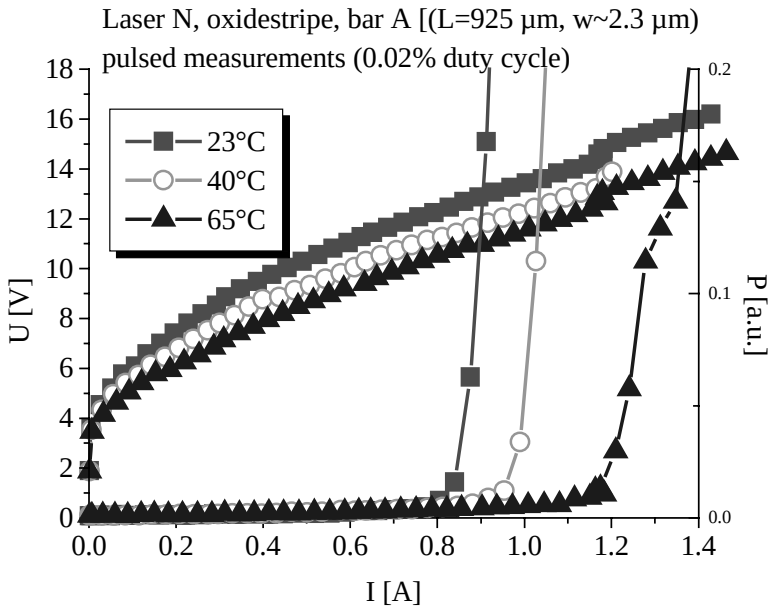

Fig. 5.1.22a Pulsed (0.02% duty-cycle) I-V and P-I characteristics of an oxidestripe laser diode measured at various (heat sink) temperatures.

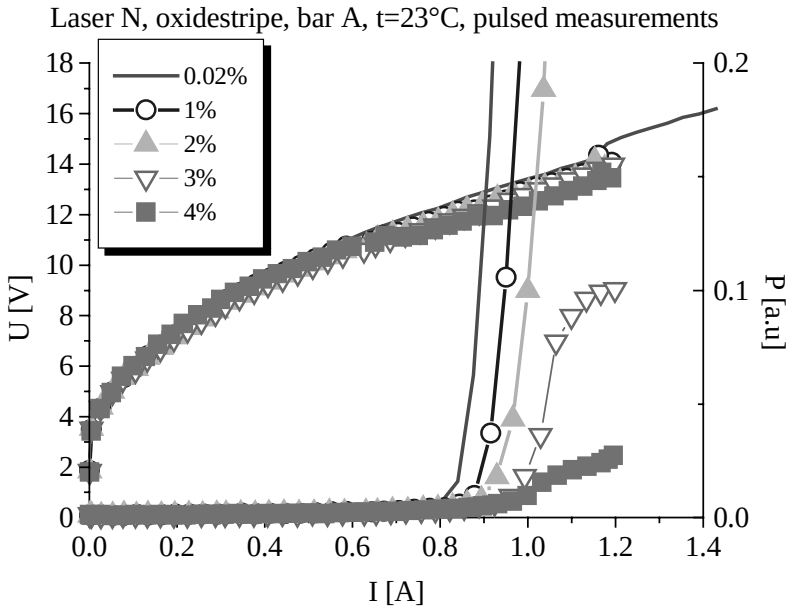

Fig.5.1.22b I-V and P-I characteristics of the oxidestripe laser diode from fig 5.1.22a, measured at various duty-cycle ratios. The heat sink temperature was kept constant at 23°C.

used for these measurements was an un-calibrated one, the qualitative change is a very clear one). This data indicate that, in the case of increased duty-cycle ratios (3% and 4% in figure 5.1.22b), while the active zone temperature is at the beginning of the current pulse much smaller than that corresponding to a heat-sink temperature of 65°C in figure 5.1.22a (as indicated by the threshold current), it increases dramatically during the current pulse. More than this, for duty-cycle ratios larger than 4% it was not possible to get lasing at the same heat-sink temperature. This means that the heat accumulated during the current pulse can't be dissipated enough, even during the pulse break, in order to allow lasing activity. Therefore this means that the thermal resistance of this diode is not good enough.

Because this kind of behavior was typically observed for the laser diodes fabricated during this work, it was suggesting to investigate the thermal resistance of these diodes with the goal to find some possible improvements in thermal design.

To find the value of the thermal resistance in a laser diode an appropriate means must be employed for estimating the temperature rise of the active layer. For example, if the cw lasing is achievable, the temperature in the active zone could be estimated by comparing the threshold current for cw operation with the threshold temperature characteristic measured for low duty-cycle. Also spectral measurements could be employed, by using the wavelength temperature characteristic, or, generally any temperature dependent properties of the laser diode that can be calibrated.

In this work, because the cw lasing was not possible to achieve, it was used the I-V characteristic change with the temperature. By measuring the I-V characteristics in the pulsed pumping mode, using a low duty-cycle (200 ns/1 ms), at various heat-sink temperatures, and respectively in cw mode at room temperature, could be estimated the real temperature inside the laser diode when operating cw. This could be done, of course, with the assumption that the real temperature in the laser during the pulsed operation is the same as the heat sink one – for this reason it was used a very low duty-cycle ratio (0.02%). An example of such measurement can be seen in figure 5.1.23a. The intersection

points of the cw I-V characteristic with the pulsed ones indicate the real temperature in the diode during cw operation.

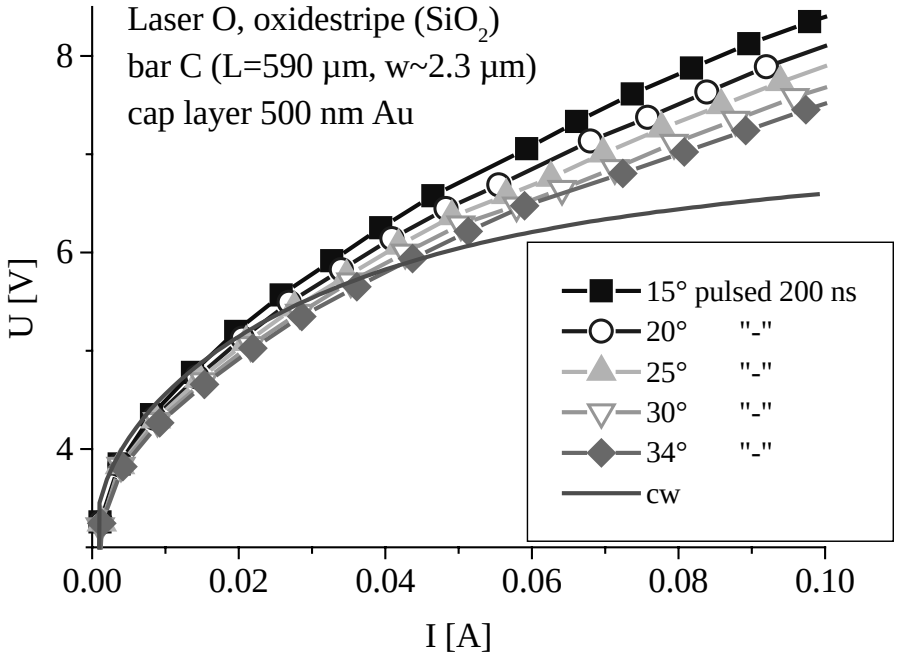

Fig. 5.1.23a I-V characteristics in the low duty-cycle pulsed operation mode at various heat-sink temperatures and respectively in the cw mode at room temperature. The intersection points of the cw I-V characteristic with the pulsed ones indicate the real temperature in the diode during cw operation.

By plotting the real temperature in the cw pumped diode versus the electrical power – considering that, at this low currents, practically all the supplied power is thermally dissipated – from the slope of the curve one obtains the thermal resistance of the laser diode, as is shown in figure 5.1.23b. Because the thermal resistance value depends on the diode geometry, a common formula used [Makino97, Drenten94] is:

$$R_{th} = (1/\pi kL) * \ln(16t/\pi w) \qquad (5.1.17)$$

where k is the thermal conductivity and t the thickness of the laser diode, and w and L are the stripe width, respectively length.

Therefore we measured R_{th} values for diodes with different lengths. The stripe length influence was eliminated considering $R_{th}=R_{th0}/L$ and the value of R_{th0} which is independent of the stripe length was calculated at it is shown in figure 5.1.23c.

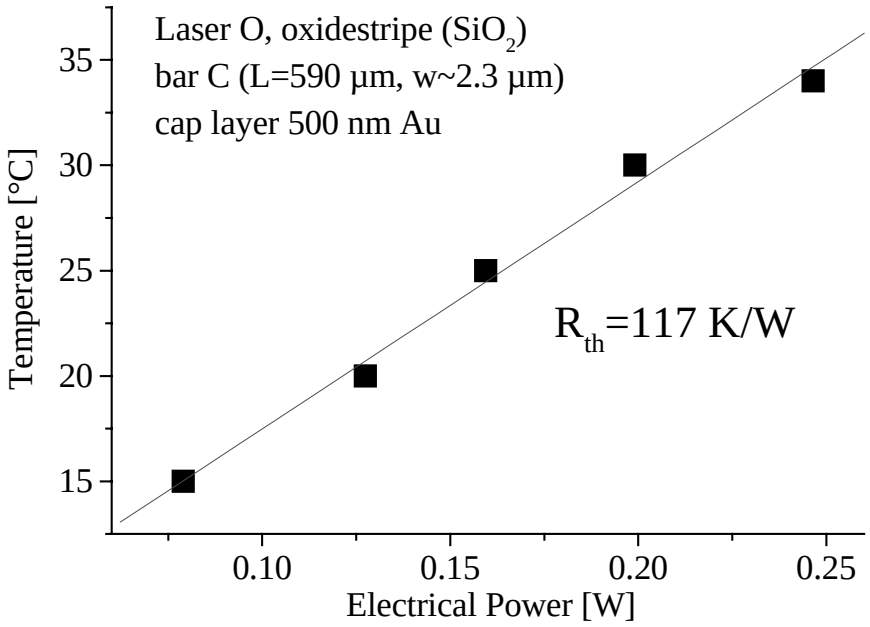

Fig.5.1.23b Real temperature in the laser diode during heat sink room temperature cw operation – data extracted from fig. 5.1.23a – versus electrical power in the low pumping currents range. The slope of this dependence gives the thermal resistance of the diode.

The obtained values of the thermal resistance are pretty high and indicate that, indeed, beside the high threshold current, this is a critical parameter in hindering the cw operation of these laser diodes. Therefore, it was tried to look for possible improvements from this point of view. One possibility is to use a thicker p-contact layer which will act as heat spreader. But increasing the p-contact thickness leads to difficulties in the cleavage process – for realizing the cavity mirrors – due to increased probability of

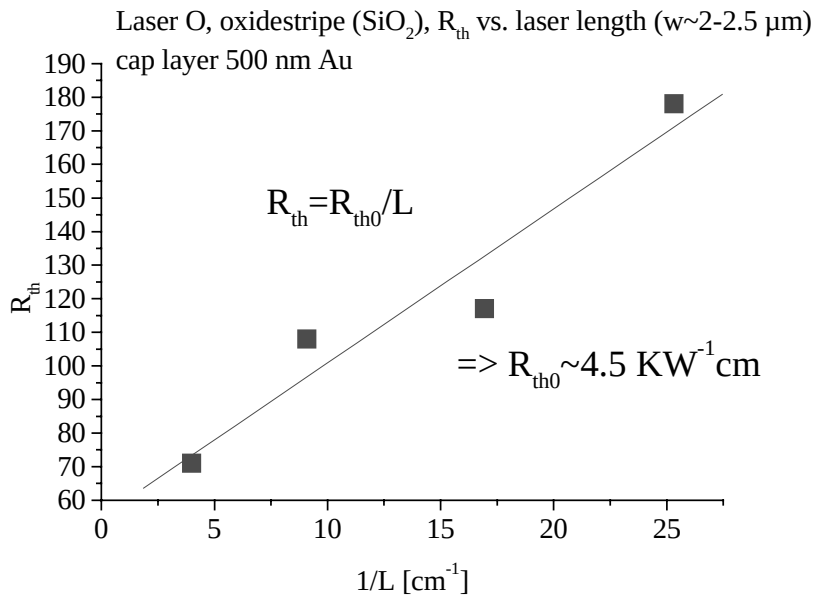

Fig. 5.1.23c Thermal resistance measured as shown in figures 5.1.23a,b, for different stripe lengths. From the dependence $R_{th}=f(1/L)$ one obtains the $R_{th0} = R_{th}*L$ value.

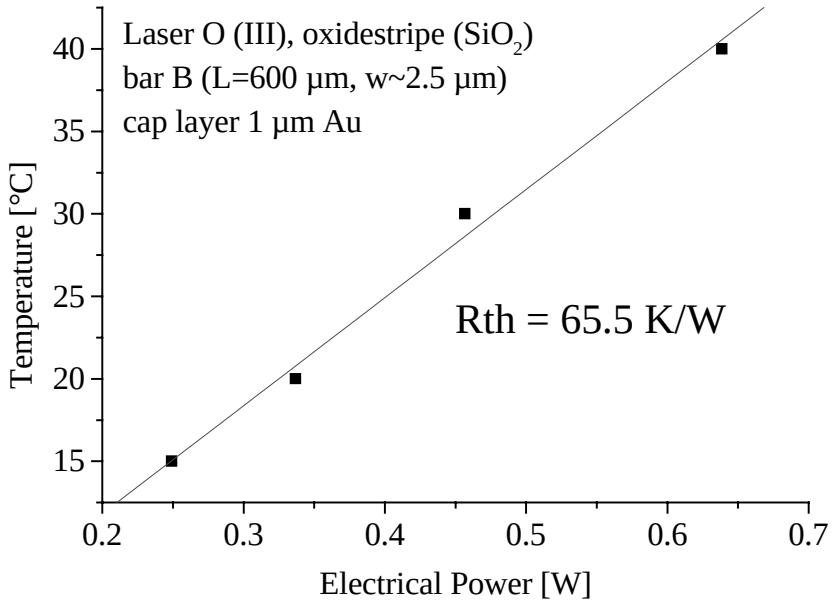

Fig. 5.1.24 Thermal resistance estimation for an oxidestripe diode similar to those from fig. 5.1.23, except the thicker cap Au layer.

getting metal "fingers" from the contacts which can shorten the p-n diode junction. Therefore, it was tested to see the practical effect of increasing the strengthening Au contact layer thickness from 500 nm to 1 μm – for which the gold "fingers" could still be avoided – on the thermal resistance of the laser diode. For this, oxidestripe diodes from the same epitaxial wafer but with thicker strengthening Au contact (1 μm) were processed and their thermal resistance was measured in the above described manner. The result obtained can be seen in figure 5.1.24. It indicates that, by increasing the cap gold layer thickness from 500 nm to 1 μm the thermal resistance of diodes with roughly the same geometry decreases from 117K/W (fig. 5.1.23b) to 65.5 K/W, by around 45%. Therefore this could be considered a very promising approach for further optimizations, if the cleavage related metal "fingers" problem could be also solved.

Another possible direction for decreasing the thermal resistance of the laser diodes is related to the heat flow inside its structure. As mentioned in the fabrication section, in the vertical structure of the laser diode, just beneath the p-contact top-most thick strengthening gold metalization, the dielectric layer that assures the localization of the current just under the p-contact is situated. Usually, the common used dielectric is SiO_2, which was also employed for the laser diodes processed in this work. However, SiO_2 , due to its very low thermal conductivity (0.017 Wcm/K), limits also the heat flow toward the thick, strengthening gold, metalization, acting as heat spreader. Therefore an idea for improving the heat dissipation could be to use a dielectric layer material which also has larger thermal conductivity, allowing in this way a better heat dissipation. As suitable candidates from this point of view could be considered Al_2O_3, having a thermal conductivity value of 0.351 W/cm/K or, even better, AlN with 2.85 W/cm/K. Practically, during this work, it was possible to realize only a preliminary test for replacing the SiO_2 with Al_2O_3. Even if it was successfully with respect to obtaining a working laser diode, as can be seen from figure 5.1.25a, some technological improvements regarding the sputtering parameters adjusting and lift-off technique there are still necessary. Anyway, with regard to the Al_2O_3 contribution to the device thermal

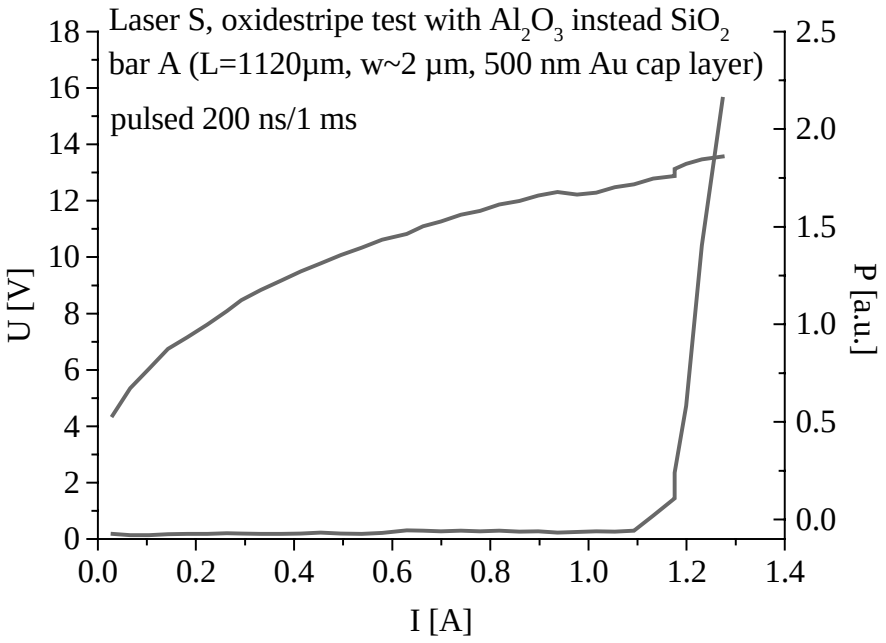

Fig. 5.1.25a I-V and P-I characteristics of an oxidestripe laser diode employing Al_2O_3 (100 nm) as isolator layer.

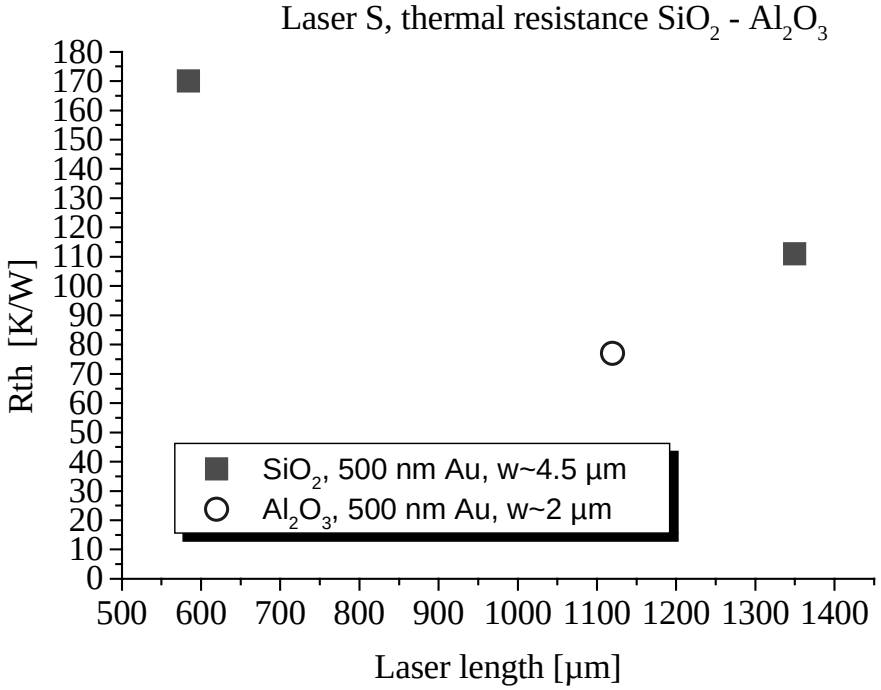

Fig. 5.1.25b Thermal resistance for lasers using SiO_2, respectively Al_2O_3 as isolator layer

resistance, the measured value for this diode compares favorable with that obtained for the diodes using SiO_2, processed from the same wafer and using the same, standard, 500 nm strengthening gold layer as can be seen from figure 5.1.25b. Due to the different geometries of the lasers, a quantitative, direct comparison is difficult to be done. However, qualitatively, the strong decrease of the thermal resistance in the case of Al_2O_3 as isolator layer is clearly demonstrated.

In conclusion, investigating the thermal resistance of the obtained laser diode one finds high values for this parameter which can be a serious obstacle regarding cw operation of GaN-laser diodes. Looking for possible improvements from this point of view, we investigated the influence of increasing the p-contact metalization thickness as well as the exchange of the SiO_2 isolator layer with one having higher thermal conductivity (Al_2O_3), both approaches showing promising results.

5.2 DFB laser diode.

As already mentioned, an attractive solution to overcome the problems related to the optical feedback realization in GaN based laser diodes is to use the DFB – distributed feedback lasers - or DBR – distributed Bragg reflectors – approaches. Further advantages of these kinds of lasers are brought by their stability of the laser emission and, in principle, small line-width, which could enable the application of blue lasers beyond their present use in displays or in optical memories. In this chapter will be presented the realization and characterization of a laterally coupled DFB GaN based laser diode. In the case of the DFB laser the grating providing the optical feedback is incorporated into the heterostructure waveguide throughout the entire laser cavity. In the standard approach, as shown in figure 5.2.1, the grating is etched in the GaN waveguide layer of the ridge.

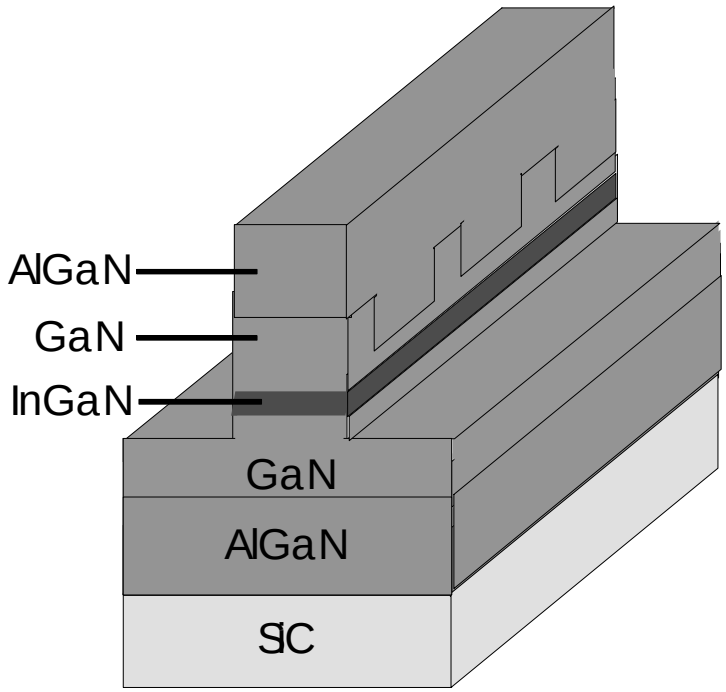

Fig. 5.2.1 A “typical” GaN DFB structure. The AlGaN layer has to be overgrown after realization of the grating in the GaN waveguide layer.

Therefore, in this case, the epitaxial growth has to be interrupted after GaN layer, fabricated the grating, and after that overgrown the AlGaN layer. This makes the entire process rather complicated. Therefore, in this work it was tried another approach, namely a laterally coupled DFB laser, which was a new one for this material system. In such a device, the grating is not inserted in the ridge waveguide, but instead it is etched in the waveguide layer laterally to the ridge, on both sides of it, as shown in the figure 5.2.2. The grating's coupling to the light field in the resonator is assured by that smaller part of the light field that it's spreading laterally outside the ridge region. Of course, the fact that only a small part of the light is interacting with the grating reduces its effectiveness and therefore its coupling coefficient by comparison with the case of a "typical", overgrown DFB laser. The main advantage of the laterally approach is that it's avoiding the need for interrupting the epitaxial growth for the grating fabrication and the subsequent epitaxial overgrowth. Instead, the complete epitaxial grown structure was processed in a similar manner as for the Fabry-Perot laser diodes (see chapter 5.1.1), except that after the ridge-waveguide etching step one realized the grating. For this PMMA e-beam resist was spin-coated over the whole wafer. By high-resolution e-beam lithography the lateral gratings of second order with grating periods between 160 and 169 nm were defined. The grating region placed along the 2 µm wide ridge was 80 µm wide. After developing the resist, the grating pattern was transferred into the semiconductor by an ECR-RIE dry etching step. An example of such grating can be seen in figure 5.2.3. After this step, the process was continued like in the already described Fabry-Perot laser diodes case, with the deposition of the SiO_2 isolator layer, the lift-off process, evaporation of the strengthening p-contact layer and cleavage of the laser bars.
Even if not all the parameters could be optimized in this first approach, the process was successful, as can be seen from figure 5.2.4 where the I-V and P-I characteristics of one of these lasers are shown. As well as from figure 5.2.5 which shows the emission spectra obtained for lasers with different grating periods.

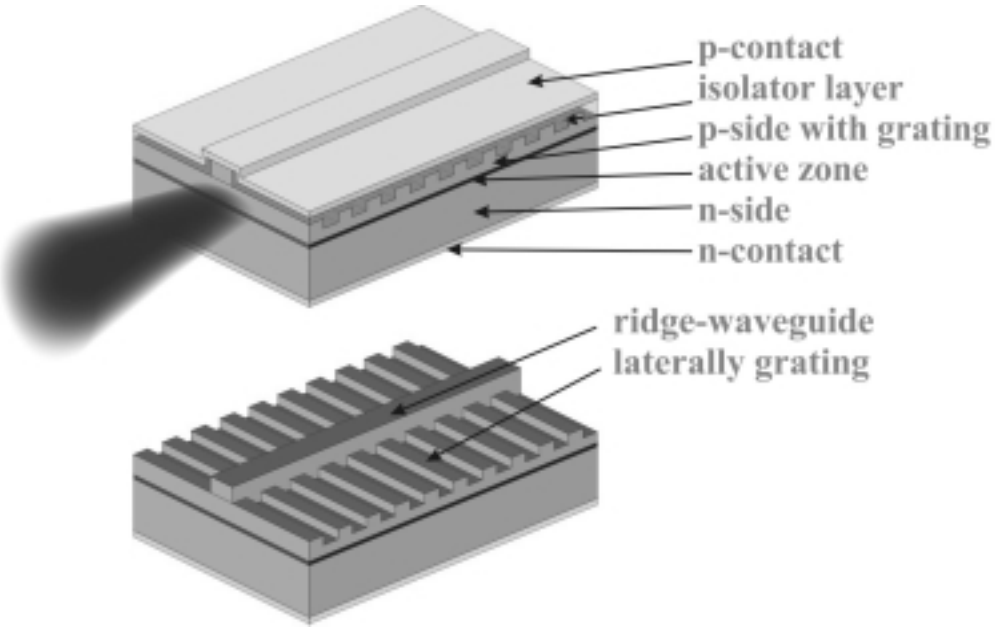

Fig. 5.2.2 Schematic view of the laterally GaN DFB laser diode, showing the ridge-waveguide with the lateral defined gratings (down) and the complete processed laser diode (top).

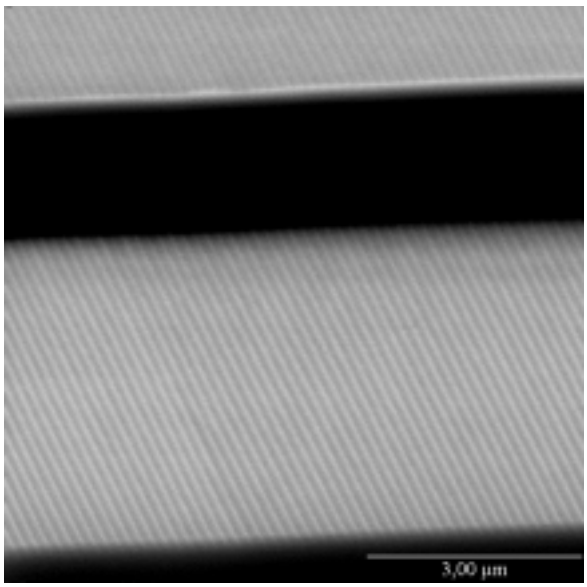

Fig. 5.2.3 SEM picture of a laterally coupled GaN DFB laser. The lateral grating is realized on both sides of the ridge waveguide, perpendicular on it.

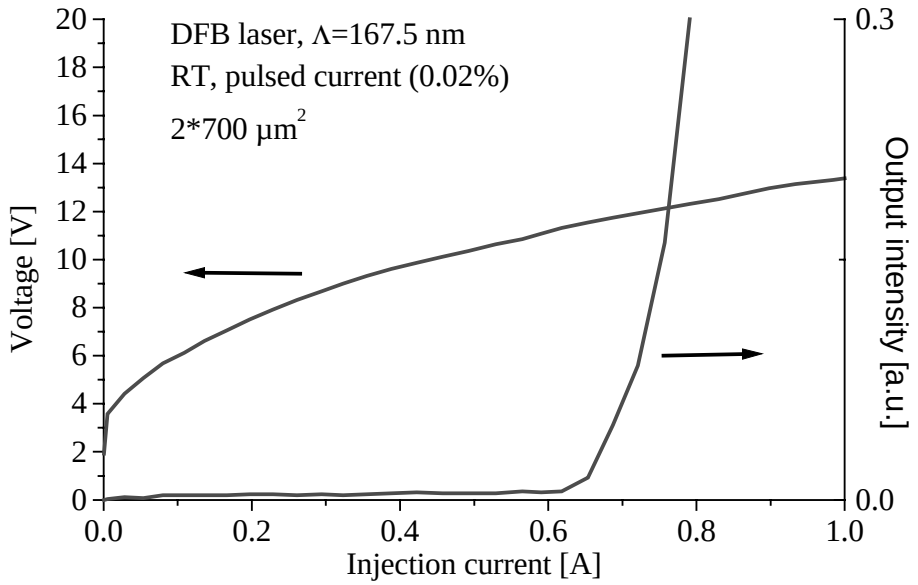

Fig. 5.2.4 I-V and P-I characteristics of a GaN based DFB laser diode.

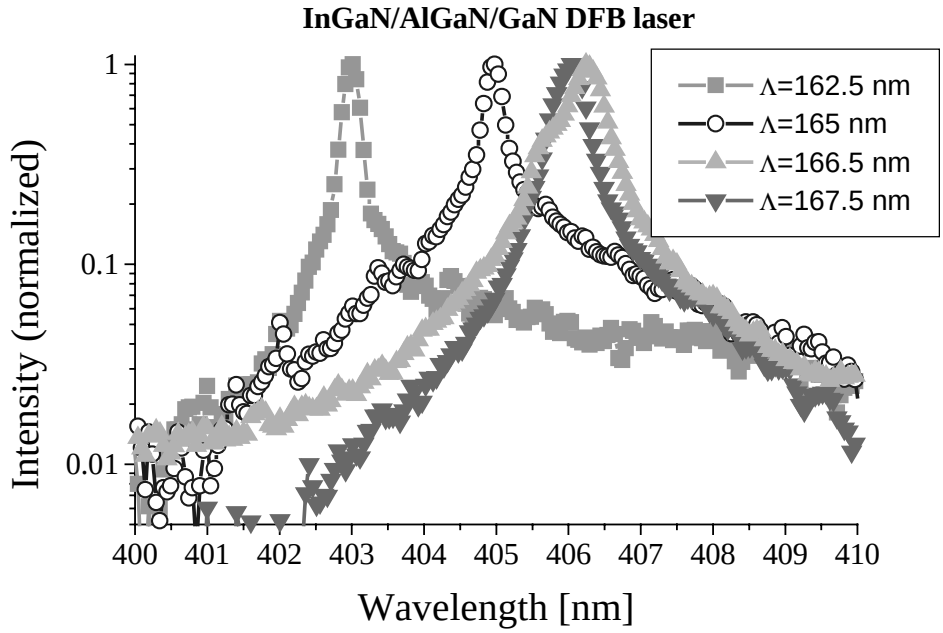

Fig. 5.2.5 Emission spectra (logarithmic plot)of the GaN based DFB laser diodes (pulsed operation) with different grating periods.

According to the coupling of the light to the grating, the Bragg frequency of the DFB emission shifts to longer wavelengths for larger grating periods Λ. For low bias currents the DFB emission spectra are single mode and more modes show up for higher current levels on the long-wavelength side of the main peak. As discussed in [Schweizer02], this could be understood by an in-phase complex coupling regime of the light wave to the grating, which results in a mode threshold spectrum for the DFB lasers showing a distortion of the threshold curve of the complex coupled DFB-laser spectrum compared to the pure index coupled laser. This results in a lowering of the threshold for modes on the long wavelength side of the Bragg emission, therefore, by an increase of the bias current always modes on the long wavelength side show up for higher current levels.
Also, as can be seen form figure 5.2.5, the mode shift of the DFB lasers with grating period is not totally monotonic, but shows some non-monotonic behaviour. This non-monotonic shift it's also visible in figure 5.2.6, where the refractive index, which is given for a second order grating by

$$\lambda_{Bragg} = n_{eff} * \Lambda \qquad (5.2.1)$$

it's plotted as function of wavelength. As can be seen, it shows some scatter around 406 nm. An interesting feature is the observed slope of the dispersion relation of $-1.5*10^{-2}$ nm^{-1} which is a factor of 6 steeper than that of the dispersion relation reported for the optically pumped GaN DFB lasers [Hoffmann00]. This larger slope of the refractive index dispersion in conjunction with the non-monotonic behaviour of the laser modes could be attributed to incompletely screened polarisation fields in the active region of electrically pumped lasers, already mentioned in chapter 5.1.4. In the optically pumped structures overall carrier densities are higher and therefore the internal fields are screened more efficiently. This effect of incompletely screened internal fields in the electrically pumped structures can be seen more clearly if one studies the DFB laser threshold as function of wavelength at different temperatures. In figure 5.2.7 the thresholds of different DFB modes at two temperatures are

shown. As can be seen, for each temperature, the modes achieve a minimum threshold for a certain wavelength - 406 nm for +10 ^{o}C and 407.5 nm for +70 ^{o}C according to the parabolic approach.

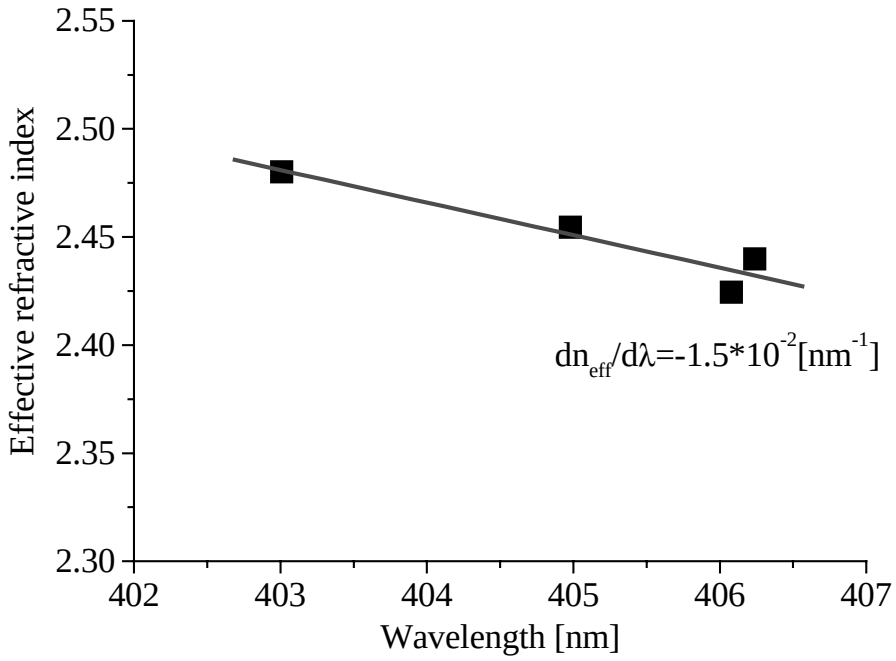

Fig. 5.2.6 Effective refractive index as a function of wavelength derived from DFB laser spectra.

Below and above the minimum the threshold increases as expected for normal band to band transitions. This threshold minimum is given by the maximum of the gain spectra. Therefore the energetic shift of the threshold minima from +10°C to +70°C corresponds to the temperature related band-gap shift of the gain curve, eventually modified by the internal polarisation fields. The obtained value of this shift, of 2.1 10^{-2} nm/K, is lower than that of 6.5*10^{-2} nm/K found for the optically pumped Fabry-Perot lasers [Hoffmann00], and concords well with those found in chapter 5.1.4, confirming the findings that the electrically pumped GaN lasers are more stabile with temperature by comparison with their optical counterparts.
As already explained (see chapter 5.1.4) this is most probably due to the incomplete screening of the internal fields in the

electrically pumped devices which leads to existence of two counterbalancing effects in the band-gap shift with the temperature: a red shift induced by the temperature and a blue shift by the increased screening of the internal fields by injected carriers at higher temperatures.

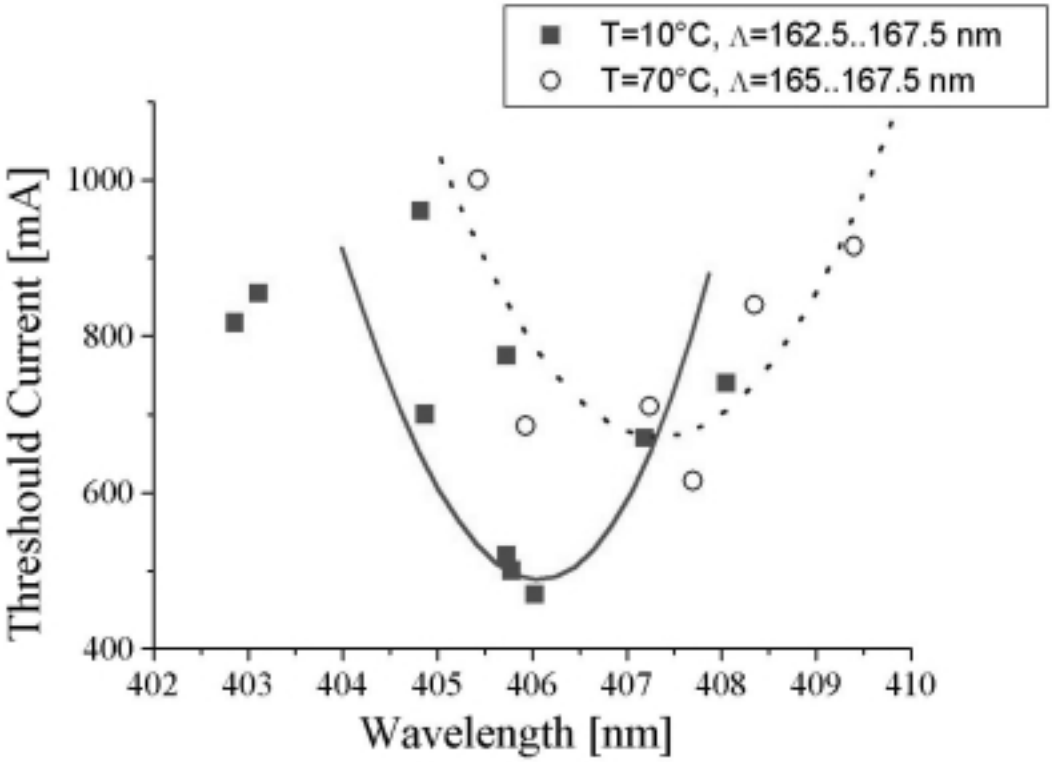

Fig. 5.2.7 DFB laser threshold as function of wavelength for two temperatures.

This enhanced temperature stability of the electrical pumped devices should then, on one hand, be seen also comparing the optically and electrically pumped DFB lasers with respect to their temperature characteristic of lasing wavelength. On the other hand this should lead to the obtaining of a device that is extremely stable with temperature in case of the electrically pumped DFB lasers. This is because, if in a Fabry-Perot laser the wavelength change with the temperature is given by the change of the peak wavelength of the gain profile, in a DFB laser, however, the wavelength change is given by:

$$\Delta\lambda = \frac{d(n_{eff}\Lambda)}{dT}\Delta T = \Lambda\left(\frac{dn_{eff}}{dT}\right)\Delta T + n_{eff}\left(\frac{d\Lambda}{dT}\right)\Delta T \qquad (5.2.2)$$

The first term accounts for the change of refractive index with the temperature and the second term for the grating thermal dilatation which normally can be neglected. Therefore in a DFB laser the wavelength change with temperature is practically induced by the refractive index solely. Thus it is generally much weaker than in a Fabry-Perot laser. This was verified for the optically pumped devices [Hoffmann00], the wavelength change with temperature being $1.7*10^{-2}$ nm/K for the DFB lasers by comparison with $6.5*10^{-2}$ nm/K found for the Fabry-Perot. In the case of these electrically pumped DFB lasers, measuring the emission spectra at different temperature, the found value for the wavelength shift with temperature was $2.9*10^{-3}$ nm/K, as can be seen from figure 5.2.8.

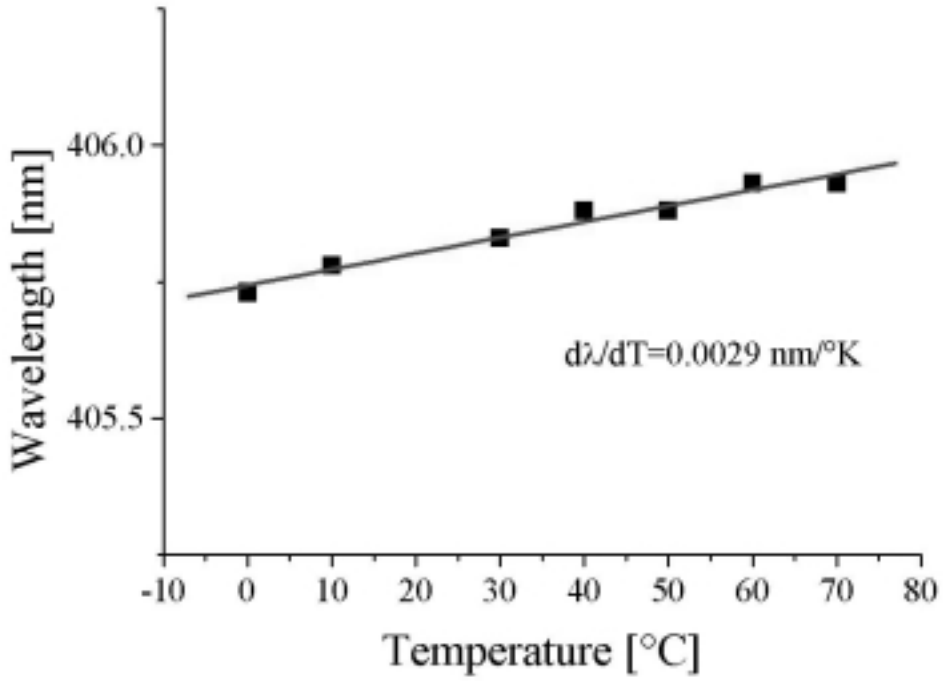

Fig. 5.2.8 DFB emission wavelength as function of temperature

This value is indeed smaller than the above found one of $2.1\ 10^{-2}$ nm/K for the change in peak wavelength of the gain profile – which gives the wavelength shift with temperature for the Fabry-

Perot electrically pumped lasers – and it's smaller also than the $1.7*10^{-2}$ nm/K value reported for the optically pumped DFB lasers. This confirms the enhanced temperature stability of the electrically pumped GaN laser devices – both Fabry-Perot and DFB respectively - by comparison with their optically pumped counterparts. Therefore from this experimental results it is further confirmed also the existence of the incompletely screened internal fields in the electrically pumped lasers, which, as above predicted, indeed leads to an extremely small wavelength shift with temperature in case of the electrically DFB laser.

5.3 DBR laser diode.

Another alternative approach for a laser in addition to the normal Fabry-Perot lasers tested in this work was the realization of distributed Bragg reflector (DBR) laser diode. As described in chapter 2, in case of this device, the mirrors present in the Fabry-Perot laser are replaced by distributed Bragg reflectors placed at the end of the laser cavity. In this way the mirror reflectivity becomes wavelength dependent, the lasing mode being thus determined by distributed reflector parameters. This allows, in principle, the single mode operation of the laser diode. More than this, as already mentioned, using a second order grating, it is possible to couple light from the laser out into the direction perpendicular to the junction, thus obtaining a surface-emitting laser.
In order to test this approach for nitride based laser diodes, a DBR laser structure that is schematically shown in figure 5.3.1 was realized in this work.

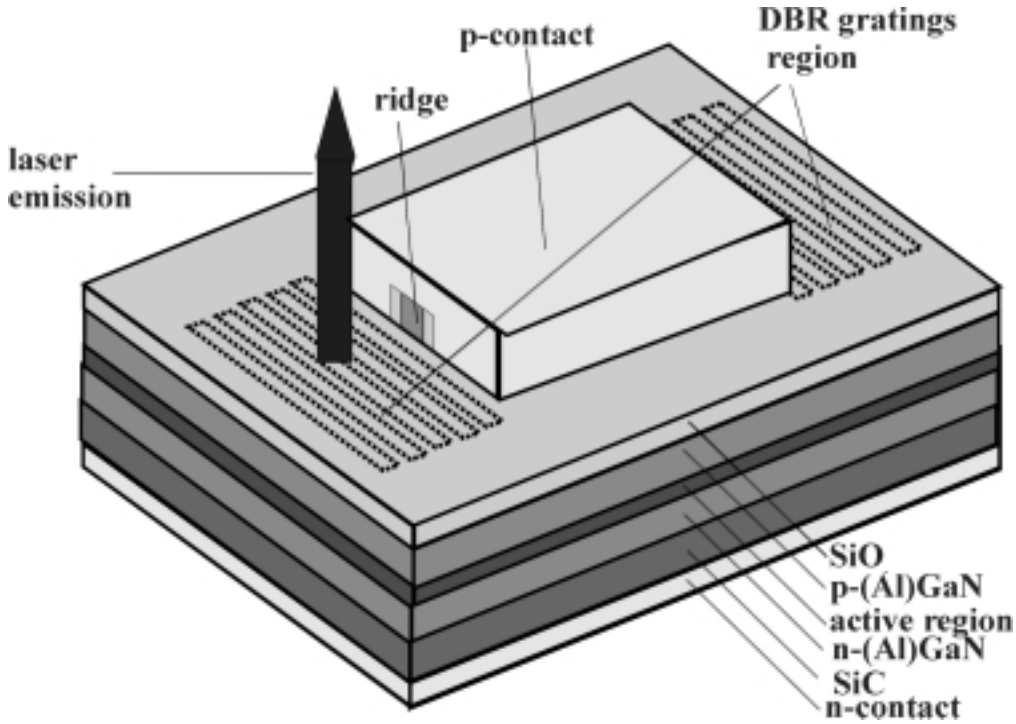

Fig. 5.3.1 Schematic view of the nitride based DBR laser diode with second order grating

For this, on the epitaxially grown wafer, electrical contacts using Ni as n-contact on SiC and Pd/Au as p-contact on p-GaN were firstly realized. After that, for obtaining the ridge waveguide, we applied optical lithography to pattern the p-side into 2 μm wide and 500 μm long stripes which serve for the subsequent dry etching step as etch masks. After the ridge processing step, PMMA e-beam resist for the subsequent grating definition step was spincoated. By high-resolution e-beam lithography second order DBR gratings at both ends of the ridge were defined. The DBR pattern was transferred by an additional dry etching step into the semiconductor. The grating regions were 500 μm long and the grating depth was approximately 50 nm.

As can be seen, the laser fabrication procedure was the same as in the case of the laterally coupled DFB lasers, except that the ridge waveguide defined by optical lithography had a fixed length and the gratings realized after that were positioned at both ends of the ridge. Also, in this case, the cleavage step was avoided altogether – in fact the wafer it wasn't even preliminary thinned. The obtained device therefore had no cleaved mirrors. Instead, because the top of the gratings was free of the metal contact, it was possible to observe the light emission in the vertical direction, which was measured directly on the wafer. In this way, one gets a surface emitting laser with the optical feedback provided solely by the distributed Bragg reflectors without cleaved mirrors necessary.

Even for this first approach where the device parameters couldn't be optimized, the process was a successful and laser emission at room temperature was obtained. The I-V and P-I characteristics measured on such a laser diode, with a grating period of 172.5 nm, can be seen in figure 5.3.2. The threshold current corresponds to a threshold current density of 66 kA/cm^2 and the threshold voltage was 11.2 V. The emission spectra of this laser diode collected with an optical fibre placed on the top of the DBR grating, perpendicular on it, is shown in figure 5.3.3. Using the dependence of emission wavelength λ on the grating period Λ, the effective refractive index of the DBR laser was calculated.

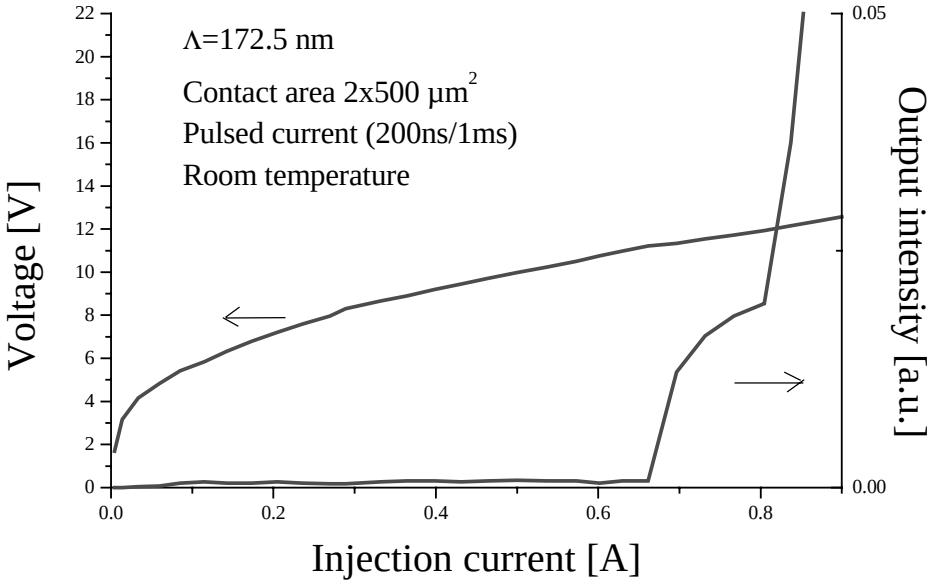

Fig. 5.3.2 Room temperature current-voltage and light output-current characteristics of the GaN based DBR laser diode.

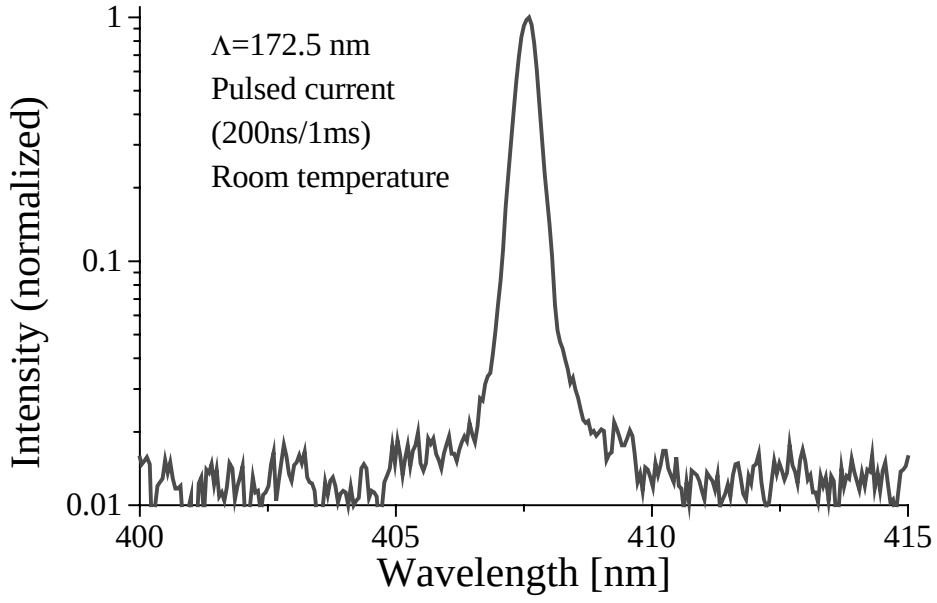

Fig.5.3.3 Emission spectra (logarithmic plot) of the GaN based DBR laser diodes (pulsed operation) at room temperature.

From the Bragg condition $\lambda = 2\, n_{eff}\ \Lambda/m$, where n_{eff} is the effective refractive index and m is the order of the diffraction, one obtains, at room temperature, a value of n_{eff}=2.363. This value agrees well with dispersion data obtained in the case of DFB lasers.
It was also investigated the temperature stability of the obtained device. For estimation of the temperature characteristic of lasing wavelength emission spectra measurements at temperatures between 10 and 70°C were done. The measured spectra are shown in figure 5.3.4. As can be seen, the diode showed laser operation in the pulsed mode even at 70°C. Also, should be highlighted that the spectra remain single mode even for higher temperatures. From these measurements the lasing wavelength dependence on temperature was obtained as shown in figure 5.3.5.

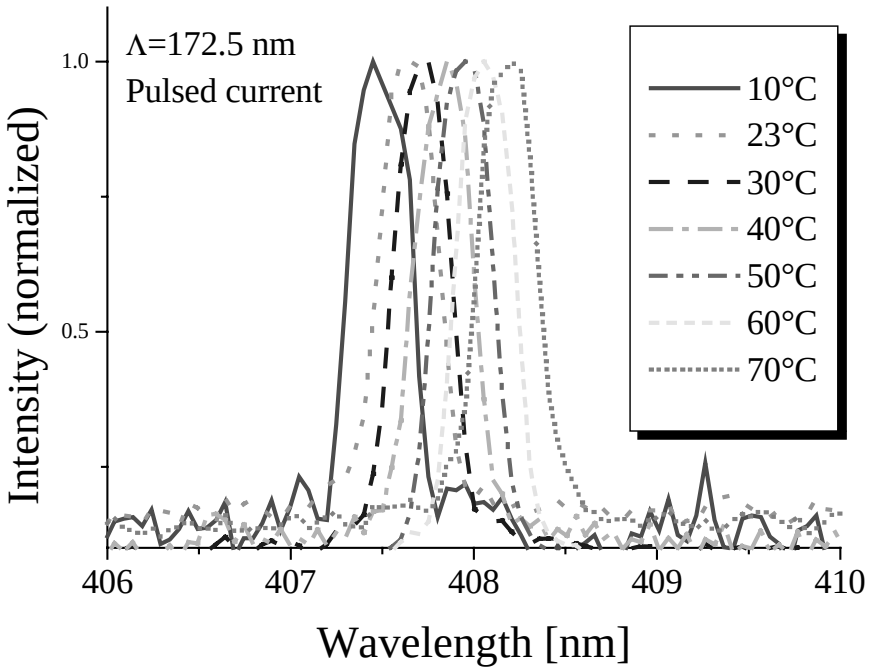

Fig. 5.3.4 Emission spectra of the GaN based DBR laser diode at different temperatures.

The found value of the wavelength shift with temperature was $1.19*10^{-2}$ nm/K. This value is, as expected for a DBR operation, significant lower one than those found for the Fabry-Perot laser

diodes (see chapter 5.1). It is also higher than the extremely low value obtained in case of the DFB device. This might be understood again on the basis of the internal fields in the electrically pumped GaN lasers: In the case of DBR lasers the filter segment is not electrically pumped. Therefore no carrier injection can screen the already present piezoelectric field. Unfortunately, a more precise comparison between the two kinds of Bragg gratings based devices was difficult because the epitaxial wafers used in the two cases were different. However, what is noticeable is that this first approach of realizing a nitride based second order DBR laser diode was successful. By obtaining in this way a nitride surface emitting laser diode whose fabrication procedure avoids altogether the problems related to the mirrors realization this is opening a quite promising way in the field of nitride lasers.

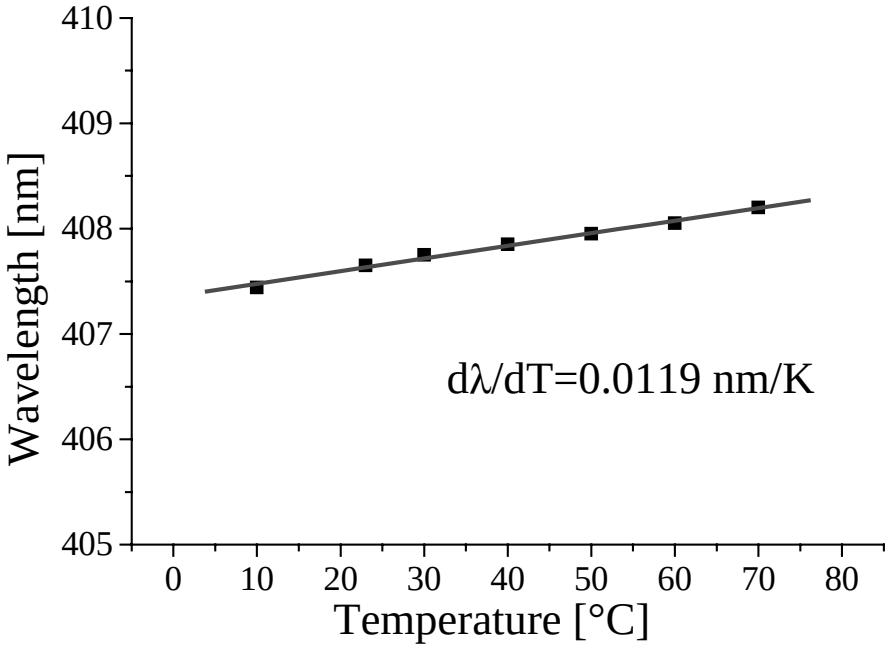

Fig. 5.3.5 DBR laser diode emission wavelength against temperature.

References

[Akasaki97] I.Akasaki, H. Amano, in "High Brightness Light Emitting Diodes" *Semiconductors and Semimetals* Vol 48, Chapter 7, Academic Press 1997

[Alok93] D. Alok, B. J. Baliga, P.K. McLarty, IEDM Technical Digest, 691 (1993)

[Alves03] H. Alves *et. al. phys. stat. sol.* (c) **0**, No 6, 1770 (2003)

[Amano86] H. Amano, N. Sawaki, I. Akasaki, Y. Toyoda, *Appl Phys. Lett* **48**, 353 (1986)

[Amano89] H. Amano, M.Kito, M. Hiramatsu I. Akasaki, *Jpn. J. Appl. Phys.* **28** L2112 (1989)

[Ambacher98] O. Ambacher, *J. Phys.D: Appl. Phys*. **31**, 2653 (1998)

[Ambacher03] O. Ambacher *et. al., phys. stat. sol. (c)* **0**, No.6, 1878 (2003)

[Andrews75] J. M. Andrews and J.C. Phillips, *Phys. Rev. Lett.* **35**, 56 (1975)

[Bader00] S. Bader *et. al., phys. stat. sol. (a)* **180**, 177 (2000)

[Bernardini97] F. Bernardini, V. Fiorentini, D. Vanderbildt, *Phys. Rev. B* **56**, R10024 (1997)

[Björk87] G. Björk and O. Nilsson, *IEEE J. Lightw. Technol.* **5**, 140 (1987)

[Böttcher03] T. Böttcher *et. al. , phys.stat.sol. (c)* **0**, No 6, 1846 (2003)

[Brillson78] L.J. Brillson, *Phys. Rev. Lett***. 40**, 260 (1978)

[Carrol98] J. Carrol, J. Whiteaway, D. Plumb " Distributed feedback semiconductor lasers" Institution of Electrical Engineers, London, 1998

[Cartwright99] A. N. Cartwright *et.al. MRS Internet J. Nitride Semicond. Res. 4*, 12 (1999)

[Chu00] C. Chu *et al . Appl Phys. Lett* **77**, 3423 (2000)

[Cowley65] A. M. Cowley and S.M. Sze *J. Appl. Phys.* **36**, 3212 (1965)

[Crofton95] J.Crofton, P.G. McMullin, J.R. Williams, M.J. Bozack, *J. Appl. Phys*.**77**, 1317 (1995)

[Crofton97] J.Crofton, L.M. Porter, J.R. Williams, *phys.stst.sol*. (b) **202**, 581 (1997)

[Cole00] M.W. Cole et al. *Journal of Applied Physics* Vol 88, No 5 2652 (2000)

[Chang01] S. Chang, Y. Su *Appl Phys. Lett* **78**, 312 (2001)

[Chuang95] S. L. Chuang "Physics of Optoelectronic Devices" New York, Willey 1995

[Dadgar03] A. Dadgar *et. al., phys. stat. sol. (c)* **0**, No.6, 1538 (2003)

[Davydov02] V. Y. Davydov *et.al. phys.stat.sol. (b)* **230**, R4-R6 (2002)

[Drenten94] R.R. Drenten *et al., J. Appl. Phys*.**76**, 3988 (1994)

[Edgar94] J.H. Edgar (Editor); Properties of Group III Nitrides, INSPEC 1994

[Fiorentini99] V. Fiorentini *et.al.* , *Phys. Rev. B* **60,** 8849 (1999)
[Frankowsky96] G. Frankowsky, F. Steuber, V. Härle, F. Scholz, A. Hangleiter, *Appl. Phys. Lett.* **68**, 3746 (1996)

[Gessmann02] T. Gessmann *et al., Appl Phys. Lett* **80**, 986 (2002)

[Hangleiter98] A. Hangleiter *et.al*. *MRS Internet J. Nitride Semicond. Res. 3*, 15 (1999)
[Hangleiter03] A. Hangleiter, *phys. stat. sol (c)* **0**, No6, 1816 (2003)
[Hatakoshi99] G. Hatakoshi *et al*.*Jpn. J. Appl. Phys*. **38**, 2764 (1999)
[Hasegawa86] H. Hasegawa and H. Ohno, *J. Vac. Sci. Technol.* **B4(4**), 1130 (1986)
[Härle00] V. Härle *et.al., phys. stat. sol. (a)* **180**, 5 (2000)
[Härle02] R. Härle, *Diplomarbeit*, Universität. Stuttgart 2002
[Heine65] V. Heine, *Phys. Rev.* **A 138**, 1689 (1965)
[Henisch84] H.K. Henisch "Semiconductor Contacts" Clarendon Press Oxford 1984
[Hofmann00] R. Hofmann, *Dissertation*, Universität. Stuttgart 2000
[Ho99] J. Ho *et al. Appl Phys. Lett* **74**, 1275 (1999)

[Ikeda02] M. Ikeda and S. Uchida,. *phys.stat.sol (a)* **194**, No2, 407 (2002)
[Ivanov03] A. Ivanov *et al*, 10th European Workshop on Metalorganic Phase Epitaxy, Lecce (2003)

[Kaufmann98] U. Kaufmann *et.al. ., Appl Phys. Lett* **72**, 1326 (1998)
[Kneissl00] M. Kneissl *et.al. ., Appl Phys. Lett* **77**, 1931 (2000)
[Kuhn02] B. Kuhn, *Dissertation*, Universität. Stuttgart 2002
[Kim01] D. Kim *et al, J. Vac. Sci. Technol.* B 19(3) 609 (2001)
[Kimura01] Y. Kimura et. al. *Jpn. J. Appl. Phys* **40,** L1103, (2001)
[Kobayashi02] Y. Kobayashi *et al, J. Crystal Growth* **243**, 103 (2002)
[Kogelnik72] H. Kogelnik and C.V. Shank, *Appl Phys. Lett* **43** (5), 2327 (1972)
[Kumakura00] K.Kukamura, T Makimoto, N. Kobayashi, *Jpn. J. Appl. Phys*. **39** L195 (2000)
[Kumakura01] K.Kukamura, T Makimoto, N. Kobayashi, *Appl Phys. Lett* **79,** 2588 (2001)
[Kuramata98] A. Kuramata *et. al. Jpn. J. Appl. Phys.* Vol **37**, L1373 (1998)
[Kurimoto02] E Kurimoto et al. *Journal of Applied Physics* Vol 91 No12, 10215 (2002)

[Lai00] W. Lai *et al*. *Jpn. J. Appl. Phys* 39, L1138 (2000)

[Lee99] J. Lee *et al Appl Phys. Lett* **74**, 2289 (1999)
[Lewis02] G.M. Lewis, P.M: Smowton, J.D: Thomson, H.D. Summers, P. Blood, *Appl Phys. Lett* **80** 1, (2002)
[Li00] Y. L. Li *et al Appl Phys. Lett* **76**, 2728 (2000)
[Liu00] B.Liu, M.H. Ahonen, P.H. Holloway, *MRS Internet J. Nitride Semicond. Res. 5S1*, W11.78 (2000)

[Makino97] T. Makino, J.D. Evans and G. Mark, *Appl Phys. Lett* **71**, 2871 (1997)
[Marinova96] Ts. Marinova et al *J. Vac SciTechnol*. B 14(5) 3252 (1996)
[Miyachi98] M. Miyachi, T. Tanaka, Y. Kimura H. Ota *Appl Phys. Lett* **72,** 1101 (1998)
[Miskys03] C. R. Miskys, M. K. Kelly, O. Ambacher, M. Stutzmann, ., *phys. stat. sol. (c)* **0**, No.6, 1627 (2003)

[Nakamura91] S. Nakamura, *Jpn. J. Appl. Phys* **30,** L1705 (1991)
[Nakamura92] S. Nakamura, N. Iwasa, M. Senoh T. Mukai *Jpn. J. Appl. Phys* **31,** 1258 (1992)
[Nakamura96] S. Nakamura et al., *Jpn. J. Appl. Phys* **35,** L74 (1996)
[Neugebauer95] J. Neugebauer and C.G. Van de Walle *Physical Review Letters.* **75**, 4452 (1995)
[Neugebauer96] J. Neugebauer and C.G. Van de Walle *Appl Phys. Lett*. 68, 1829 (1996)

[Off01] J. Off, , *Dissertation*, Universität. Stuttgart 2001

[Park98] Yoon Soo Park "SiC Materials and Devices" Semiconductors and Semimetals Vol52, Academic Press (1998)
[Pearton96] S.J. Pearton *et al., Appl Phys. Lett*. **69,** 1879 (1996)
[Pearton99] S.J. Pearton *et al., J. Appl. Phys*. Vol 86, (1999)
[Petit94] J.B. Petit P.G. Neudeck, C.S. Salupo, D.J. Larkin J.A. Powell. *Inst Phys. Conf. Ser*. No 137, 679 (1994)

[Robinson85] G. Y. Robinson in "Physics and Chemistry of III-V Compound Semiconductors Interfaces" Edited by C. W. Wilmsen, Plenum Press 1985

[Sharma81] B. L. Sharma in "Semiconductors and Semimetals" Vol. 15, edited by R. K. Williardson and A. C. Beer, Academic Press 1981
[Shaklee73] K.L. Shaklee, R.E Nahori, R.F. Leheny, *J. Lumin*.**7**, 284 (1973)
[Scherer01] M. Scherer *et al., J. Appl. Phys.* Vol 89, (2001)
[Sheu99] J.K. Sheu *et al., Appl Phys. Lett*. **74**, 2340 (1999)
[Scholz03] F. Scholz *et.al*., Journal of Crystal Growth 248, 507 (2003)
[Schreiner02] R. Schreiner, *Dissertation*, Universität. Stuttgart 2002

[Schweizer02] H. Schweizer *et. al., phys. stat. sol. (a)* **192**, 301 (2002)
[Strassburg03] M. Strassburg *et. al. phys.stat. sol. (c)* **0**, No.6, 1835 (2003)
[Suematsu94] Y. Suetmatsu and A. R. Adams "*Handbook of Semiconductor Lasers and Photonic Integrated Circuits"* Chapman & Hall, London 1994
[Sze81] S.M Sze "Physics of Semiconductor Devices" John Wiley & Sons 1981

[Takeda02] M. Takeda *et.al. phys.stat.sol (a)* **192**, No2, 269 (2002)
[Teraji 97] T.Teraji, S. Hara, H. Okushi, K. Kajimura, *Appl. Phys. Lett*. 71 (5) 689 (1997)
[Tersoff84] J. Tersoff, *Phys. Rev. Lett. 52*, 465 (1984)
[Thompson80] G.H.B. Thompson "Physics of Semiconductor Laser Devices" Wiley 1980

[Vechten92] L. A Van Vechten, J.D. Zook, R.D. Horning, B. Goldenberg, *Jpn. J. Appl. Phys* **31,** 3662 (1992)

[Wetzel98] C. Wetzel *et.al*. *MRS Internet J. Nitride Semicond. Res. 3*, 31 (1998)
[Williams85] R.H. Williams in "Physics and Chemistry of III-V Compound Semiconductors Interfaces" Edited by C. W. Wilmsen, Plenum Press 1985

CURRICULUM VITAE

Dumitru Viorel-Georgel

Date and place of birth: 14.04.1972, Ploiesti, Romania

Education:

-1979-1987 Primary school: Scoala cu cl.I-VIII No. 25, Ploiesti, Romania

-1987-1991 High school: Liceul “Mihai Viteazul”, Ploiesti, Romania

-1996: Diploma Degree, Faculty of Physics, Bucharest University
Subject: “Obtaining and Characterization of Aluminium Nitride Thin Layers”

-1997: Master of Science in Semiconductor Physics, Faculty of Physics, Bucharest University
Dissertation subject: “ The study of the growth mode and the optimisation of deposition conditions of aluminum nitride thin films obtained by reactive magnetron sputtering”

Scientific Activity:

1996-2000, research assistant at the Institute for Physics and Technology of Materials, Bucharest, Romania

2000-2004, PhD student at the 4 Physikalisches Institut, Universität Stuttgart, Germany

Thanks:

I express my gratitude to the following persons:

• Prof. Dr. M.H. Pilkuhn for accepting me as PhD student within 4. Physikalisches Institut;

• Prof. Dr. H. Schweizer for guiding this work. His support, encouragement and so many stimulating discussions have been very important for me;

• Prof. Dr. M. Berroth for co-refering this thesis;

• Prof. Dr. F. Scholz, Dr. M. Jetter for very usefull discussions and their unceasing encouragement;

• All my colleagues from 4. Physikalisches Institut for their kindly helps and nice working atmosphere. In particular I owe a special “Thanks!” to: T. Ballmann, O. Breitschädel, A. Gröning, L. Fu, R. Härle, A. Ivanov, M. Körbl, B. Kuhn, A. Malik, J. Off, H. Roll, S. Rurländer, R. Schreiner, V. Perez-Solorzano, J. Schwarz, W. Wagner, M. Zimmermann;

• H. Gräbeldinger, E. Frank, E. Lux, J. Mehne, G. Moutchnik and M. Ubl for their great support and help in the lab work;

• The nitrides research group from the firm OSRAM Opto Semiconductors;